Università degli Studi di Roma "Tor Vergata"
Facoltà di Scienze Matematiche, Fisiche e Naturali.
Dottorato di ricerca in Astronomia – XVII ciclo

The RR Lyrae distance scale from Near-Infrared photometry

Massimo Dall'Ora

Coordinatore
Prof. Roberto Buonanno

Relatore
Prof. Roberto Buonanno

Tutore
Prof. Giuseppe Bono

Contents

Abstract

The work carried out in this thesis is part of a long-term project aimed at measuring accurate near-infrared magnitudes of RR Lyrae stars in a sample of Galactic globular clusters that cover a wide metallicity range ($-2.3 \leq [Fe/H] \leq -1.3$) and host a sizable population of RR Lyrae stars ($N_{RR} \geq 10$).

In this thesis we will present the result obtained for the Galactic globular clusters M68 and NGC3201, and for the Large Magellanic Cloud cluster Reticulum. The results for these clusters are all based on the observations carried out with SOFI/NTT.

The data collected allowed us to provide accurate estimates of *J, K* mean magnitudes for a large portion of the cluster RR Lyrae variables, and in turn to derive in a homogeneous context the slope of the *K*-band Period-Luminosity relation (*PLK*). The slope of the observed *PLK* relation agrees quite well with theoretical pulsational predictions. On the basis of this agreement between our empirical *PLK* relations and the theoretical ones, we adopted the latter for estimating the absolute distances to the target clusters. The distances obtained for M68, NGC 3201, and Reticulum disclose a fairly good agreement with the most recent and accurate independent estimates (Baade-Wesselink calibration, FOBE method, δ Scuti Period-Luminosity relation).

Current data, together with near-infrared data already collected, will allow us to accomplish the following goals:

- to derive, on the basis of the new empirical calibration of the *PLK* , absolute distances for field RR Lyrae stars for which are available mean *K* magnitudes and to compare them with distances based on Baade-Wesselink method;
- to provide, on the basis of predicted and observed *PL(J-K)*relations, independent estimates of the reddening toward the target clusters;
- to supply an independent test on a wide metallicity range of the accuracy of both evolutionary and pulsational predictions adopted to construct the *PLK* and the *PL(J-K)* relations;
- to obtain accurate optical/near-infrared Color-Magnitude diagrams (CMDs) for the target clusters by adopting the new data and the optical data available in the literature.

These CMDs will allow us to compare theory and observations by using color indexes (V-J), (V-K), which are only marginally affected by systematic uncertainties;

- to use (V-K) colors to derive accurate estimates of the effective temperatures of the globular clusters RR Lyrae stars, which in turn can be used to provide an estimate of the helium abundance. This result is particularly interesting, because globular clusters are among the oldest objects that can be found in the Galaxy, and therefore the estimated helium estimates can give a hint on the primordial helium abundance.

Chapter 1
The Scientific Problem

1.1 RR Lyrae stars as distance candles

Since the first trigonometric distance measurement performed by Bessel on the star P Cygni in 1838, one of the major problems in the Galactic and in the extragalactic astronomy is the development of robust methods to provide accurate estimates of the cosmic distances. Together with the development of the spectroscopic observations, Astronomy became Astrophysics with the advent of distance measurements, the third dimension in our vision of the sky. Indeed, the knowledge of the physics of the celestial objects, and of the Universe as a whole, is tied to the knowledge of the absolute distances.

Connected to the distance scale problem is the building of a comprehensive framework of the formation and evolution of the galaxies, and first of all of the Milky Way. Indeed, the calibration of robust standard candles allows us to trace the 3-D structure of our system and of the group of galaxies to which the Galaxy belongs, the Local Group. Moreover, correct estimates of the stellar distances allow us, via a comparison with the theoretical models of stellar evolution, to give an idea of the ages of the stellar populations and, together with chemical abundances, to trace back the history of their formation and evolution.

In this context, RR Lyrae stars are particularly important, since they are standard candles that can be observed in all the old components of the stellar systems: Galactic and extragalactic globular clusters, Galactic halo, Galactic Bulge, ancient populations of the nearby galaxies, such as the Magellanic Clouds and the dwarf spheroidal galaxies of the Local Group. These systems were among the first formed in the Universe, and therefore it is crucial to have accurate estimates

of their distances and ages, in order have strong constraints on the formation and evolution of the structures in the Universe.

Without entering into a detailed discussion on the calibration of the standard candles, here we mention only the fact that the use of the RR Lyrae stars as distance indicators is still hampered by several uncertainties, both on the empirical and on the theoretical side, mainly connected to the dependence of their absolute *V*-band magnitude on the chemical composition and on the uncertainty on the evolutionary status. Current uncertainties on the absolute visual magnitude of the RR Lyrae stars are of the order of 0.2-0.3 mag. Details will be given in chapter 2.

At the same time, RR Lyrae stars in the photometric *K*-band (centered on the effective wavelength $\lambda_{eff} = 2.2\mu m$) do obey to a tight linear period-luminosity relation (*PLK*). This relation offers several advantages, both theoretical and observational, when compared to other techniques. Once calibrated, this relation could be a powerful and sound tool to gain accurate and homogeneous distances for old stellar components.

1.2 The PhD Project

The main goal of this thesis project is to substantially improve the distance estimates to the globular clusters with the *PLK* relation. Results have been produced for two Galactic globular clusters, namely M68 and NGC 3201, and for the Large Magellanic Cloud cluster Reticulum.

Data presented in this thesis work are part of a more general project, which has a threefold objective:

- we still lack an extensive *K*-band observational database for RR Lyrae stars. Indeed, empirical estimates of the *PLK* relation have been published only for nine Galactic globular clusters: M3, M4, M5, M15, M107, NGC 3201, NGC 5466, Ω Cen (Longmore et al. 1990), and IC 4499 (Storm 2004); M3 was observed also by Butler (2003). Unfortunately, the Longmore et al. (1990) measurements are heavily affected by observational uncertainties such as crowding, since their photometry was carried out with a fixed-aperture photometer and the derived *PLK* for the single clusters have uncertainty of the order of 10-15% on the slope. Butler (2003) observed only seven RR Lyrae stars in the innermost regions of the Galactic globular cluster M3. Storm used single-epoch observations to estimate a distance to IC4499, but the measurements are affected, on

average, by an error of the order of 10%. The fist objective of our project is therefore to supply a homogeneous photometric database to derive an accurate estimate of the empirical *PLK*;

- theory predicts a non-negligible dependence of the *PLK* on the chemical composition, which translates in a different zero-point of the relation. Therefore, to proper compare results for RR Lyrae stars of different chemical composition, it is of paramount importance to test theoretical predictions with observations. The test can be performed by comparing the observed *PLK* relations for sizable samples of chemically homogeneous RR Lyrae stars with the *PLK* relations predicted by theory. The ideal targets for such a comparison are the globular clusters, both Galactic and extragalactic, since they are coeval and chemically homogeneous stellar populations, and their stars can be all considered at the same distance;
- once an accurate empirical *PLK* has been obtained and a comparison with the predicted *PLK* has been performed to investigate the dependence of the relation on the chemical composition, we plan to use the *PLK* relation to achieve accurate distance estimates for cluster and field RR Lyrae stars, belonging to several old stellar populations.

Specifically, the environments for which data have been already collected are:

1. Galactic Globular Clusters (GGCs). Data have been collected for 17 globular clusters that cover a wide range in chemical content. Since the method yields *absolute* distances, absolute ages can be inferred, giving a lower limit to the age of the Galaxy and of the Universe. Moreover, the selected clusters span a wide range in metallicities, allowing a meaningful test of the metallicity-dependence of the *PLK*.
2. Galactic Bulge. Although the distance to the Galactic center is a fundamental parameter, used, for example, in the dynamical models of the Milky Way, its determination is still hampered by several uncertainties (Reid 1993). One of the main sources of error in the distance estimates of the Galactic center is the uncertainty on the strong (and differential) absorption, which translates into errors of the order of 10% in the estimates of the de-reddened magnitudes. However, *PLK* relation constitutes a robust diagnostic to achieve distances for RR Lyrae stars in the Bulge, since the absorption in the *K*-band is only the 10% of the absorption in the *V*-band.

3. Galactic Halo. Empirical evidence (Vivas et al. 2001) shows that RR Lyrae stars of the Galactic Halo have a clumpy distribution. Data have been collected for three fields, and they should provide information both on the distance and the structure of the clumps. One of these clumps could be the sign of the accretion by the Galaxy of the Sagittarius dwarf galaxy and the others could be the relic of the globular cluster Pal 5. On the basis of the estimates of the RR Lyrae distances, it should be possible to assess whether the first of the observed fields is the relic of the Sagittarius dwarf (Helmi & White 1999; 2001), and to check if the other two fields are connected to the tidal debris of the globular cluster Pal 5.
4. Large Magellanic Cloud (LMC). LMC is the first ladder in the extragalactic distance scale, and therefore it is of paramount importance to get an accurate distance estimate of its center, as well as of its 3-D structure. Our dataset includes 5 globular clusters, located in different positions along this galaxy, and 3 pointings along the central bar, with about 150 field RR Lyrae stars expected. This dataset should provide an estimate of the distance and of the geometry of the LMC with an unprecedented accuracy.

Table 1.1 summarizes the complete dataset.

Environment	Object	[Fe/H]	Instrument	Status
GGCs	M 92	-2.28	NICS	Observing
			SWIRCAM	Observed
	M 15	-2.26	NICS	Observed
	M 68	-2.06	SOFI	Reduced
	M 53	-1.99	NICS	Observing
	Ω Cen	-1.62	SOFI	Observed
	M 2	-1.62	NICS	Reducing
	NGC 3201	-1.58	SOFI	Reduced
	M 3	-1.57	NICS	Observing
	NGC 6522	-1.44	SOFI	Observed
	M 72	-1.40	SOFI	Observed
			NICS	Observed
	Pal 5	-1.41	SOFI	Observed
	M 14	-1.39	SOFI	Observed
	M 5	-1.27	SOFI	Observed
			NICS	Observing
	NGC 1851	-1.22	SOFI	Observed
	NGC 6388	-0.60	SOFI	Observed
	NGC 6441	-0.53	SOFI	Reducing
	NGC 6528	-0.04	SOFI	Observed
Baade Window	18 Fields	≈ -0.2 (a)	SOFI	Observed
			ANDICAM	Observed
Sagittarius Clump	3 Fields	≈ -1.4 (b)	SOFI	Observed
LMC	NGC 1841	-2.11 (c)	SOFI	Observed
	NGC 1466	-1.85 (d)	SOFI	Observed
	NGC 1835	-1.8 (e)	SOFI	Observed
	Reticulum	-1.71 (c)	SOFI	Published
	NGC 2257	-1.63 (f)	SOFI	Observed
	Bar, 3 Fields	≈ -1.5 (g)	ISPI	Observed

Table 1.1. The complete dataset available for this project. Metallicities for Galactic Globular Clusters are from the catalogue by Harris (1996). (a) Alves (2000); (b) Pal 5 value adopted (Harris 1996); (c)Suntzeff et al. (1992); (d) Walker (1992); (e) Walker (1993); (f) Dirsch et al. (2000); (g) Gratton et al. (2004), mean value.

Chapter 2
RR Lyrae stars

RR Lyrae stars are low-mass, radially pulsating variable stars, typical of old stellar populations. Since their discovery, occurred at the end of the 19th century by S. Bailey (Pickering & Bailey 1895), it was recognized that their mean V magnitude is almost constant. This occurrence, together with the fact that they are moderately bright ($\approx 40 L_{\odot}$), ubiquitous in all the stellar systems hosting an old population, and easily recognizable from their light curve, make them attractive as distance indicators.

2.1 Observational properties

RR Lyrae stars appear as bright giants stars, with spectral types ranging from A to F (Smith 1995), which show regular light variations. Radial velocities curves, together with the Baade-Wesselink analysis, demonstrate that the light variation is connected with a periodic variation in the radius of the structures (fig. 2.1).

The three observable quantities, without considering spectra, are magnitudes, pulsation period, and pulsation amplitudes. Magnitudes and color indexes can be adopted to derive the Color-Magnitude-Diagram (CMD, figure 2.3), where at fixed age (which fixes the evolving masses) and chemical composition the position depends on the luminosity and on the effective temperature. Periods and luminosity amplitudes can be arranged in the so-called Bailey's diagram, and they are linked to the structural parameters mass, luminosity, effective temperature and chemical composition. CMDs show that RR Lyrae stars are located in a well-defined region that is the intersection of the Horizontal Branch, which is populated by core helium-burning structures, with the Cepheid Instability Strip (IS), one of the regions of the CMD where stars are pulsationally stable. The physical reasons for the pulsation instability will be discussed in section 2.3. Bailey's diagram shows that RR Lyrae stars populate two distinct regions: this occurrence, together with the different shape of light curves, led to the classification of RR Lyrae in three

different types, namely a-type, b-type and c-type (Bailey & Pickering 1902). Subsequently a-type and b-type variables where recognized as a single class, leading to the current classification in RRab and RRc type stars. RRab stars are characterized by "saw-tooth" light curves, with steep rise and less steep decline; RRc have almost sinusoidal light variations. Schwarzschild (1940), on the basis of theoretical models, realized that RRab pulsate in the fundamental mode, while RRc stars are first-overtone pulsators.

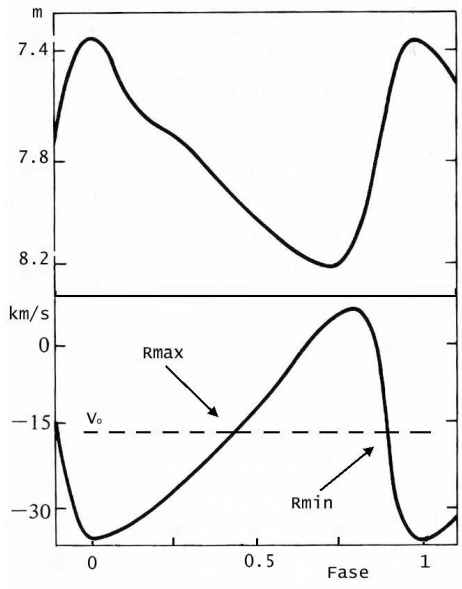

Figure 2.1 Behavior of the light curve (upper panel) and of the radial velocity curve for a typical radial pulsator. The dashed line in the lower panel shows the atmospheric zero velocity: the non vanishing value is due to the radial component of the motion of the star. The plot clearly shows that light variations are due to variations in the radial velocity, i.e. to a radially moving atmosphere. Figure from Rose (1973).

Figure 2.2 shows the Bailey's diagram for RR Lyrae stars in the Galactic Globular Cluster M5 (upper panel) and their position in the (B-V)-V CM diagram (lower panel). As shown in the figure, RRc type stars are bluer (i.e. hotter) than RRab stars. Finally, it is worth noting that amplitudes and periods are not quantities affected by usual observational uncertainties, such as distance and reddening. Table 2.1 summarizes the average properties of RR Lyrae stars.

Pulsation period	P = 0.2-0.85 days
Mean V magnitude	$\langle M_V \rangle = +0.6 \pm 0.2$
Mean effective temperature	$\langle T_{eff} \rangle = 6000 - 7300$ K
Mean gravity	$\langle \log g \rangle = 2.5 - 3.0$
Metallicity	$[Fe/H] \sim 0.0 \ldots - 2.5$
Mass	$M \sim 0.6 - 0.8 M_{\odot}$
Radius	$R \sim 4 - 6 R_{\odot}$
Luminosity	$L \sim 40 L_{\odot}$

Table 2.1. Main physical properties of RR Lyrae stars. Table adapted from Smith (1995).

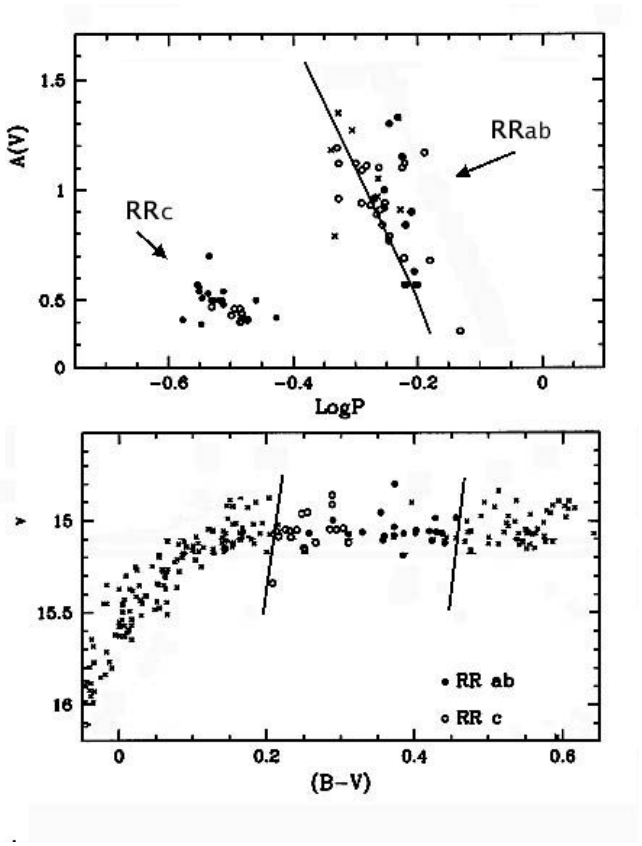

Figure 2.2. Upper panel: Bailey's diagram for the RR Lyrae stars in M5. RRab and RRc stars are located into twodifferent locations in this plane. Lower panel: the same stars in the CM diagram. Filled and open circles depict RRab and RRc stars, respectively. The two solid lines display the predicted edges of the Instability Strip, which hosts RR Lyrae stars. Plot from Caputo et al. (1999).

2.2 Evolutionary properties

Stars with masses ranging between 0.5 and $3\,M_{\odot}$ are usually referred as low-mass stars (V. Castellani, in preparation). These stars spend a substantial fraction of their life burning hydrogen in their cores. In the CM diagrams, stars in this evolutionary status arrange themselves into a mono-parametric sequence, called the Main Sequence (MS, fig. 2.3). If a simple stellar population is considered (i.e. stars coeval, sharing the same chemical composition and at the same distance), the positions of the stars along the MS depend on stellar mass, being stars with lower masses fainter and cooler. The MS phase ends when stars exhaust the most (about 90%) of their central hydrogen. Starting from this point, the He core contracts and becomes electron-degenerate, and the outer envelope expands, while the Hydrogen is still burning in a shell: stars begin the so-called Red Giant phase, and in the CMD they climb the Red Giant Branch (RGB). During this evolutionary stage, the helium-core increases its mass with the helium produced in the hydrogen-burning shell, heating up. The outer envelope expands more and more, and red giants become brighter. The RGB phase ends when cores are massive enough (about $0.5\,M_{\odot}$) to effectively ignite the helium burning (at a temperature of 10^8 K), via the 3α process. The ignition of the 3α abruptly removes the electron degeneration and produces a phenomenon called the helium-flash. In the CMD, stars leave the RGB and they place themselves along the Zero Age Horizontal Branch (ZAHB), a sequence characterized by a constant luminosity, and by a spread ($\approx 30,000$ K) in temperatures. Now, since the RGB phase is faster (of about a factor 30-100) than the MS phase, at the tip of the RGB, where the helium flash is produced, stellar masses tend to be the same. Therefore, if no other phenomenon occurs, stars should arrange themselves into a narrow sequence in the ZAHB. Oddly enough, CMDs for several Galactic Globular Clusters show extended HBs, thus suggesting the occurrence of a spread in the envelope masses, produced by mass-loss phenomena. However, it is worth noting that the observed spectra on RGB stars suggest a smaller rate for the mass-loss than that required to explain the observed temperatures spread along the HB. The spread in the temperatures is therefore a spread in the envelope masses, with smaller masses on the blue side of the ZAHB. Starting from ZAHB, stars evolve off-ZAHB, following their evolutionary tracks and becoming more luminous. Figure 2.4 shows that, at a fixed metallicity, there is a fixed range of the stellar masses for which an HB star shows up as a RR Lyrae star, since its position on the ZAHB is inside the IS, while stars with masses smaller or

larger of this range can enter the IS during their evolution, from the hot side or from the cool side, respectively. Evolved RR Lyrae stars are more luminous than ZAHB up to 0.25 mag in the *V*-band, and this is an important point to take into account when they are used as distance indicators (Bono 2003; Cacciari & Clementini 2003).

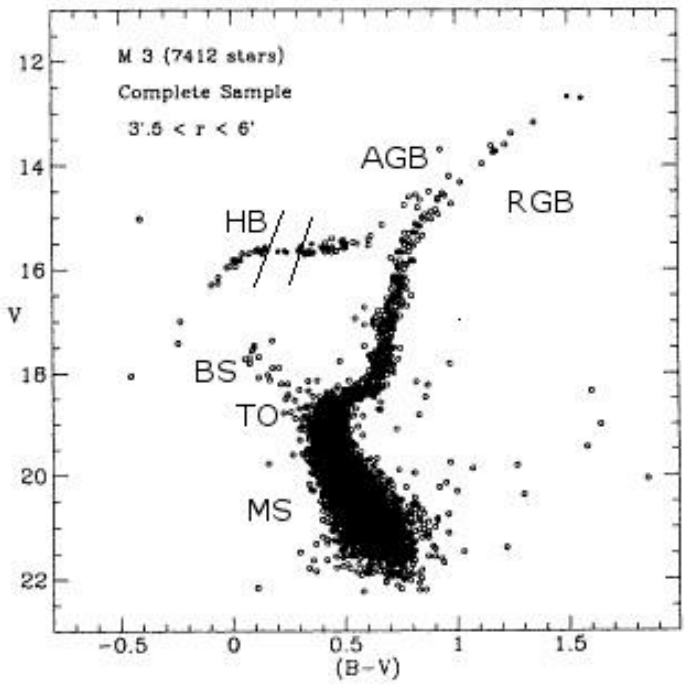

Figure 2.3. Color-Magnitude diagram for the Galactic Globular Cluster M3. The principal evolutionary phases, discussed in the text, are labeled. The two solid lines on the HB mark the edges of the Instability Strip. Blue Stragglers (see CMDs in chapter 4) are labeled with BS. Photometry from Buonanno et al. (1994).

2.3 Pulsation physics

2.3.1 Generalities

The main aim of the pulsation theory is to describe the physics of pulsations and to explain why some stars pulsate and some others do not. This approach is based on an artificial perturbation of a static stellar envelope, leaving the equilibrium condition, and to investigate whether the perturbation grows or it is damped. From first linear computations (Zhevakin 1953), more and more sophisticated codes have been developed: at the present time, non-linear, non-local, time-dependent convective treatment of stellar pulsation can predict not only periods and

pulsation amplitudes, but also the observed light curves (Bono, & Stellingwerf 1994; Bono et al. 1997). Figure 2.5 shows the agreement between models and observations for the RR Lyrae star U Comae (Bono, Castellani, & Marconi 2000). Moreover, theoretical models reproduce the position and the width of the IS in the CM diagram, and its topology. As shown in the fig. 2.6, the IS is made of a region populated by fundamental pulsators, limited by the Fundamental Blue Edge (FBE) and the Fundamental Red Edge (FRE), and a region populated by first overtone pulsators, marked by the First Overtone Blue Edge (FOBE) and the First Overtone Red Edge (FORE). The two regions intersect in the OR zone, where either fundamental or first overtone pulsators can exist. According to current empirical and theoretical evidence, this region is crucial to explain the so-called "Oosterhoff dichotomy", (see section 2.5). Moreover, the OR zone can be populated by stars which simultaneously pulsate in the fundamental and in the first-overtone: these stars are called RRd stars (Nemec 1985).

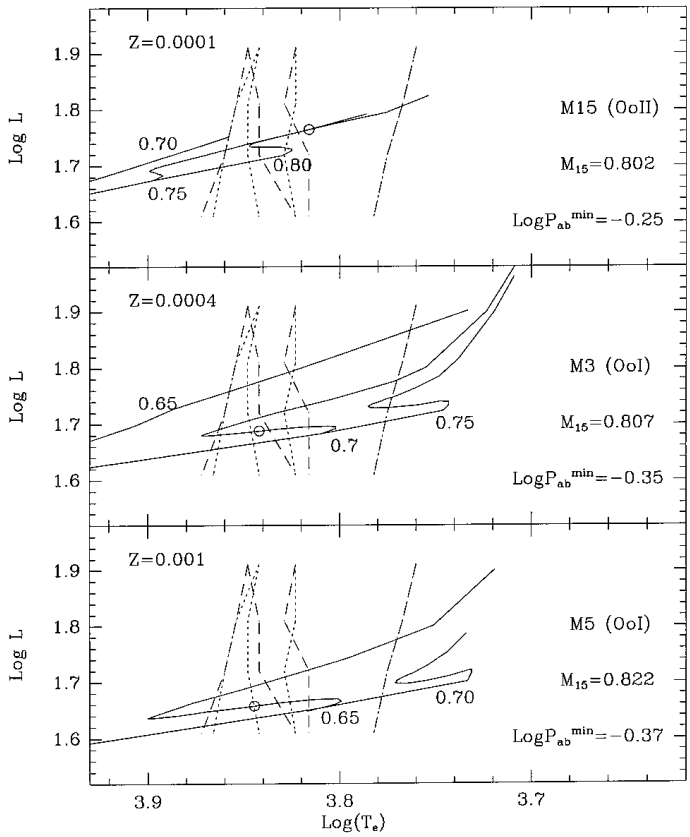

Figure 2.4. Evolutionary track (solid lines) for low-mass stars, for three different metallicities. Outer dashed lines mark the edges of the Instability Strip, while the inner lines mark the edges of the fundamental pulsators, the first-overtone pulsators, and the OR zone (see section 2.3 for details). Plot from Bono et al. (1997).

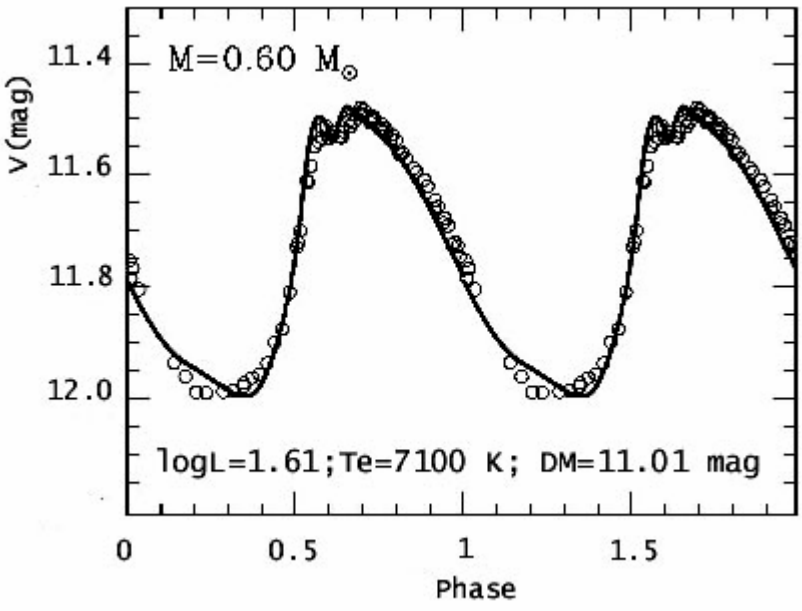

Figure 2.5. Comparison between observations (empty circles) and theoretical prediction (solid line) for the light curve of the RR Lyrae star U Comae. Physical parameters used for the fit are listed. Figure adapted from Bono, Castellani, & Marconi (2000).

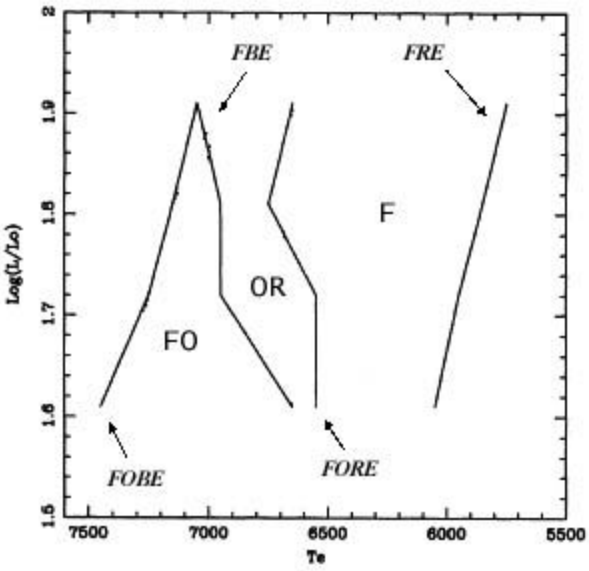

Figure 2.6. Topology of the Instability Strip. Outer edges of the IS are the FOBE on the hot side, and the FRE on the cool side. FBE and FORE mark the blue edge and the red edge of the fundamental and first overtone pulsators, respectively. The two regions intersect in the OR region, where the two pulsational modes can exist. Plot from Bono, Caputo, & Marconi (1995).

2.3.2 Kappa and Gamma mechanisms

The physical mechanism at the basis of the stellar pulsation was suggested in 1926 by Eddington, who called it the "valve mechanism". The idea is to see if a layer in the atmosphere releases heat during the compression stage, or retains it. In the latter case, the layer contributes to the instability of the structure. Such a behavior is tied to the opacity κ of the layer. When a Kramer opacity is considered, $\kappa \sim \rho^r / T^s$, $r \approx 1$ and $s \approx 3.5$ for a layer where no important element is undergoing partial ionization. This means that during an adiabatic compression the opacity decreases, since

$$\frac{d\kappa}{\kappa} = \left[r - s(\gamma - 1) \right] \frac{dT}{T}$$

and $\gamma \geq 4/3$ is the adiabatic coefficient. Thus, the heat is released and the layer is pulsationally unstable. However, in a region where an abundant element is partially ionized, *s* becomes very small or even negative, and the opacity increases with the temperature (King & Cox 1968). This accounts for the Eddington's valve, and it is called the κ–mechanism. Zhevakin (1953; 1959) singled out that the layer responsible of the instability is the zone of second ionization of helium (in a range of temperature between 30,000 and 60,000 K). This result was subsequently confirmed by Baker & Kippenhahn (1962) and by Cox (1963). Therefore, the pulsation instability is a phenomenon that interests only the outer layers of the stellar atmosphere. Theory also shows that HeI and the H ionization layers, at temperatures of 13,000 and 17,000 K respectively, play a role in the onset of the pulsations (e.g. Bono & Stellingwerf 1994). Figure 2.7 shows the structure of a HB stars, with the stratification in mass, density, and temperature. Ionization zones for H and HeI are also depicted.

The second main mechanism, connected with the ionization zones in RR Lyrae stars, that contributes to the instability is the γ–mechanism. In this case, the energy that normally would raise the temperature is absorbed by the ionizing matter, lowering the adiabatic exponent γ. Therefore, the layer tends to absorb heat during compression, leading to a driving force for the pulsations (King & Cox 1968). It is evident that the two mechanisms are connected each other.

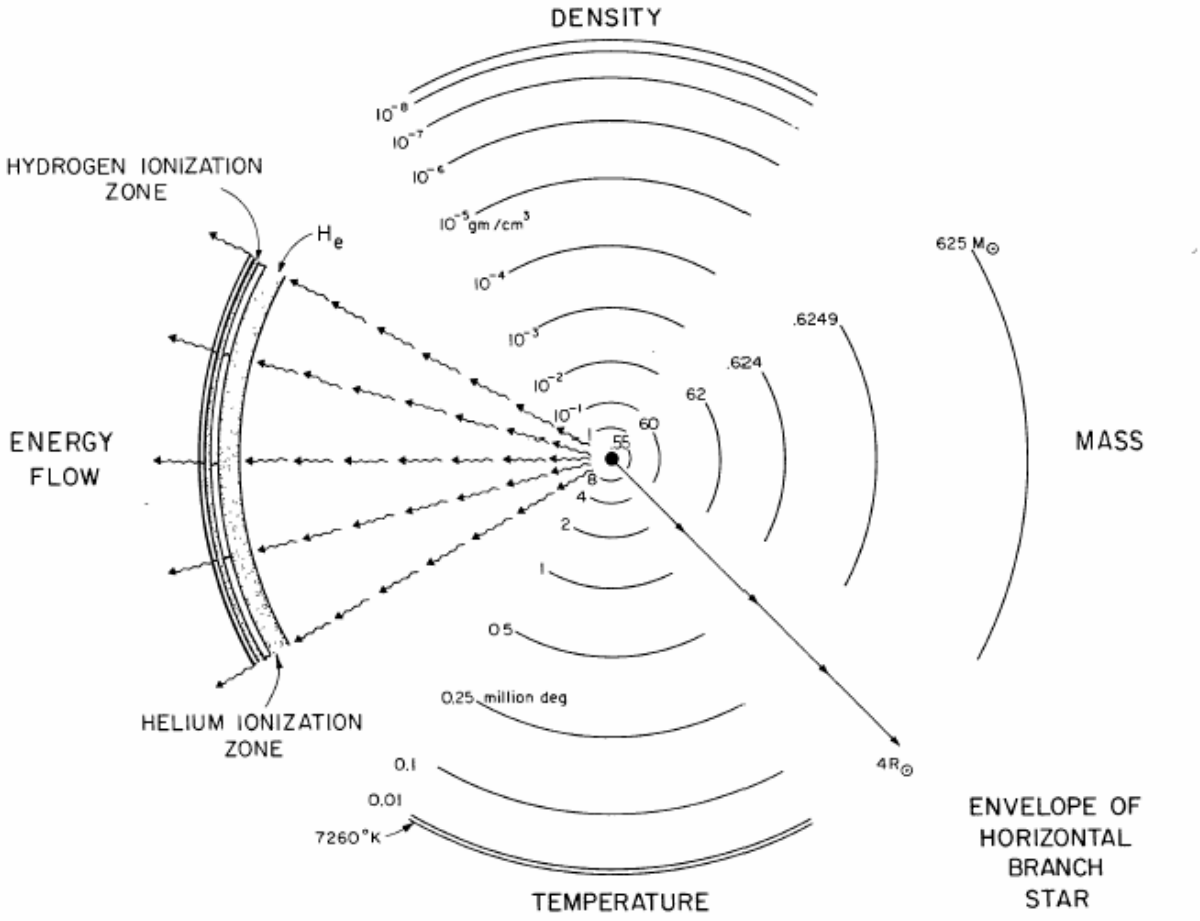

Figure 2.7. Internal structure for a $0.625M_\odot$ ***Horizontal Branch star. Stratification in mass, density and temperature is shown. Helium and Hydrogen ionization zones are also shown. Figure from Iben (1974).***

As previously outlined, RR Lyrae stars can pulsate in the fundamental or in the first overtone. Models show that the choice of the pulsation mode relies on the minimization of the integral of the mechanical work needed to keep that mode pulsationally stable: starting from the FOBE, at a fixed luminosity level, the condition of minimum energy supports the first overtone, which is characterized by a "node" (a zero-velocity layer) in the atmosphere. Moving to the cooler side of the IS, the node moves toward layers of smaller density, until it reaches a layer of too low density and disappears. Therefore, the star switches to fundamental mode (Bono & Stellingwerf 1994).

It has also been claimed that RR Lyrae can pulsate in the second overtone mode (e.g. Demers & Wehlau 1977; Soszynski et al. 2003). Unfortunately, no definitive observational

evidence is available, nor the second-overtone RR Lyrae stars, sometimes called RRe, are predicted by theory.

The last aspect that pulsation physics is able to explain is the width of the IS in the HR diagram: stars bluer than the FOBE cannot pulsate because the ionization zone is too close to the surface, thus its envelope mass is too low to effectively retain heat and to act as a valve; on the other side, on the red edge, convection quenches the pulsation mechanism (Smith 1995). It is worth noticing that the FOBE is well defined by theory, so that it is possible to use the FOBE location in the CMDs as a distance indicator (Caputo 1997; Caputo et al. 2000), while the position of the FRE depends on the assumptions adopted to treat the convective transport.

2.4 Pulsation Periods

Pulsation periods are fundamental quantities in stellar pulsations, since they are: a) well-defined observables, which can be measured with high accuracy and do not depend on distance and reddening; b) well-defined theoretical quantities, predicted with good accuracy even with the simplest models. Indeed, since first calculations by von Ritter (1879), it is known that the period P of pulsation and mean density $\overline{\rho}$ are related by

$$P\sqrt{\overline{\rho}} = Q$$

where Q is the pulsation constant. If $\overline{\rho}$ is written as $\overline{\rho} = M / R^3$ (where M is the total mass, and R is the radius), and R is written as $R \propto \sqrt{LT^{-4}}$, it results that

$$\log P = const + \frac{3}{4}\log L - \frac{1}{2}\log M - 3\log T_e$$

At the present time, non-linear, non-local, time dependent convective models predict

$$\log P^F = 11.066(\pm 0.002) + 0.832\log L - 0.650\log M - 3.363\log T_e$$
$$\log P^{FO} = 10.673(\pm 0.001) + 0.805\log L - 0.603\log M - 3.281\log T_e$$

for fundamental and first overtone pulsators, respectively (Marconi et al. 2003). It is worth mentioning that these two equations are not directly comparable with observations, since *L, M,* and T_e are not observable quantities. Observations yield magnitudes and colors, which can be related to luminosities and effective temperatures via bolometric corrections and color-temperature transformations. Stellar masses are estimated from evolutionary predictions. For example, using *B, V* photometry and transforming the equations above in the observational plane, one obtains

$$\log P^F = -0.612(\pm 0.002) - 0.340 M_V - 0.663 \log M + 1.307(M_B - M_V)$$
$$\log P^{FO} = -0.762(\pm 0.001) - 0.340 M_V - 0.643 \log M + 1.381(M_B - M_V)$$

where M_V and M_B are the absolute magnitudes in the *V* and *B* bands, respectively.

In fact, there is only one case in which masses can be estimated directly from the theoretical equations, and this is the case of the mixed-mode (RRd) pulsators: indeed, the pulsator must obey to the same time two equations, therefore individual masses can be inferred from, provided that luminosities and temperatures are estimated from observations.

In some cases it is useful to consider together fundamental and first overtones pulsators: in these cases, first overtones are "fundamentalized", i.e. the constant 0.127 (the mean difference between $\log P^F$ and $\log P^{FO}$) is added to their $\log P^{FO}$ (Di Criscienzo, Marconi, & Caputo 2004). A more accurate relation is $\log P^F = 0.147 + 1.033 \log P^{FO}$ (Marconi et al. 2003).

2.5 The Oosterhoff dichotomy

It has long been known (Oosterhoff 1939) that Galactic globular clusters can be classified in two distinct groups, on the basis of the mean period of their RRab pulsators and on the percentage of RRc stars with respect to the total number of RR Lyrae stars (fig. 2.7, right panels). Oosterhoff type-I clusters (OoI) are characterized by a smaller number of RRc stars (20%) and by a shorter RRab mean period, $< Pab >= 0.55$ days. The prototype of this class is the GGC M3. OoII clusters show a larger number of RRc pulsators (40%) and a longer RRab mean period, $< Pab >= 0.64$ days. The template of this group is the GGC M15.

Subsequent works have highlighted that, besides such dichotomy, OoI and OoII GGCs show also a dichotomy in the metal content, having OoI clusters a metallicity higher than OoII ([Fe/H] ~ -1.5 vs. ~ -2; Kinman 1959).

The dichotomy in mean periods has been explained with a difference in luminosities: indeed, from the equations of pulsation, longer periods imply higher luminosities, the other parameters being fixed. This explanation is known as the Sandage' "period shift effect" (e.g. Sandage 1990). The main problem with this interpretation is that it is at odds with predictions of evolutionary theories and with chemical enrichment models: indeed, to have higher luminosities, OoII clusters should have higher helium fraction than OoI clusters, therefore showing an anti-correlation between helium and metals content (Gratton, Tornambè, & Ortolani 1986).

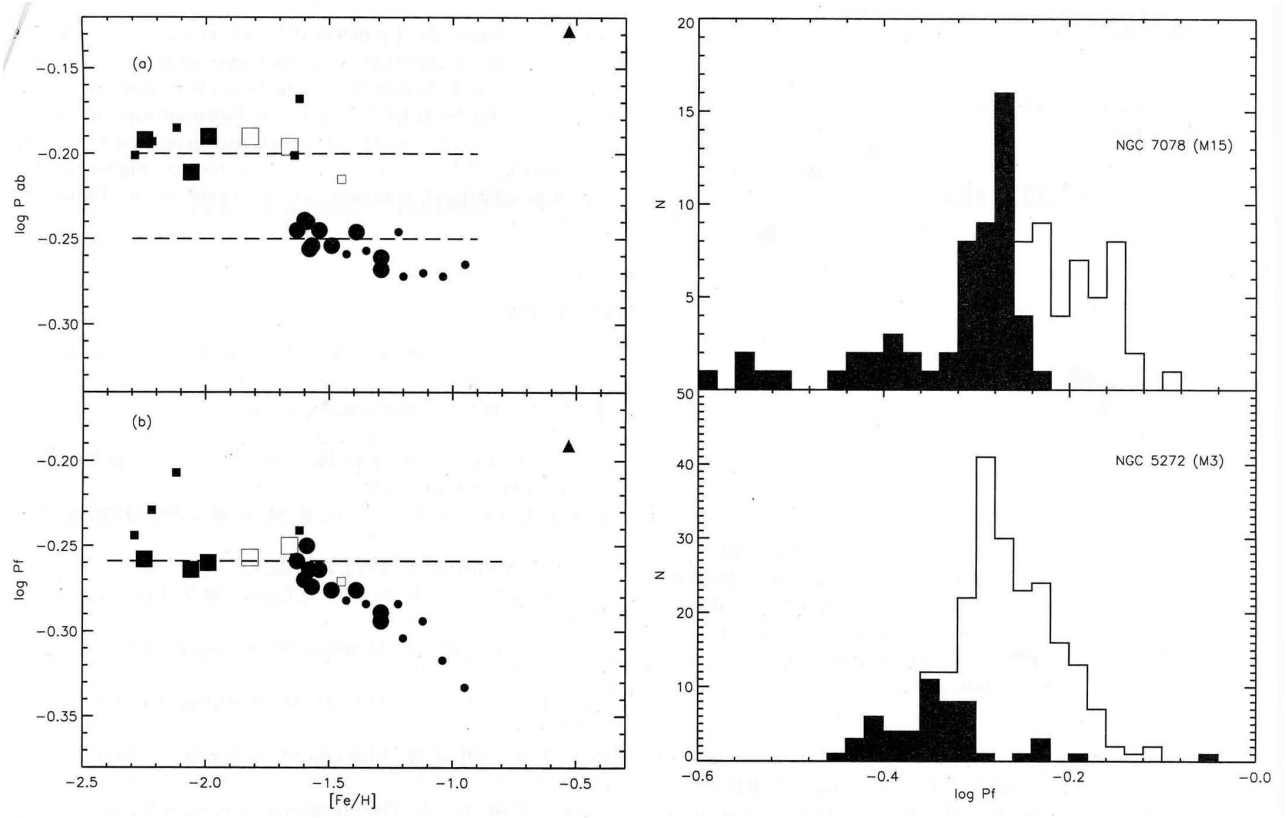

Figure 2.7. Left panels: fundamentalized periods histograms for the GGC's M 15 and M 3. The fraction of RRc stars changes when moving from OoI clusters (M 3) to OoII clusters (Oo II). Right panels: distribution of the mean periods of RRab stars of a sample of Galactic Globular Clusters as a function of the metallicity. In the upper panel it is evident the dichotomy of the distribution; such a dichotomy disappears when fundamentalized periods are used (lower panel). Figure from Castellani, Caputo, & Castellani (2003).

The other explanation was proposed by Van Albada & Baker (1973), who assumed the existence of a hysteresis mechanism in the IS, according to whom the mode of pulsations depends

on the evolutionary path in the IS. In this model, RRab stars that enter the OR zone from the red side, save their pulsation mode until they reach the FBE; conversely, RRc stars that enter the OR zone from the blue side keep the pulsating first overtone mode until they reach the FORE. Therefore, if the OR zone is populated mainly by RRab stars, and since period is a strong function of temperature, $< Pab >$ will be shorter and the cluster will be an OoI type; on the other hand, if the OR zone is populated mainly by RRc stars, $< Pab >$ will be longer and the cluster will be an OoII type. It is worth noting that with the Sandage's hypothesis, the difference is on a star-by-star basis, while with the Van Albada & Baker mechanism the difference arises from sample properties. A test of this latter hypothesis can be made using the fundamentalized periods: if the hysteresis mechanism is correct, then the difference between OoI and OoII clusters should disappear, because the difference in the period distribution between RRab and RRc stars disappears. Indeed, figure 2.7 (panels *a* and *b*) shows that fundamentalized periods are the same from [Fe/H] ~ -2.2 to ~ -1.5, hence supporting the hysteresis mechanism.

At the present time, Oosterhoff dichotomy seems to be a phenomenon connected only with the Galaxy, since other galaxies in the Local Group show intermediate properties between the two Oosterhoff types (as in dwarf spheroidals, Mateo 1998; Dall'Ora et al. 2003, and references therein), or a continuum in the RR Lyrae pulsation properties as in the Large Magellanic Cloud (Smith 1995; and references therein).

2.6 The Blazhko effect

The so-called "Blazhko effect" (Blazhko 1907) is a modulation of the light curves (changes in the maxima and minima), with a periodicity that ranges from about ten to few hundreds days, that seems to affect mainly RRab stars.

The physical reasons of such a modulation are still unknown. Here, we mention the phenomenon because it complicates the estimate of the mean magnitudes and colors of the observed RR Lyrae stars, i.e. the quantities that are compared with theoretical predictions.

2.7 Mean magnitudes

In comparing observations with theory, it is important to bear in mind that magnitudes and colors used in the theoretical relations are *static*, i.e. they are the magnitudes and the colors that the star would have if it was a static star. Magnitudes and colors derived from observations are *mean* quantities, obtained averaging in some way the observed light curves. Usually, the average can be performed in magnitudes or in intensities. Figure 2.8 shows the differences in the V band between static and mean magnitudes, averaged both in intensities and in magnitudes, and between magnitude-averaged and intensity-averaged magnitudes as a function of the amplitude, for fundamental (left panels) and first-overtone pulsators (right panels).

Figure 2.8 discloses that the key element that governs the differences is the morphology of the light curves, i.e. large-amplitude, asymmetrical light curves tend to produce larger differences, while low-amplitude, sinusoidal light curves show almost negligible differences between static and averaged quantities. This follows from the fact that in calculating the averages, a logarithmic and a more sensible linear scale are adopted for the magnitude-averaged and for the intensity-averaged quantities, respectively. Since, at fixed effective temperature, the amplitude decreases from *B* to near-infrared bands, it follows that in the *K*-band these differences are marginal.

2.8 RR Lyrae stars as distance indicators: the M_V-[*Fe/H*] relation

2.8.1 Pros and Cons

As previously outlined, RR Lyrae stars are excellent distance indicators for old stellar populations, since they are bright, are easily recognizable and show an almost constant *V* magnitude. Usually, *V* band luminosity of the RR Lyrae stars is calibrated as a linear function of the *metallicity* [Fe/H]:

$$M_V = \alpha + \beta\ [Fe/H]$$

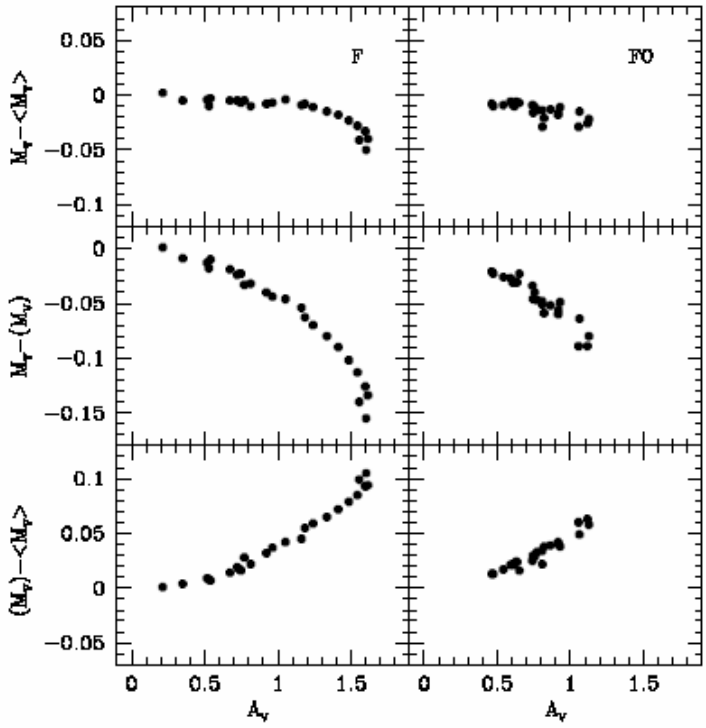

Figure 2.8. Upper panels: differences between static and intensity-averaged mean magnitudes in the V-band for Fundamental (F) and First Overtone (FO) pulsators as a function of the pulsation amplitude. Middle panels: the differences between static magnitudes and magnitude-averaged mean magnitudes. Lower panels: differences between magnitude-averaged mean magnitudes and intensity-averaged mean magnitudes. Plot from Marconi et al. (2003)

This relies on the fact that V magnitudes and [Fe/H] ratios are easy observables, but unfortunately no general agreement has still been reached both on the slope and on the zero point of this relation. Indeed, recent evaluations for α cover an interval of about 0.3 mag, while the values of the slope β range from ~0.13 to ~ 0.30 mag dex^{-1} (Di Criscienzo, Marconi, & Caputo 2004). Moreover and even more importantly, theoretical calibrations of the (M_V-[*Fe/H*]) relation supply magnitudes that are systematically brighter $\approx$ 0.15 mag than empirical calibrations, revealing the existence of poorly-known systematic effects. As a consequence, at given metallicity, a spread is found up to ≈ 0.3 mag (Bono et al. 2003, Bono, 2004). The use of the (M_V-[*Fe/H*]) relation to calibrate RR Lyrae luminosity is hampered by the following problems:

- evolutionary effects: theoretical models yield the luminosity on the Zero Age Horizontal Branch. However, during their evolution, RR Lyrae stars become brighter, introducing an uncertainty in the *V* magnitude up to 0.25 mag. Moreover, theoretical and empirical evidence suggest an increase in the spread of the intrinsic ZAHB luminosity moving from metal-rich to metal-poor GGCs. Therefore, actual luminosity of RR Lyrae stars depends on their evolutionary status, as well as on the ZAHB morphology. This problem is even more striking with field RR Lyrae stars, for which no evidence on their evolutive status is available;
- linearity: as evidenced in Castellani, Chieffi, & Pulone (1991), Caputo et al. (2000), and Layden (2002), the (M_V-[*Fe/H*]) relation is not strictly linear, but there is a change of slope at [*Fe/H*] ~ -1.5. A quadratic curve seems to be more appropriate to fit the data. It is worth noting, however, that recent photometric and spectroscopic observations (Clementini et al. 2003) in the LMC do not confirm the change of slope at [*Fe/H*] ~ -1.5;

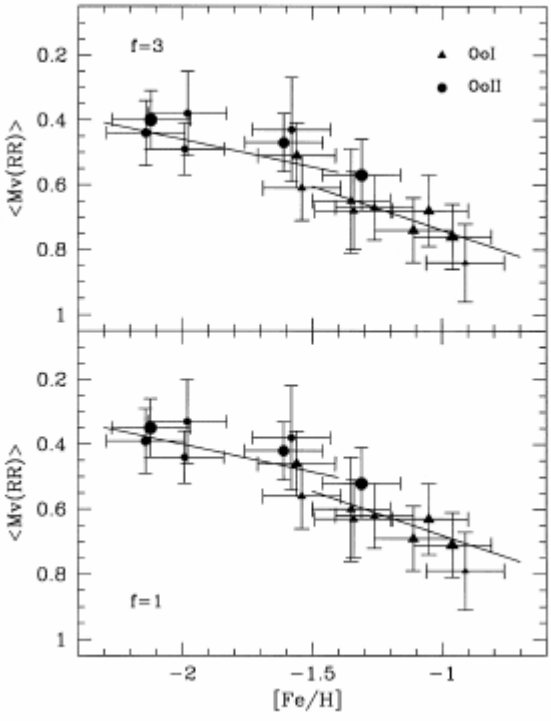

Figure 2.9. Distribution of the mean absolute V-magnitudes as a function of the metallicity for a sample of Galactic globular clusters. Filled triangles depict OoI clusters, while filled circles mark OoII clusters. Solid lines show the change of slope in the $M_V - [Fe/H]$ ***relation. Plots have been produced for a solar-scaled composition (f=1, lower panel) and for an*** α***-enhanced chemical composition (f=3, upper panel). Figure from Caputo et al. (1997).***

- metallicity: usually, the metal content of the stars is evaluated with the iron-to-hydrogen ratio [*Fe/H*], with the implicit assumption that other elements change in lockstep with iron; this assumption appears to be too simplistic, since it is known that metal-poor stars show an overabundance of the α-elements (the so-called *α-enhancement*) with respect to iron (see, e.g., King 1999). RR Lyrae spectra are quite complex (Smith 1995; Bono 2003 and reference therein) and hence it is difficult to estimate their [*Fe/H*] content; moreover, such estimates are usually based on the Preston's Δs index (Preston 1959), or on the *hk* index (Anthony-Twarog et al. 1944; Rey et al. 2000): the main problem is that such indexes are based on the calcium abundance, which is an α-element. Finally, there is the fundamental problem of the *calibration* of the metallicity scale: the Zinn &West (1984) and the Carretta & Gratton (1997) scales show in the intermediate metallicity range a difference of the order of 0.2 dex (Rutledge, Hesser, & Stetson 1997; Kraft & Ivans 2003). Note that the zero-point of the M_V-[Fe/H] relation is generally estimated at [Fe/H]=-1.5, and therefore current uncertainties on the metallicity scale might introduce an error of the order of 0.04 mag. However, Kraft & Ivans (2003) proposed a new metallicity scale, which agrees quite well with the Zinn & West scale in the range $-1.7 < [Fe/H] < -1$, but it gives metal abundances that are 0.2–0.3 dex lower at both higher and lower metallicities.

2.8.2 Outline of the current calibrations

Without entering into a detailed discussion, current calibrations can be divided in two groups: the "observational route" and the "theoretical route" (Smith 1995). In the first group mainly fall calibrations based on statistical parallaxes solutions (in which distance-dependent proper motions or proper motions dispersions are compared with the distance-independent radial velocities or radial velocities dispersions), Baade-Wesselink solutions (in which the linear radius variation, estimated from the velocity curve, is compared with the angular radius variation, estimated from the light curve), main sequence fitting of Galactic globular clusters and calibrations based on independent distance estimates of the Large Magellanic Cloud. Following Cacciari & Clementini (2003, and references therein), statistical parallaxes give $M_V = 0.78 \pm 0.12$ mag at $[Fe/H] = -1.5$; Baade-Wesselink solutions can be summarized with

$M_V = (0.20 \pm 0.04)[Fe/H] + 0.98(\pm 0.05)$ (Fernley et al 1998); main-sequence fitting yields results such as $M_V(RR) = 0.61(\pm 0.07)$ mag at $[Fe/H] = -1.5$ (Gratton et al. 2003). Calibrations of the absolute magnitude of the RR Lyrae $M_V(RR)$ based on the distance of the LMC have to been consciously considered, since the distance of LMC is mainly fixed on the Cepheids Period-Luminosity relation, but its zero-point is calibrated with the Galactic Cepheids. Moreover, the Cepheids PL relation may not to be universal, as e.g. suggested in Tammann, Sandage, & Reindl (2003), but could have a dependence on the metallicity (Romaniello et al. 2005; and references therein). For the theoretical route, HB models still depend on the input physics, and the calibrations based on them show a spread up to 0.2 mag, as illustrated in figure 2.10. Theoretical calibrations can be based not only on the evolutionary models, but also on the pulsation models: this point will be discussed in the next two paragraphs.

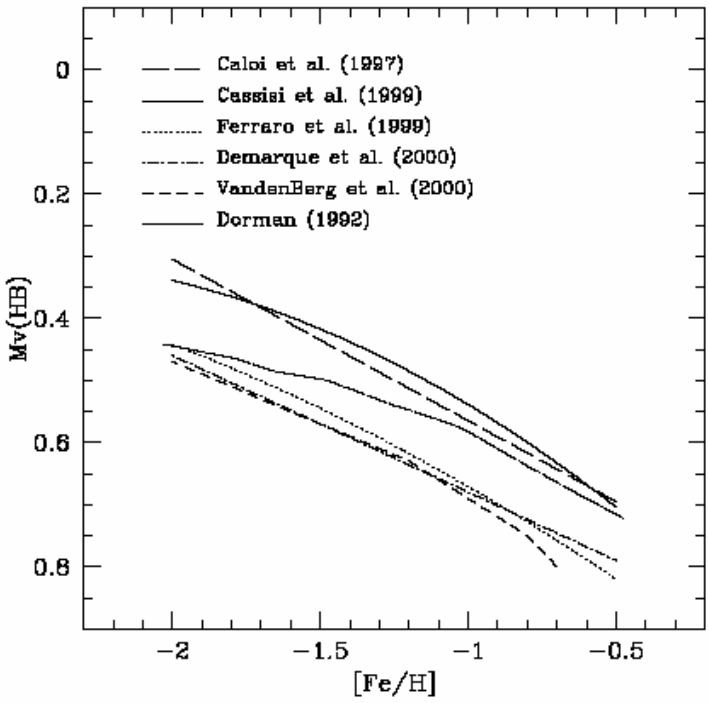

Figure 2.10. Absolute V-magnitudes for HB models as a function of the metallicity. Different models are plotted, with different input physics. The spread is up to ≈ 0.25 mag. Plot from Cacciari & Clementini (2003).

2.9 RR Lyrae stars as distance indicators: the FOBE method

Non-linear, non-local, time-dependent pulsation theory predicts with good accuracy the blue edge of the IS, since the uncertainty on the convection efficiency, usually treated with the free parameter l / H_p, is small compared to the red edge of the IS. Indeed, current models predict, for $l / H_p = 1.5$ and for a fixed Z=0.001, that the absolute magnitude of the FOBE is

$$M_V^{FOBE} = -1.193(\pm 0.034) - 2.230 \log M - 2.536 \log P^{FO}$$

(Marconi et al. 2003); if $l / H_p = 2.0$ is adopted, the absolute magnitude of the FOBE changes of only +0.05 mag, while the same change in the convection produces a change in the magnitude of the FRE of -0.14 mag (Marconi et al. 2003). This characteristic makes the location of the FOBE in the CM diagram an attractive distance indicator (Caputo 1997; Caputo et al. 2000). The essential requirement to apply this method is to have a well-populated IS, i.e. this method is useful only with homogeneous populations (as globular clusters and old components of dwarf spheroidal galaxies) with a significant sample of RRc stars. However, it is worth noticing that this method relies on the estimate of the position of the FOBE with the bluest RRc stars: therefore, strictly speaking, this method yields only an upper limit for the distance modulus. The reliability improves if the HB is well populated, so that the difference in color between the bluest RRc stars and the first non-pulsating HB stars, hotter than the bluest RRc stars, is as small as possible.
In practice, it is convenient to fix the mass from evolutionary models, and to express the magnitude as a function of the metal abundance

$$M_V = -0.78 - 2.255 \log P + 0.151 \log Z$$

(Caputo et al. 2000) and where the metal fraction Z can be related to the observable [Fe/H] ratio by

$$\log Z = [Fe / H] - 1.70$$

(simply scaling the solar chemical composition, with $Z_{\odot} = 0.02$ [1]) or by

$$\log Z = [Fe/H] - 1.70 + \log(0.638 f + 0.362)$$

when the ratio f of α-elements respect to iron is taken into account (Salaris, Chieffi, & Straniero 1993). The intrinsic accuracy of the FOBE relation is $\sigma_V = 0.065$ mag. As a matter of example, Figure 2.11 shows the FOBE method applied to RRc stars belonging to the Carina dwarf spheroidal galaxy (Dall'Ora et al. 2003).

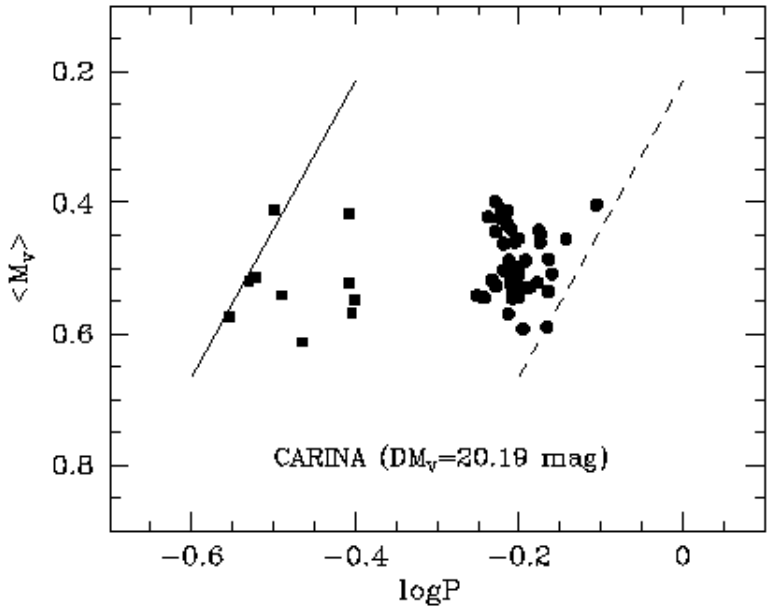

Figure 2.11. Distribution of the dSph Carina RR Lyrae stars in the $M_V - \log P$ plane. Observed apparent magnitudes were shifted to match the FOBE of the IS. The shift is the estimated distance modulus. Figure from Dall'Ora et al. (2003).

2.10 RR Lyrae stars as distance indicators: the *PLK* relation

2.10.1 Empirical evidence and theory

Empirical evidence shows (Longmore et al. 1986; 1990) that RR Lyrae stars follow, in the *K*-band, a rather tight period-luminosity relation (*PLK*). This empirical finding was subsequently

[1] Solar chemical abundances have recently been revised by Asplund, Grevesse, and Sauval (2004). They found $Z_{\odot} = 0.012$. If confirmed, this new value would slightly affect *absolute* distances, while *relative* distances would stay unaltered.

theoretically supported by Buckley, Longmore, & Dixon (1992), who combined the pulsation equations by Van Albada & Baker (1973) with the horizontal branch models of Lee & Demarque (1990). Figure 2.12 shows their theoretical relation obtained for three different values of the stellar masses. Moreover, they took into account the effect of the evolution: figure 2.12 shows quite clearly that the evolutionary effects have a small impact on the magnitude, since they introduce a scatter of about 0.1 mag.

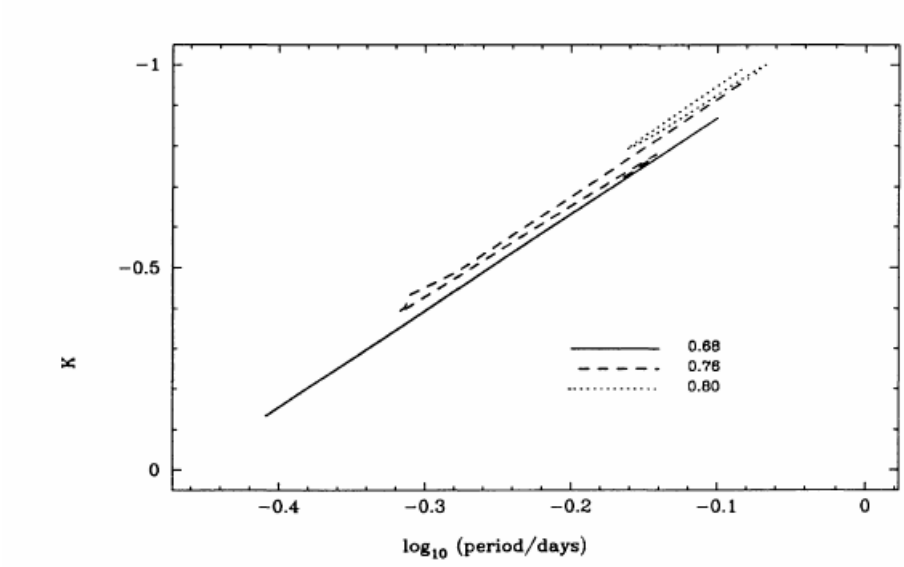

Figure 2.12. Theoretical PLK relations for the three labeled masses and for two luminosity levels. Figure from Buckley, Longmore, & Dixon (1992).

On the basis of more sophisticated theoretical models, these findings were subsequently confirmed and refined by Bono et al. (2001, hereafter B01). In Figure 2.13 absolute *V* and *K* magnitudes are plotted as a function of *log*P, for a fixed chemical composition and for three different values of the luminosity. The *V* magnitude is strongly dependent on the luminosity level, since a variation of 0.1 dex implies a variation of 0.25 mag; on the other hand, the same luminosity change implies in the *K*-band a variation both in the *K*-magnitudes and in the periods, and the net effect is that the *PLK* relations of bright and faint pulsators agree with each other, within 0.1 mag. It is evident that in the *V* band RR Lyrae stars do not follow any period-luminosity relation. The physical reason is that in the *K* band the bolometric correction strongly depends on the effective temperature (i.e. on the period, having fixed the other parameters) while in the *V*-band the bolometric correction is nearly constant. Figure 2.14 shows the behavior of the bolometric correction with the temperature for the photometric bands *V, I,* and *K*. The bolometric

correction starts to show a linear and significant dependence on the temperature only with the *I*-band, and the effect is maximum in the *K* band. It is worth noting that, although *K* magnitudes depend on the chemical composition (figure 2.14) this effect is smaller than in the *V* band. If one starts from the pulsation equation (for example, for the fundamental pulsators)

$$\log P^F = 11.066(\pm 0.002) + 0.832 \log L - 0.650 \log M - 3.363 \log T_e$$

(Marconi et al. 2003) and neglects the effect on the period of luminosity and mass (in the previous relation the coefficients are quite small compared to the coefficient of the temperature), the period mainly depends on the effective temperature and, in turn on the bolometric correction.

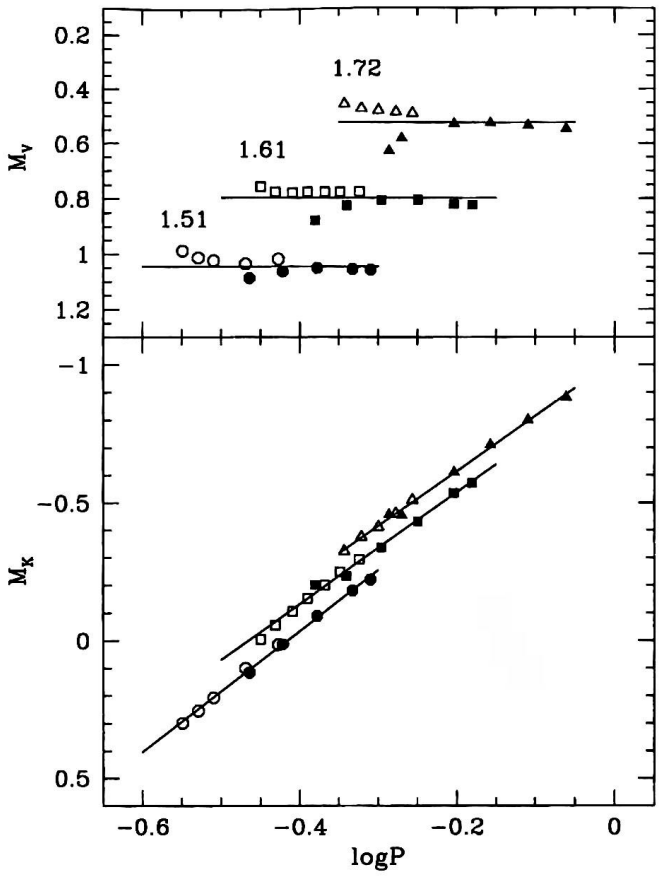

Figure 2.13. Upper panel: predicted V-band absolute magnitudes for fundamental (filled symbols) and first overtone (empty symbols) pulsators, for a fixed chemical composition (Y = 0.24, Z = 0.001) and mass ($M = 0.65 M_\odot$), but with different luminosity levels. Lower panel: same as in the upper panel, but for K-band absolute magnitudes. Figure from Bono et al. (2001).

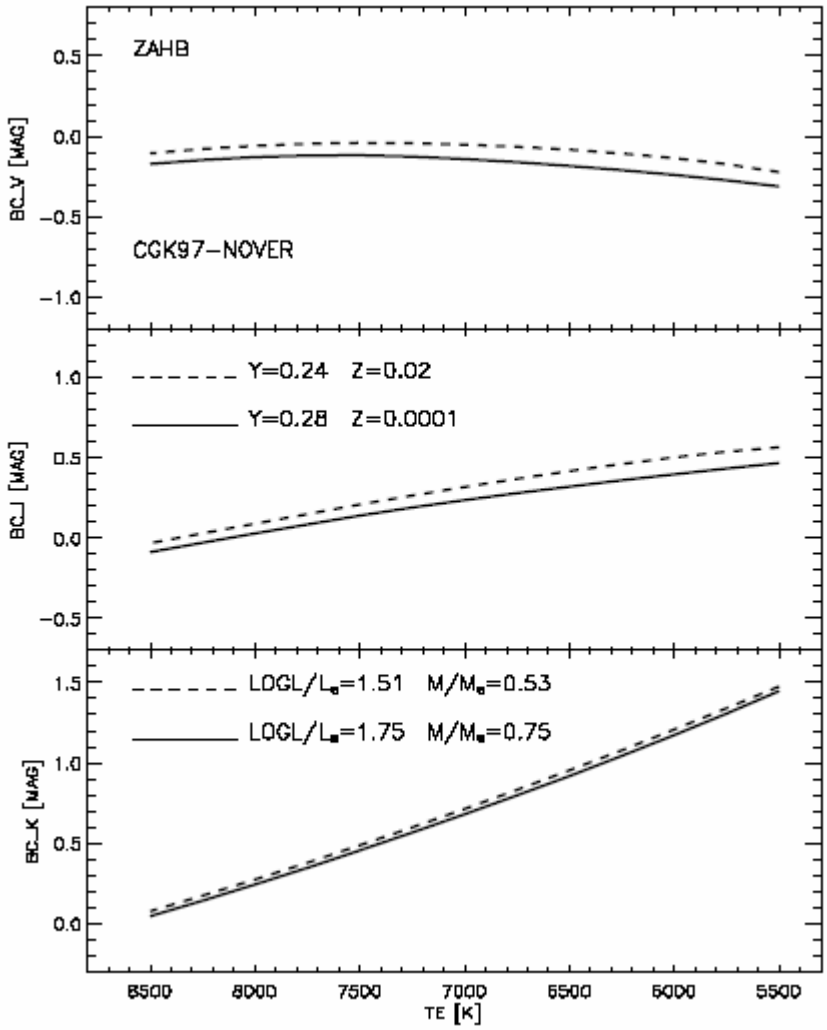

Figure 2.14. Predicted bolometric correction as a function of the effective temperature for the labeled values of helium, metallicity and mass in the* V *(upper panel),* I *(middle panel), and* K*-band (lower panel). Figure from Bono (2004).

Figure 2.15 shows the dependence of V and K magnitudes on the stellar masses: the luminosity level is fixed ($\log L/L_{\odot} = 1.61$), and two values of masses have been plotted (0.625 and $0.675\,M_{\odot}$), considered representative of the spread in masses for RR Lyrae stars in a GC at $\log Z \approx -3$ (see figure caption for details). In particular, *PLK* relation is only marginally affected by a spread in masses, and indeed a variation of 8% in mass introduces, at fixed period, a variation of ~0.06 mag.

By adopting the mass of the ZAHB models (Bono et al. 1997) located in the middle of the IS (i.e. at $\log T_e \sim 3.85$, Bono et al. (2001) found the relation

$$M_K = 0.568 - 2.071 \log P + 0.087 \log Z - 0.778 \log L$$

where the periods are fundamentals or fundamentalized. Estimating the luminosity level on the basis of the log$L$(ZAHB)-log$Z$ calibrations provided by (Bono et al. 1997; Cassisi et al. 1998; 1999), one obtains the relation

$$M_K = 0.139 - 2.071(\log P + 0.30) + 0.167 \log Z$$

with the intrinsic accuracy of $\sigma_K = 0.037$ mag.

The previous equation can be rewritten as

$$M_K = -0.766 - 2.071 \log P + 0.167[Fe/H]$$

and compared with the empirical calibrations available in the literature, based on the Baade-Wesselink luminosity calibrations of field RR Lyrae stars

$$M_K = -0.647 - 1.72 \log P + 0.04[Fe/H] \quad \text{(Longmore et al., 1990)}$$
$$M_K = -0.76 - 2.257 \log P + 0.08[Fe/H] \quad \text{(Liu \& Janes, 1990)}$$
$$M_K = -0.72 - 2.03 \log P + 0.06[Fe/H] \quad \text{(Jones et al., 1992)}$$

It is worth noticing that the theoretical relations have all been obtained on a solar-scaled mixture (i.e. without α-enhancement).

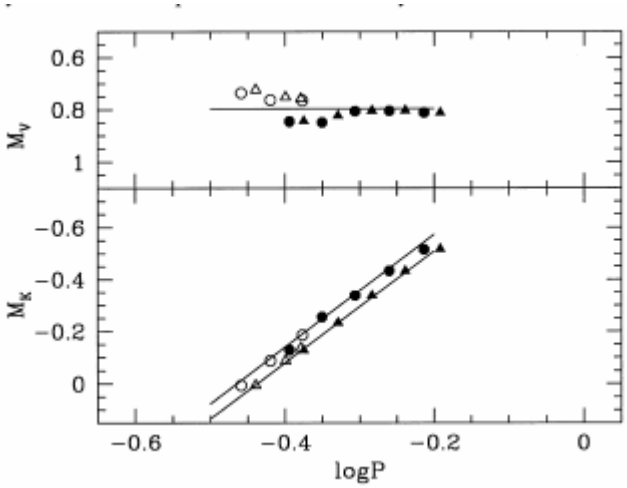

Figure 2.15. Predicted absolute magnitude in the* V *(upper panel) and in the* K*-band, as a function of the pulsation period. The luminosity is fixed, $\log L / L_{\odot} = 1.61$***, and two different mass values are adopted, namely*** $0.625 M_{\odot}$ ***(triangles) and*** $0.675 M_{\odot}$ ***(circles). Figure from Bono et al. (2001).***

Theory has been validated on RR Lyr itself by Bono and coworkers (2002): the pulsation parallax (i.e. the parallax that a star, with the estimated distance, should have), obtained with the *PLK* relation, was compared with the trigonometric measure obtained by Benedict et al. (2002) using the interferometer on board of the Hubble Space Telescope. In particular, the *PLK* estimate $\pi_{puls} = 3.858 \pm 0.131$ mas is in excellent agreement with the measured value $\pi_{trig} = 3.82 \pm 0.20$, but with a smaller formal error. The estimate of the pulsation parallax relies on the comparison between the *K* band absolute and de-reddened apparent magnitudes. Unfortunately, RR Lyrae is located at low Galactic latitude and its reddening is poorly known, ranging from $E(B-V) \approx 0.03$ to $\approx$ 0.06 mag. This means, following the relations provided by Cardelli, Clayton, & Mathis (1989), that the absorptions in the *V* and *K* band range from $A_V = 3.1 \times E(B-V) \approx 0.09$ to ≈ 0.18 mag, and from $A_K = 3.1 \times 0.11 \times E(B-V) \approx 0.01$ to $\approx$ 0.02 mag, respectively. As shown in Bono et al. (2003), the pulsation parallax is only moderately dependent on the absorption (figure 2.16, upper panel), decreasing with increasing A_V; however, pulsation-based estimates are within the error bar of the HST measurements.

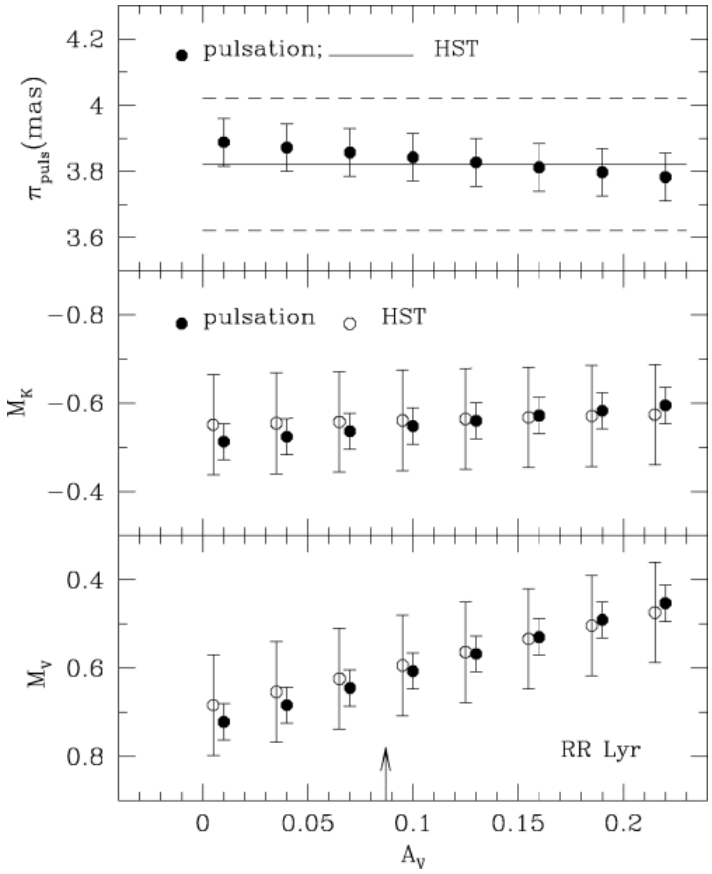

Figure 2.16. Top panel: predicted pulsation parallax for RR Lyr (filled circles), as a function of the visual extinction. Solid and dashed lines show the HST direct measurement and the relative uncertainty, respectively. Middle panel: comparison between* K *magnitudes of RR Lyr based on HST trigonometric parallax (open circles) and on the pulsation approach (filled circles), as a function of the visual extinction. For the sake of clarity, HST data have been slightly shifted along the x-axis. Bottom panel: the same as the middle panel, but for absolute visual magnitude. Plot from Bono et al. (2003).

Middle and bottom panels of figure 2.16 show the dependence on the absorption of the absolute *K* and *V* magnitudes, respectively. Data in both panels show that the empirical determination of the absolute magnitude is still hampered by the uncertainty in the HST measurement, even if the absorption was firmly known.

2.10.2 *PLK* relation: fine tuning

Relations provided Bono et al. (2001) were provided only for fundamental pulsators and, although *PLK* is moderately dependent on the pulsator mass, and the quoted equations were obtained by fixing only a reference mass, in the middle of the IS.

On the basis of a finer grid of pulsation models, Bono et al. (2003) derived new theoretical relations, both for fundamental and first overtone pulsators. The equations they obtained are

$$M_K^F = 0.511 - 2.102 \log P + 0.095 \log Z - 0.734 \log L - 1.753 \log M / M_r$$
$$M_K^{FO} = -0.029 - 2.265 \log P + 0.087 \log Z - 0.635 \log L - 1.633 \log M / M_r$$

with a rms scatter of σ = 0.016 mag. In these equations, M_r is a reference mass, function of the metal content, and M is the model mass, that can be inferred from HB evolutionary models. Reference masses (in solar units) for different metals and helium abundances are listed in the table 2.2, partially reproducing Bono et al. (2003) table 1.

Once the reference mass is included in the above equations the masses predicted from ZAHB models for fundamental and first overtone pulsators, at logT_e = 3.80 and 3.85, respectively

$$M_K^F = 0.565 - 2.101 \log P + 0.125 \log Z - 0.734 \log L$$
$$M_K^{FO} = -0.016 - 2.265 \log P + 0.096 \log Z - 0.635 \log L$$

with a rms of σ = 0.031 and 0.025 mag, respectively.

Z	***Y***	***M_r***
0.0001	0.24	0.75
0.004	0.24	0.70
0.001	0.24	0.65
0.06	0.255	0.58
0.01	0.255	0.57
0.02	0.28	0.53

Table 2.2. Input parameters for the grid of the models used by Bono et al. (2003). Masses are in solar units

Following the same procedure outlined above, Bono et al. derived

$$\left(M_V - M_K\right)^F = 4.014 + 1.986 \log P - 0.134 \log Z - 1.662 \log L + 1.656 \log M / M_r$$
$$\left(M_V - M_K\right)^{FO} = 5.195 + 2.518 \log P - 0.159 \log Z - 2.158 \log L + 1.815 \log M / M_r$$

or, fixing the mass as in the *PLK* relations,

$$\left(M_V - M_K\right)^F = 3.963 + 1.986 \log P - 0.162 \log Z - 1.662 \log L$$
$$\left(M_V - M_K\right)^{FO} = 5.180 + 2.518 \log P - 0.168 \log Z - 2.158 \log L$$

with an intrinsic dispersion of 0.037 and 0.031 mag, respectively. These equations are particularly useful, since if one fixes the luminosity level they can be used as an independent check on the estimated distances with the *PLK* relations. Moreover, and even more importantly, due to their strong dependence on the luminosity level, they can be used to give an estimate of the luminosity *L*, to use therefore in the *PLK* equations.

Catelan, Pritzl, & Smith (2004), on the basis of synthetic HB computations, studied the behavior of the Period-Luminosity relation in several bandpasses, from *U* to *K*. They accounted for the evolutionary effects and the spread in masses by considering several HB morphologies, which can be described with the Lee-Zinn ratio $(B-R)/(B+V+R)$, where *B* and *R* are the number of stars on the blue side and on the red side of the IS, respectively, and *V* is the number of RR Lyrae stars. For the *K* band, they found the average (i.e. not depending on the specific HB morphological type) relation

$$M_K = -0.597 - 2.353 \log P + 0.175 \log Z$$

which is similar to that found by Bono et al. (2001), but with a slope slightly steeper: in terms of zero point, at the representative values $P = 0.50$ d and $Z = 0.001$, the above relation provide a magnitude 0.05 mag brighter than B01.

A very similar approach was adopted by Cassisi et al. (2004), who found slopes ranging from $\alpha = -2.30$ to $\alpha = -2.41$.

2.10.3 The M_K-[*Fe/H*]-log *P* relation

In the above equations the metallicity is treated with the mass fraction *Z*. Unfortunately, this is a not an observable parameter, but it is estimated from the observed quantity [Fe/H]. It is worth to recall that [Fe/H] actually is *not* the real metallicity of the star, being neglected the abundances of other elements, such as α-elements. Nevertheless, since the α-enhancement is of the order of 0.3-0.4 dex, the difference between [Fe/H] and the global metallicity [M/H] is of the order of ≈ 0.2-0.3, and the [Fe/H] ratio is currently adopted as metallicity indicator, since it is relatively ease to get even from photometric observations. To study the $M_K - [Fe/H] - \log P$ relation, B03 chose a set of RR Lyrae stars for which accurate *V* and *K* magnitudes were available, as well as with reliable evaluations of the reddening and metallicity. (*V-K*) colors were used to estimate the luminosity level, and then their absolute *K*-band magnitude was estimated with the *PLK* relation. They found a very tight relation between M_K and $[Fe/H]$ ratio, i.e.

$$M_K + 2.101 \log P = -0.770(\pm 0.044) + 0.231(\pm 0.012)[Fe/H]$$

Note that the dependence on the metallicity is steeper than in the purely theoretical relation, where the metallicity is given with the mass fraction *log* Z (in that case the slope was 0.125, or 0.167 when the theoretical B01 relation is considered). To check the occurence of systematic uncertainties on the distance scale based on the B03 *PLK* semi-empirical relation, Dall'Ora et al. (2004b) performed a comparison between the distance moduli of four Galactic Clusters estimated with the Baade-Wesselink calibration and with the FOBE method (only for three of them, in this latter case), with the distance modulus estimated with the B03 semi-empirical calibration. Results are summarized in table 2.2, which reproduces their table 2. Table 2.2 clearly shows that the most discrepant results are with the most metal-poor clusters, especially if the comparison with the results from the Baade-Wesselink method is considered. The trend is weaker with the FOBE.

Object	[Fe/H][a]	E(B-V)[b]	<V>[c]	σ_V	μ_0 (BW)[d]	μ_0 (FOBE)[e]	μ_0 (K)[f]	$\Delta\mu_0$[f]	$\Delta\mu_0$[f]
Ω Cen	-1.62	0.12	14.57	0.12	13.57±0.16	…	13.77±0.04	0.20	…
M 3	-1.57	0.01	15.61	0.12	14.94±0.16	14.97±0.07	15.15±0.16	0.21	0.18
M 5	-1.27	0.03	15.06	0.08	14.26±0.13	14.28±0.07	14.37±0.09	0.11	0.09
M 15	-2.26	0.10	15.82	0.08	15.01±0.13	15.17±0.07	15.32±0.10	0.30	0.15

Table 2.3. ***a) Mean cluster metallicity according to Harris (1996)***
b) Cluster reddning according to Harris (1996)
c) Mean visual magnitude according to Ω Cen, Olech et al. (2003); M3, Corwin & Carney (2003); M5, Caputo et al. (1999); M15 Silbermann & Smith (1995)
d) True distance moduli based on the Baade-Wesselink calibration provided by Fernley (1994)
e) True distance moduli based on the FOBE method suggested by Caputo et al. (2000)
f) True distance moduli based on the* K*-band mean magnitudes for RR Lyrae stars collected by Longmore et al. (1990) and the semi-empirical relation derived by B03
g) Difference in distance moduli between the* PLK *relation and the BW method
h) Difference in distance moduli between the* PLK *relation and the FOBE method
Table from Dall'Ora et al. (2004b)

Chapter 3
Data reduction

In this chapter will be discussed the observing strategies and data reduction techniques used in the present work. A brief introduction on the near-infrared arrays and on the problems in observing in the near-infrared bands with ground-based telescopes will be given.

3.1 Near-Infrared arrays

Near-Infrared arrays are imaging devices developed starting from the second half of 80's. Typical dimensions are of 1024 × 1024 pixels, and only recently 2048 × 2048 pixels arrays become available to the astronomical community.

The physical bases of the IR arrays are the same of visual CCDs, both being based on the photoelectric effect, but construction and operation differs in several significant aspects.

IR arrays are made with semiconductors with a small energy gap between the valence and conduction bands (in order to allow infrared low-energy photons to excite electrons). The side effect is that electrons can be excited into the conduction band not only by photons, but also by thermal energy. As a consequence, IR arrays must be operated at temperatures (about 60 – 80 K for HgCdTe detectors) much lower with respect to CCDs. Moreover, in order to reduce the thermal background as much as possible, they must also be extremely well baffled by cold (typically 77 K) surfaces to admit only the solid angle subtended by the telescope optics.

From the structural side, current technology does not allow to build IR detectors that function adequately as shift registers and amplifiers: in this case hybrid arrays are adopted, made of a detector array and of a readout array (multiplexer), assembled separately, aligned and joined. It is worth noting that the multiplexer, although made of silicon is not a CCD, but for noise-reduction reasons it consists of individual amplifiers for each pixel. This set-up has several

advantages, since each pixel is effectively isolated from his neighbors: this eliminates annoying effects seen in CCDs, such “blooming” (i.e., the overflowing of photoelectrons from one pixel to neighbors) and “charge trail” or “bleeding” (the loss of charges along a column during the reading stage), because each pixel is read separately and there is no charge transfer from one pixel to another.

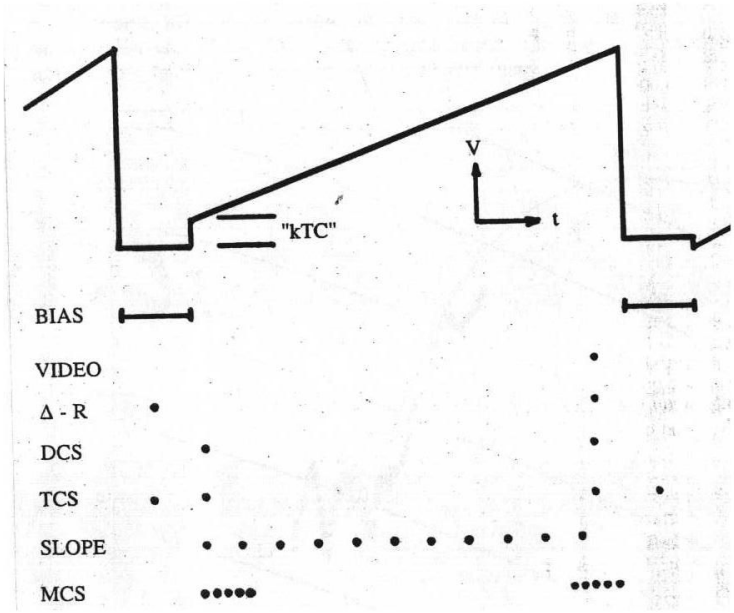

Figure 3.1. Representation of the voltage of the single pixel as a function of time. The “double correlated sampling” technique, described in the text, is labeled with DCS. The* kTC *noise is shown. Figure from Joyce (1992).

3.2 Array operation

As mentioned, IR arrays are made of pixels that are isolated from neighbors and that are read separately. Therefore, the readout process is non-destructive because it does not affect the charge on the pixel and hence it can be carried out at any time.

As in CCDs, the pixels are made of diode junctions that act as capacitors, on which the voltage is function of the collected charges. The adopted sampling technique is based on the assumption that charge and voltage on the pixel follow a linear relation. This is certainly not the case if the pixel is saturated, but even in normal operating limits, there is a slight voltage

dependence on the diode capacitance. This means that the full dynamic range is not effectively usable, but only the region well below the saturation limit. For example, with SOFI (available at the ESO/NTT telescope) the 1.5% level of non-linearity is reached under 10,000 ADUs.

Figure 3.1 shows a schematic representation of the voltage on a pixel as a function of time. At the beginning of an integration, the voltage is set to a pre-selected bias level. When the reset switch is open, the voltage may shift to a new value and then increase linearly with time as charge is collected by the diode junction. The offset after biasing is a random uncertainty, which depends on temperature *T* and capacitance *C*, ("*kTC* noise", as outlined in the figure) in the actual charge on the diode capacitance; consequently, the offset may vary in amplitude and sign from one reset cycle to another. To overcome this problem, a technique widely used in astronomy and also used for the observations presented in this thesis work, is the "double correlated sampling", in which the array is read immediately after and before reset; the integration time is the interval between the two reads, and the signal is the voltage difference. This technique has the advantage to remove the *kTC* noise, but at the cost of $\sqrt{2}$ in read noise, since two independent readouts are made.

3.3 The sky in the Infrared

The radiation background from the sky and observing environment is much higher in the IR than in the visible. Figure 3.2 shows a plot of the measured sky brightness at the 0.9 meter KPNO telescope from 0.4 to 4 μm, in units of photons-s^{-1}- μm^{-1}-$arcsec^{-1}$. Open squares depict experimental points, while the solid curve represents the flux from a 300 K blackbody. To have an astronomical reference frame, curves of constant magnitude- $arcsec^{-1}$ are also plotted. From data plotted in the figure it is immediately clear that, starting from the *J* band (1.25 μm), the sky-background has magnitude around 15, brighter, in the majority of the cases, of the objects of astronomical interest.

Three separate factors contribute to background:

- shortward of 2.3 microns, the background is dominated by non-thermal emissions, principally by aurora, OH and O_2 molecules, excited by solar radiation during the day. Because of its atmospheric origin, this airglow background is often temporally and

spatially variable: for example, the vibrationally excited OH emissions are highly variable on a timescale of few minutes;

- longward of 2.3 μm, thermal emission from the telescope optics and obscurations (such as the spider and central obscuration), produces a background which rises very rapidly with increasing wavelength;
- finally, thermal emission from optically thick telluric absorption lines contribute to the sky background in this thermal region.

Moreover, the IR window between 1 and 2.5 μm contains many absorption features that are primary due to water vapor and carbon dioxide in the atmosphere. These features vary with time and present a non-linearly dependence on the airmass. Figure 3.3 shows the atmospheric transmission between 1 and 2.5 microns as seen from SOFI. As shown, the atmosphere is completely opaque between *J* (yellow line) and *H* (magenta line) bands, and between *H* and *Ks* (green line) bands. Moreover, the edges of these atmospheric windows are highly variable. A complete atlas of the atmospheric features can be found in Rousselot et al. (2000).

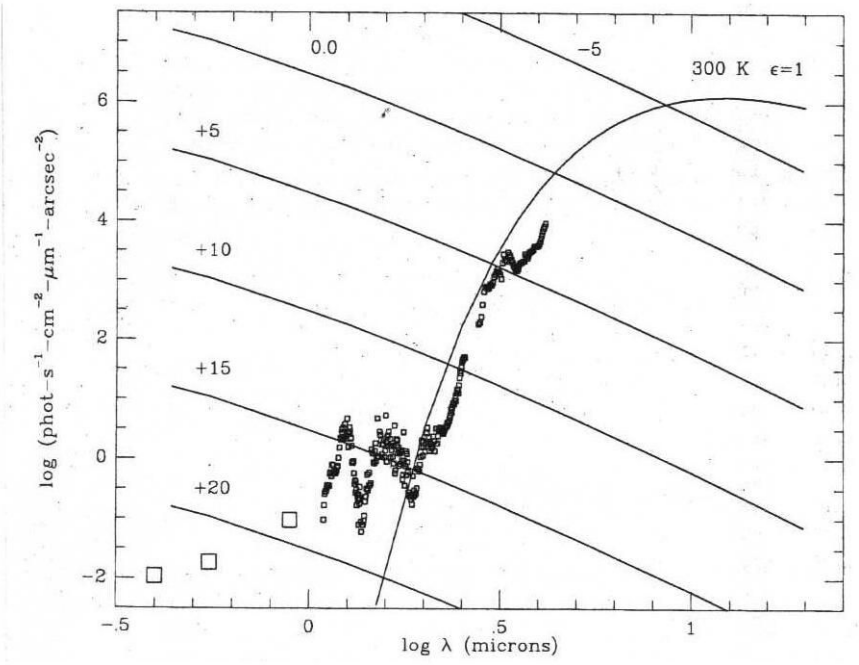

Figure 3.2. Plot from the KPNO sky brightness as a function of wavelength from 0.4 to 4μm. Solid lines are iso-magnitudes lines for the labeled values. Figure from Joyce (1992).

3.4 SOFI-Son OF ISAAC

3.4.1 Optical arrangement

Infrared data discussed in this thesis work have been collected with SOFI, the imager and spectrograph camera mounted at the Nasmyth A focus at the ESO/NTT telescope. SOFI offers four imaging modes, three spectroscopic modes and one image polarimetry mode.

Figure 3.3 shows the optical layout of the instrument: the light collected by the primary mirror is directed on the tertiary mirror and enters the front window that has no optical power; immediately after the window there is a mask wheel, at the telescope focus, that contains all the masks used for imaging and spectroscopy. The mask wheel is followed by a collimating lens, two filter wheels, a grism wheel, an objective wheel, and finally by the detector.

The imaging mode chosen for the observations is the Large Field Objective, which offers a field of view of 4.94' x 4.94', with a pixel scale of 0.288". This mode allowed us to cover the largest available field of view, thus sampling the selected clusters with a smaller number of images and hence saving telescope time. Moreover, the pixel scale is small enough to avoid problems connected with crowding, even in the very center of the clusters. Nevertheless, several images collected during nights with exceptional seeing (even less than 0.5") have star profiles slightly undersampled, complicating the estimate of the Point Spread Function (PSF).

Owing to a slight misalignment of the collimating lens, all the objectives suffer of different amounts of image degradation. In particular, large field objective is affected by a significant distortion in the bottom left and in right left corners (see figure 3.5). This distortion affects a strip of about 200 pixels wide along the x-axis, making PSF photometry a difficult task. This problem has been recently fixed, and now the image quality of SOFI is excellent.

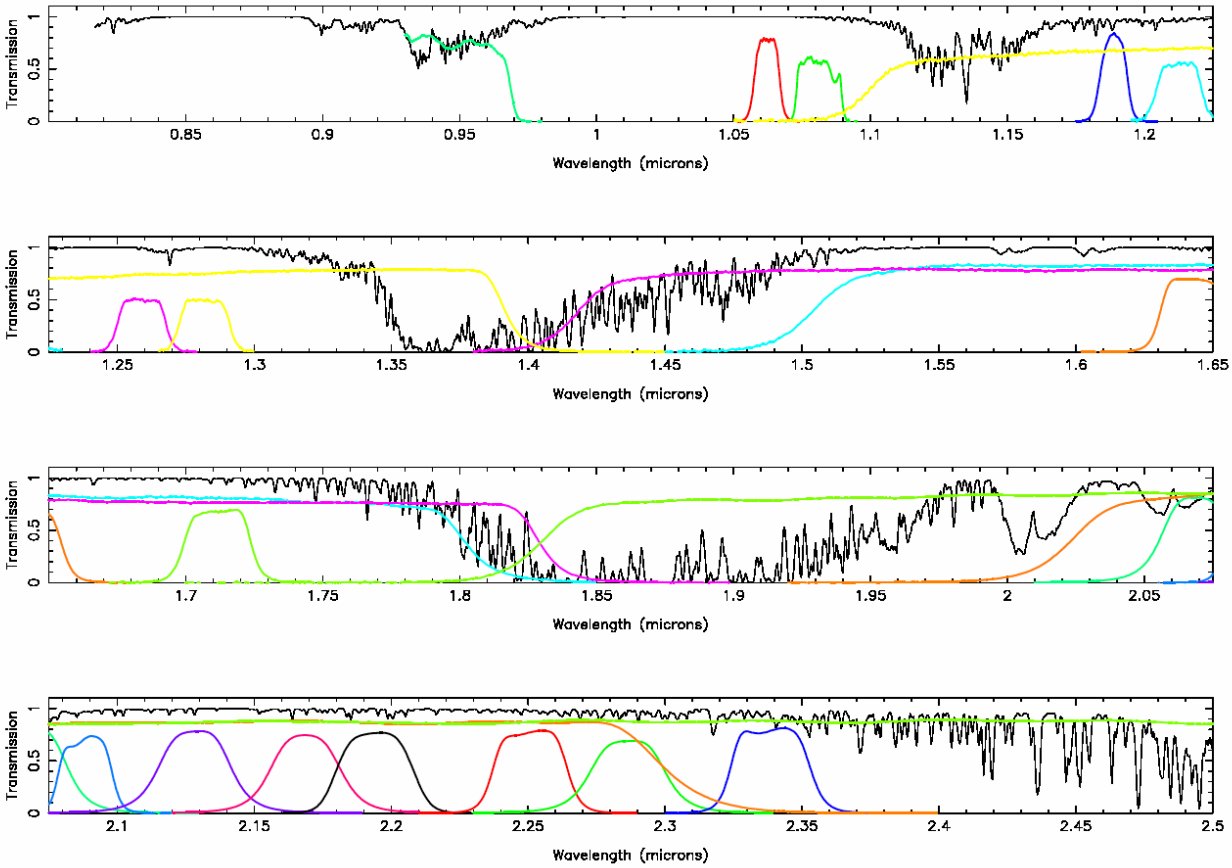

Figure 3.3. Atmospheric transmission at La Silla. Transmission curves of the filters available with SOFI are also reported. In particular, J-band is depicted with a yellow line, and Ks-band is represented with a green line. Figure from SOFI User's Manual.

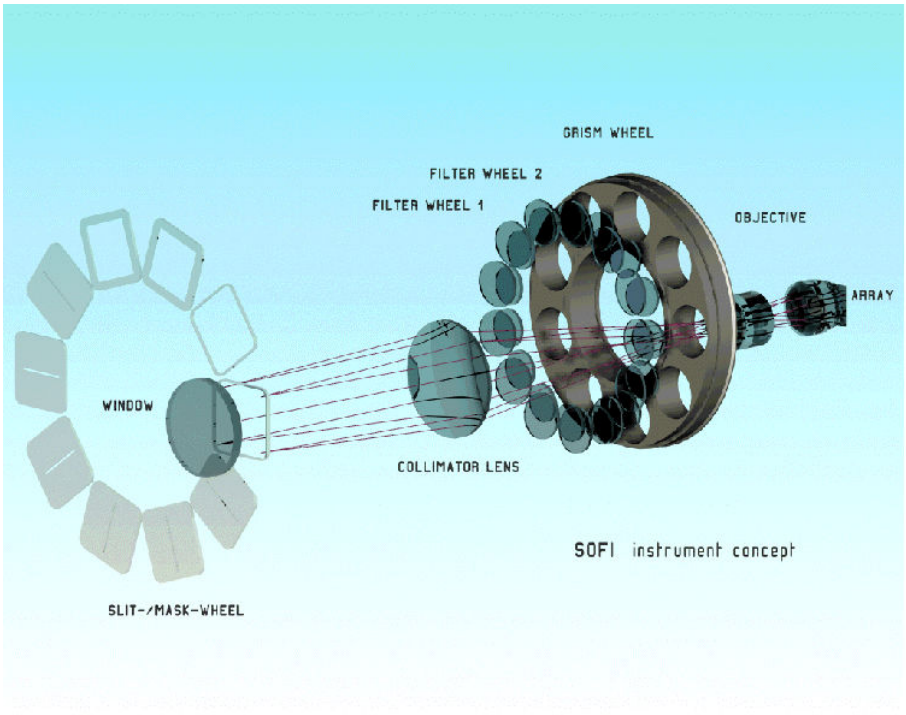

Figure 3.4. Optical layout of SOFI. See text for a detailed explanation Figure from SOFI User's manual.

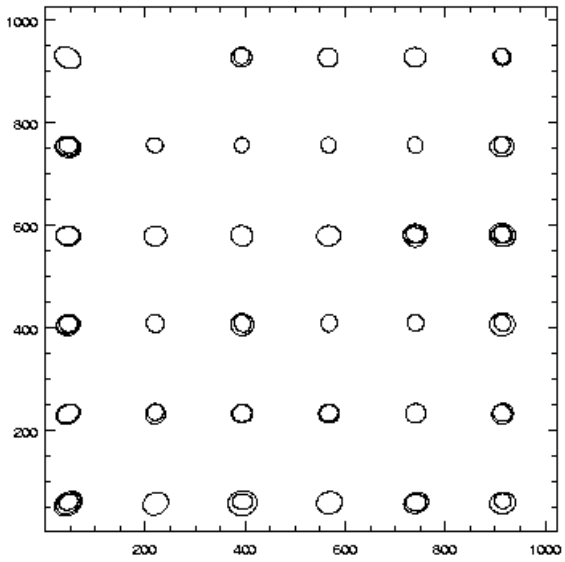

Figure 3.5. Image quality of SOFI before August 2003. As explained in the text, images appear distorted along a strip on the left side of the image. Figure from SOFI web site, http://www.ls.eso.org/lasilla/sciops/ntt/sofi/ImageQuality.htm.

3.4.2 The Detector

The detector is a Rockwell HgCdTe 1024 x 1024 Hawaii array with a pixel size of 18.5 microns. The average quantum efficiency is about 65%. The array is read in four quadrants, with a gain of 5.5 e^-/ADU and a readout noise of 12 e^- (in double correlated sampling). The full depth is of about 100,000 e^-, and the array is linear at 1% level up to ~ 60,000 e^-, i.e. up to 10,000 counts. In the SOFI user's manual (Lidman et al., 2003) it is recommended to keep the exposures short enough to avoid the background exceeds 6,000 counts, owing to a complicate dependence of the bias on the flux with backgrounds higher than this limit. The flux can reach six hundreds ADU/sec/pix during summer in the *Ks* band and with the large field objective, thus limiting the single integration to about 10 seconds.

3.5 Observational techniques in the IR

The difficulties outlined in the previous paragraphs, both instrumental and environmental, have led to the development of specific observational techniques. These techniques have mainly been devised to limit the effects of the sky background, which is generally brighter than the objects of interest and it is highly variable, both spatially and temporally. Moreover, one has to bear in mind the limitations of the detector previously discussed. These facts translate into a very careful planning of the observations. To subtract background from scientific frames it is necessary to secure a background image, and subtract the latter from the formers. The method to obtain the background image is chosen according to whether the scientific field is crowded or uncrowded or, as far as extended sources are concerned, a large or a small area is covered. For crowded fields, or for sources covering a large area, it is necessary to imagine the background separately from the scientific field, in an area close to the latter; if the field is uncrowded or the object covers a small area, the background frame can be obtained directly from the scientific frames. In collecting scientific images (and, if needed, sky images) it is mandatory to account for the physical limitations of the detector. In particular, since SOFI is linear up to 10,000 counts and it is required to keep the background under 6,000 counts, often it is necessary to split the single exposure in many single exposures (Detector Integration Time, hereafter DIT), averaged on the fly by the control system into a final frame. Therefore, the total exposure time of a single frame will be DIT seconds × NDIT (number of DITs). Moreover, to improve the quality of the scientific images, and to get a sky frame where only the background is present, it is customary to average

together several images (called NINTs, number of single frames) slightly dithered, for the scientific field as well as for the sky field. Consequently, a single image will be split in NINTs exposures, each of DIT × NDIT seconds.

The sky background is variable on a time-scale of a few minutes (five is usually a safe limit), thus it is necessary to collect images of the scientific object and of the background within this limit, or otherwise the sky subtraction will be difficult or even impossible. If one is interested in sources for which the required integration time is larger than the time range for the stability of the background, it is then necessary to split the needed exposure time in several groups of NINTs, until the requested signal to noise ratio has been achieved.

3.6 Data pre-reduction

As for visual CCDs, data pre-reduction is aimed at removing instrumental effects from scientific images, i.e. the additive offset due to the reading stage amplifiers (called the bias), the additive dark current originated from thermally excited electrons, the difference in the linear response from pixel to pixel, and the non-uniformity of the illumination of the detector. The latter two effects are corrected with the flat-field.

The usual technique adopted for visual CCDs to acquire bias and dark frames to correct for the first two effects is not useful for IR arrays, since the bias is not known a-priori and the dark frame has a complicated pattern. As a matter of fact, dark frames show a non-linear dependence on time. The signal is made of several components: a) shading, a component that depends on the DIT an on the incident flux; b) heat from the readout amplifiers; and c) classical dark current from the random generation of electron/hole pairs.

As discussed in section 3.2, the bias is automatically removed during the reading stage with the double correlated sampling technique. The dark frame is removed simultaneously with the sky background: indeed, since the sky frames are acquired with the same integration time of the scientific frames, under the same conditions and temporally close to scientific frames, they are in principle characterized by the same dark frame pattern. Hence, with the subtraction of the sky background, one also removes the dark frame.

Flat fields can be obtained either on the sky (sky flat) or on a suitably illuminated panel (dome flat). Sky flats can be obtained from twilight sky or from the observations themselves, hence producing a *local* flat that is crucial in excellent quality in the reduced images. In this case,

it is however necessary to collect a large number of images, thus this technique is not very time efficient. Dome flats are obtained exposing alternatively an illuminated ("lamp-on") and non-illuminated ("lamp-off") dome panel. Subtracting the non-illuminated exposure from the illuminated one, it will produce a dark-frame subtracted flat. It is important to note that since shading pattern, one of the components of the dark frame, also depends on the incident flux, this effect can not be perfectly removed. It remains a residual, which reveals itself as a discontinuity of few percent of the zero point across the centre of the frame. SOFI instrument scientists have developed a technique to remove this effect: in addition to usual lamp-on and lamp-off frames, images with the mask partially obscuring the array are collected. The vignetted part of the array is relatively free from scattered light, and therefore it can be used to estimate the shade pattern, calculating the difference in the region in common to both the vignetted and the unvignetted frames (fig. 3.6).

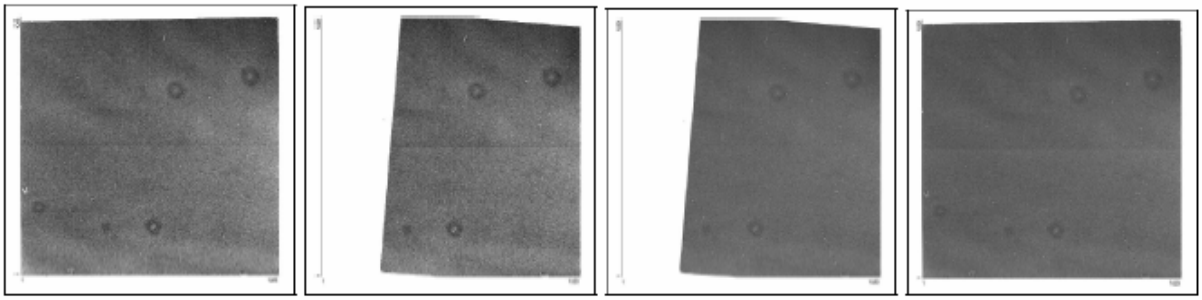

Figure 3.6. Examples of dome flats. From left to right, lamp off, lamp off with mask, lamp-on with mask, lamp on (SOFI User's manual).

Flat fields obtained with this procedure have low frequency variability between 1 and 3%. To further improve the quality of the flat field, often it is estimated the so-called "illumination correction": a bright star is observed in several positions along the frame, and a surface is fitted to the observed fluxes. The calculated plane is then multiplied by the uncorrected flat field. The corrected flat field has low frequency sensitivity better than 1%.

When bright sources are imaged, often a "ghost" is produced that affects all the lines where the source is and all the correspondent lines on the symmetric part of the detector. This effect, called the "cross talk", is not completely understood, but it is well described and corrected (SOFI's user manual, Lidman et al., 2003).

SOFI flat fields are very stable: statistics show that flat fields have a maximum deviation of the order of 4%, in the worst case, in a period of about two years with respect to an average flat field.

3.7 Photometric reduction

3.7.1 Overview

Stellar photometry can be made in two ways: the synthetic approach ("aperture photometry"), based on the integral of the counts over the area covered by the stellar image; and the analytical approach ("Point Spread Function [PSF] photometry"), based on the fitting of a well-suited analytical function to the observed stellar profiles. The first approach is the "physical" one, and produces the most accurate results with bright and isolated stars. However, in crowded fields, stellar images are partially overlapped, so it is difficult or even impossible to define an area to perform aperture photometry. Moreover, with faint sources aperture photometry is very noisy. For these reasons, when dealing with crowded fields (such as globular clusters) and/or when we are interested in faint sources, PSF photometry is preferred.

All the photometric reductions have been carried out with the DAOPHOTII/ALLFRAME packages (Stetson 1987; 1994). Details on the photometric reduction will be provided in the chapters relative to each cluster. In the following we will explain the adopted general procedure.

Point Spread Function is a function that describes how a point source (a two-dimensional delta of Dirac) is transformed in an output function by the system telescope-detector. For ground-based telescopes, PSF is also determined by the atmospheric turbulence.

The basic idea of PSF photometry is that PSF is roughly the same for all the stars present on a given frame, being its shape independent on their brightness and, as a first approximation, on their position on the frame. Therefore, if PSF is estimated from bright, non-saturated and isolated stars, this function can be used to measure the brightness of the other stars, simply taking into account their different position on the frame and the different intensity of the central peak. Usual functions used in stellar photometry are the Moffat function and the Penny function. Moffat function is described by

$$I = \frac{I_0}{(1 + a_x (x - x_0)^2 + a_{xy} (y - y_0)^2 + a_{xy} xy)^{\beta}}$$

which gives the intensity I in the point (x,y) as a function of the (measured) central intensity $I_0(x_0, y_0)$. Parameter β is usually set to 1.5, while the coefficients a are the unknown quantities calculated by the fit, i.e. the half width at half maximum in x and in y, and the position angle for the major axis of the ellipse, if the stellar images are not symmetrical. Penny function is the sum of Gaussian and a Lorentz function, with four free parameters: the half width at half maximum in x and in y; the fractional amplitude of the Gaussian function at the peak of the stellar profile; and the position angle of the tilted elliptical Gaussian. Sometimes a five parameters Penny function is used, that is a Penny function in which the Lorentz function is tilted too, but along a direction that is different from the Gaussian.

In practice, often PSF is a function of the position along the frame, so it is necessary to calculate a PSF that is variable along the frame. In such a case, the approach followed by DAOPHOT is to calculate a numerical matrix of residuals, by comparing the observed profile with the calculated one, and to correct the first analytic approximation with the computed matrix (the reasons for this choice are explained in Stetson 1987).

As shown in fig.3.5, SOFI large field imaging suffers of a degradation of the image in a strip about 200 pixels wide along the x-axis. For this reason, a variable PSF has been chosen for the photometric reductions. It is worthy noting again that, for ground-based telescopes, PSF is also a function of seeing, so the most accurate results are achieved calculating PSF for *each* frame.

3.7.2 Calculus of the PSF - DAOPHOT

The first step in the photometric reduction is to find, on each frame, the candidate sources. The search has been performed with the FIND task of DAOPHOT, finding all the peaks brighter than 3σ of the local background. Of course, several spurious identifications are made, for example galaxies and local noise peaks are identified as stars, but they are removed in the subsequent steps.

Once candidate sources have been found, a preliminary aperture photometry (PHOT task) with a radius defined by the user is performed, to give a first estimate of their magnitudes.

The next step is to pick well-suited stars for the calculus of the PSF (PICK task). This can be done in a completely automated way by the program, or with the aid of the user. For this thesis work, it has been chosen to allow the program to select stars automatically, and then to discard,

by visual inspection, the stars whose fit was not satisfactory. As for the fit function, a Moffat function was been generally preferred, while sometimes the program was allowed to choose automatically between a Moffat and a Penny function, on the basis of the standard deviation of the fit. Once a first PSF has been calculated (PSF task) for each frame, the next step is to perform a preliminary synthetic photometry. This task has been accomplished with the stand-alone program ALLSTAR (Stetson 1992), that performs PSF photometry simultaneously on all the stars present on the frame. With this approach, the influence on the single star by the neighboring stars is taken into account. Moreover, ALLSTAR re-determines the centroid of the stars, obtaining a better accuracy in the determination of this parameter, and re-calculates the sky background *after* that all stars have been provisionally removed by the fit, therefore achieving a better accuracy in the zero-point. Now, in the first determination of the PSF, reasonably isolated stars were chosen for the calculus. Nevertheless, faint neighboring stars can affect the fit, and hence a second PSF has been calculated on the frame where all but the PSF stars are subtracted (SUBSTAR task). In this way, a more accurate determination of the PSF is obtained. A subsequent run of ALLSTAR produces, for each frame, a star list with accurate positions and magnitudes.

3.7.3 Photometry - ALLFRAME

Once accurate positions and magnitudes have been obtained for each frame, the subsequent step is to cross-correlate the measurements to build light curves and color indexes. To this aim, geometrical transformations between star lists are computed to match star coordinates in the various frames. This task has been accomplished with the software DAOMASTER (Stetson 1993), that computes geometrical transformations between the input images, and provides a star list with positions and mean magnitudes relative to a reference frame. Mean magnitudes are obtained first calculating a mean offset between each frame and the reference frame, and then averaging the obtained measurements. It is also possible, in order to supply light curves, to have as output the single measurements, after they have been scaled to the reference image. However, with this procedure large discrepancies between measurements have been sometimes found. The reason is that, especially for critically or under-sampled images and with blended stars, it is difficult to split close sources with a sub-pixel accuracy. Therefore, it happens that a blob of light recognized as a single source in an image, is treated as, say, a double star in another image: in this case, magnitudes and colors are affected by large errors.

To overcome this problem, the best approach is to use the *same* master list from the beginning of the PSF photometry to the end, so that homogeneous identifications and magnitudes are obtained. This task is accomplished with the software ALLFRAME (Stetson 1994). Having obtained, for each frame, the individual PSF and ALLSTAR master list, geometrical transformations between frames and a single master star list, in the system of a reference image, are computed with DAOMASTER. ALLFRAME, for each frame, uses the master star list (re-transformed in the system of the current frame) and the individual PSF to subtract objects from the image. The residuals, both in brightness and in centroids coordinates, are then calculated: brightness is corrected immediately and the centroid corrections are saved. The process is iterated until convergence is reached. As with ALLSTAR, also with ALLFRAME local sky background is calculated after all the stars are temporally subtracted from the image. At the end of the process, ALFRAME produces, for each frame, a catalogue with position and magnitude of every source found in the image, and a star-subtracted image. The star-subtracted images can be stacked to reveal faint sources not included in the first master star list. Therefore, these sources can be added to the input catalogue and another run of ALLFRAME can be performed.

The accuracy of the results obtained with ALLFRAME not only depends on the quality of the single PSFs, but also on the accuracy of the computed geometrical transformations of the coordinates on the reference image, and on the accuracy of the positions of the stars in the input catalogue. This is a crucial point especially for faint objects, whose fit accuracy strongly depends on the position of the centroid. In these cases, the usual technique is to stack the single images to get a deep single image on which perform the photometry. Unfortunately, images collected with SOFI are often critically sampled or even under-sampled, and the technique to stack single images is not the better choice, because if the single centroids are not exactly aligned, the final image will have blurred stellar images, with an overall *decrease* of the S/N ratio. Moreover, since we are interested in obtaining light curves, we need the single measurements. The strategy devised for this thesis work, and developed for the first time, was to use one or more optical *V* or *I* –band images to build the master catalogue, and to use this catalogue as input catalogue with ALLFRAME. Figure 3.7 shows the comparison between the photometric accuracy that can be obtained by stacking images and with the described strategy. In the first case, the ALLSTAR photometry of the median (i.e. stacked) image is obtained; in the second case, the average of the ALLFRAME photometry of the single images is provided.

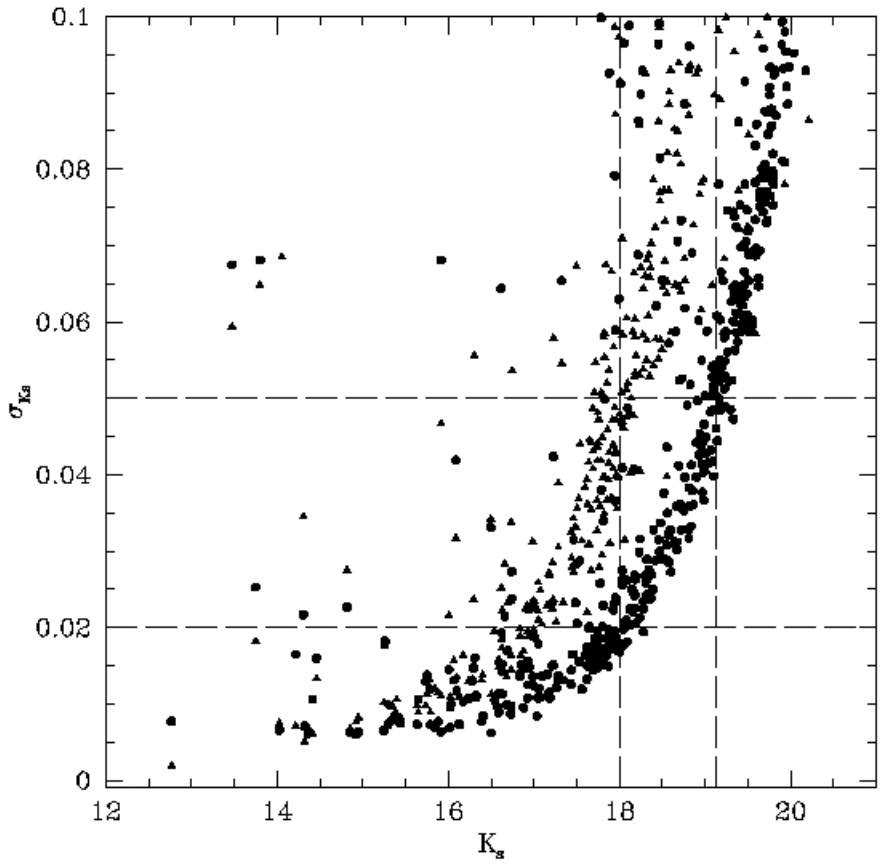

Figure 3.7. Comparison between ALLSTAR photometry on the stack of 171 Ks images (filled triangles), and the mean of the ALLFRAME photometry of the same images (filled circles). Dashed lines mark the range in magnitudes of the Reticulum RR Lyrae stars. The plot shows that, having fixed the magnitude, ALLFRAME photometry has a smaller intrinsic error; having fixed the photometric error, ALLFRAME photometry reaches fainter magnitudes.

3.7.4 The photometric calibration

The photometric calibration is probably the most critical step in the photometric reduction. The goal is to transform the measured instrumental magnitudes to a standard reference system, in order to compare the obtained results with those obtained by other observers. Usual calibration technique schedules to observe, during clear nights ("photometric nights") several standard stars, for which the apparent standard magnitude is known, with the same equipment used to collect scientific images. Then, the transformation from the instrumental system to the standard system is computed. The typical procedures account for:

- differences in integration time between the frames, both standard and scientific: to this aim, all the frames are normalized to a 1 second exposure, then $2.5 \log T_{\exp}$ is added, for

each image, to the measured magnitudes. With images taken with SOFI a warning is needed, because the actual exposure time is *not always* simply given by the product DIT × NDIT: till the end of 1999 the acquisition software of SOFI simply *summed* the sub-exposures, so that the integration time was indeed given by the above product. However, images acquired before are the result of an *average* of the single sub-exposures, so that the actual integration time is simply the single DIT. Anyway, the correct exposure time to be considered is listed in the header keyword EXPTIME;

- differences in the atmospheric extinction between images: to a first approximation, and when the field is not very low on the horizon (at least ~ 30° above the horizon), atmospheric extinction can be modeled as a linear function of the airmass $X = \mathrm{cosec}\, z$, where z is the zenithal distance. The slope of this relation is the extinction coefficient ε_λ at the λ wavelength. The extinction coefficient can be evaluated by observing the same standard star (or, more generally, the same object) at different airmasses: a linear regression of the observed magnitudes as a function of the airmass yields both the slope ε_λ and the zero-point m_{out}, i.e. the apparent instrumental magnitude that the object would have if it was observed outside the atmosphere. In the near-infrared bands, the usual technique to observe several standard stars at different airmasses to get the extinction coefficient is not very useful, because in those bands atmosphere is characterized by several features that not vary linearly with the airmass. Moreover, the IR window between 1 and 2.5 microns contains large features that are primarily due to the water vapor and to the carbon dioxide. The edges of the atmospheric window are thus highly variable and unfortunately the edges of *J* and K_s filters are designed by these atmospheric features. Therefore, with a highly variable water vapor column density, it is very difficult to achieve an absolute photometric calibration at the 1% level. In this case, the technique is to observe one or more standard stars as close as possible to the scientific target, and to observe them immediately before and after the target. With this approach, the dependence on the airmass is left out;
- differences in the standard photometric system and the instrumental system: the response in a given filter of the used equipment is not the same of the standard system. Since some of the photons collected with an instrumental filter (say, *B*) would fall, in the standard system, into another filter (say, *V*), the customary technique is to observe a standard star with two different filters, and to model the difference as a linear function of the color

index (in this case, *B-V*). The implicit assumption is that the differences between the standard and instrumental systems are not very large. In these cases more sophisticated transformations have to be adopted (involving more than one color index, and/or a higher order color terms). The near-infrared standard system adopted for this work is the so-called LCO (Las Campanas Observatory) system, defined by the standard list published by Persson et al. (1998). The *J, Ks* ESO filters used with SOFI have performance very close to the standard system. This means that the color terms are very small or even negligible: the transformations between the standard system and the SOFI system are the following, as listed in the SOFI user manual (Lidman et al., 2003)

$$J(P) - J(S) = -0.007(J-K)(P)$$
$$K_s(P) - K_s(S) = 0.023(J-K)(P)$$

where *P* stands for Persson and *S* stands for SOFI. The *K* band filter available with SOFI is not the standard *K* filter, but it is shaped in such way to avoid both the atmospheric absorption feature at 1.9 μm and the thermal background beyond 2.3 μm. This filter is called *K*-short (K_s). The difference between K_s and *K* is given by

$$K - K_s = -0.005(J-K)$$

and it has been considered negligible in the data reduction, since typical colors of globular cluster stars range from (*J-K*) = 0 to (*J-K*) = 1

The last step to perform in the photometric calibration, before applying the photometric zero-point calculated from the standard stars, is the so-called "aperture correction". PSF photometry is, as discussed above, an analytical approximation of the true stellar images: therefore, non-zero residuals are expected, because the program can over-estimate or under-estimate the measured flux. In principle, this is not a problem with relative (i.e. *internal*) photometry of a given image, since generally in the single image the flux ratios (i.e. the magnitude differences) are preserved. The problem raises when the instrumental magnitudes are transformed into a standard (i.e. *external*) system, since it is unlikely that the stellar profile is exactly the same in the target field and in the standard field, due to differences in airmass, seeing,

focus, tracking, etc… Moreover, the residuals can be position-dependent, so that even in the fortunate case that in the observed field are present standard stars, the *internal* photometry itself may need some correction. To deal with this problem, synthetic aperture photometry is performed on isolated, bright stars (typically the same stars used for the computation of the PSF) with a series of concentric apertures, and the difference between two consecutive apertures is plotted as a function of the aperture radius, building the so-called "growth-curve" (Rich, Da Costa, & Mould 1984). The adopted magnitude is then given by the asymptotic value of the growth curve. Aperture correction derived for the PSF stars, characterized by a high signal-to-noise (S/N) ratio, are then adopted for all the other stars on the frame.

Several approaches have been adopted in building the growth curve (for a discussion on this topic see Stetson 1990), using different ways to maximize the S/N ratios and different criteria to judge when a magnitude difference is reliable or it is an artifact due, for example, to a bad pixel. Moreover, it is worth noticing that this step in the photometric reduction is extremely time-consuming, because in principle a growth curve should be built, for each PSF star on each frame, choosing by eye the correct aperture differences.

For this work, the approach followed in the DAOGROW code (Stetson 1990) has been adopted. DAOGROW is completely automatic, since the code: a) evaluates the growth curve of a frame and estimate the aperture for a given star to be adopted, without any human guidance; b) can process all the data in time comparable with that requested from the other processing steps (such flat-fielding). To achieve these goals, DAOGROW takes a synoptic view of all the growth curves from a given set of images, so that it can have an expectation of a reasonable growth curve, and builds, for each frame, a best fit analytical growth curve. The basic assumption in this step is that a single-parameter family of growth curves is able, as a first approximation, to correct everything is wrong with a stellar profile. This is not strictly true, because de-focusing broadens stellar images in a different way than in a guiding error, and this effect is particularly evident at small radii, when only a fraction or the flux is considered. A purely empirical growth curve is not a viable approach, since at larger radii contribute of sky background (ant the noise associated) becomes more and more important. For these reasons, the *adopted* growth curve is not the analytical curve, since at small radii, where the S/N ratio is higher, the most accurate results are achieved with the *empirical* growth curve; on the other hand, at large radii, the empirical growth curve is too noisy, and the analytical curve works better. Therefore, DAOGROW adopts a sort of

average growth curve, weighted toward the empirical curve at small radii and toward the analytical curve at large radii.

In practice, for each dataset and for each filter a reference image was chosen, characterized by a good seeing and observed immediately after and before a standard star. Aperture corrections were therefore computed with DAOGROW on the same stars used to derive the PSF, having subtracted the neighbor stars with the command SUBSTAR available with DAOPHOT.

Once the aperture corrections have been estimated, the final step in photometric calibration is to apply the computed zero-points to individual scientific images, taking into account differences in airmass, color terms, etc. However, it is more convenient to set, for each filter, a reference image to calibrate and to scale the photometry of the other images. This can be done with DAOMASTER that, for each image, computes a robust mean difference with the reference image and applies it to the photometry of the considered image. At the end of the process, DAOMASTER writes out a file in which, for each star, are listed the photometric measurements scaled to the reference image. Finally, the computed photometric zero-point can be applied to this file.

However, it is worth noticing that the main problem that afflicts near-infrared calibrations is the measurements repeatability: when measuring a standard star on a set of images taken consecutively and reduced with the same procedure, the scatter in the measurements is larger than the intrinsic error of the photometry, thus suggesting the presence of intrinsic problems with infrared arrays.

Chapter 4
Observations and
Color-Magnitude diagrams

4.1 The LMC Cluster Reticulum

4.1.1 Introduction

The Large Magellanic Cloud Cluster Reticulum (GLC0435-59) is located at $\alpha = 04h35.4m$, $\delta = -58°56'$ (1950), 11° away from the main body of the LMC.

It is a very loose cluster, insomuch that Sersic (1974) described it as a "*dwarf… probably a member of the Local Group*". We selected this cluster because it hosts a sizable sample of RR Lyrae stars (32), is completely resolved, being its concentration $\log(r_t / r_c) = 0.5$ (where r_t is the tidal radius and r_c is the core radius; Demers & Kunkel 1976) and $\log(\rho_0) \approx 0\, M_\odot pc^{-3}$ (Peterson & Kunkel 1977), and has a low extinction (*E(B-V)*=0.03, Walker 1992). Moreover, its metallicity has been estimated using medium-resolution spectra ([Fe/H]=-1.71, Suntzeff et al. 1992). Figure 4.1 shows an image of the cluster, with the identification of RR Lyrae stars.

4.1.2 Observations and data reduction

Data were collected during two different runs between December 1999 and February 2002 in the *J* and *Ks* bands with SOFI@NTT. In the table 4.1 is reported the log of the observations. The seeing conditions were very good, with a FWHM ranging between 0.5 and 1.3 arcsec. The useful frames were 46 and 171 in the *J* and *Ks* bands, respectively, centered on the cluster. Exposure times range from 10 to 120s, while the total exposure time is 2,880 and 18,900 in the *J,*

Ks bands, respectively. Images were pre-reduced, following the approach described in chapter 3, with standard IRAF routines. The PSF for individual images was computed by selecting, on each frame, at least 20-25 stars. The PSFs were allowed to vary along each frame either linearly or quadratically. The quality of the fit was judged on the basis of the residuals on the subtracted image and on the smaller value of the χ. Since the cluster is completely resolved, and hence it does not suffers problems connected with crowding, the fitting radius was chosen as twice the FWHM. This choice has the advantage to improve the quality of the fit, and to get smaller χ values.

Night	Seeing (arcsec)	Number of *JK* phase points	Notes
1999 December 3	0.8	2	Photometric
1999 December 4	0.7	1	Photometric
1999 December 5	0.8	4	Photometric
1999 December 6	1.1	2	
2002 January 17	0.6-1.3	4	Photometric
2002 February 11	0.9	1	
2002 February 12	0.8	2	Photometric

Table 4.1. Journal of the observations of Reticulum.

Photometric calibrations were performed by choosing two reference images, in the *J* and in the *Ks*-band, and transforming the photometry of the other images on that of the two reference images. Calibrations were carried out on the night of 12 February 2002, and the transformations of the ESO *J* and *Ks* magnitudes to LCO system were calculated on the Persson 9109 (HST S055-D) standard star (Perrson et al. 1998), on which aperture photometry was performed with twelve apertures ranging from 3 to 20 pixels. The star was observed just before and after the two reference images, and a total of 10 measurements were obtained in both bands. Asymptotic *J* and *Ks* magnitudes were estimated with DAOGROW. Aperture corrections were calculated on the PSF stars of the reference images, having subtracted all the other stars with the DAOPHOT task SUBSTAR. The same apertures used for the standard star were therefore used to measure the PSF stars, and asymptotic magnitudes were computed with DAOGROW.

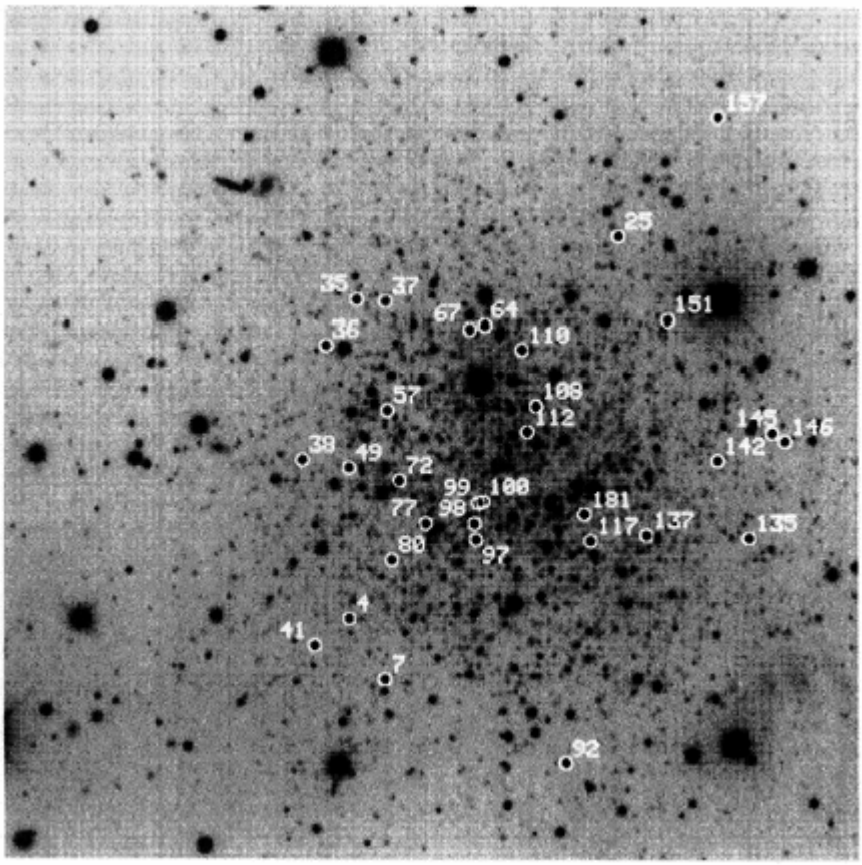

Figure 4.1 A400s V-band image of the LMC cluster Reticulum. Positions of RR Lyrae stars are shown. North is up and east to left. The picture is 7.5 arcmin square. Image from Walker (1992).

The calibration equations are the following:

$$J = j + 2.5(norm) - 2.118(ZP) - 0.040(AC)$$
$$K = k + 2.5(norm) - 2.717(ZP) - 0.042(AC)$$
$$\sigma_J = \sigma_K = 0.03 \text{ mag}$$

where *norm* is the normalization of the measured flux of the reference image to 1 second exposure, *ZP* is the measured zero-point on the standard star (normalized to 1 sec exposure), and *AC* is the aperture correction.

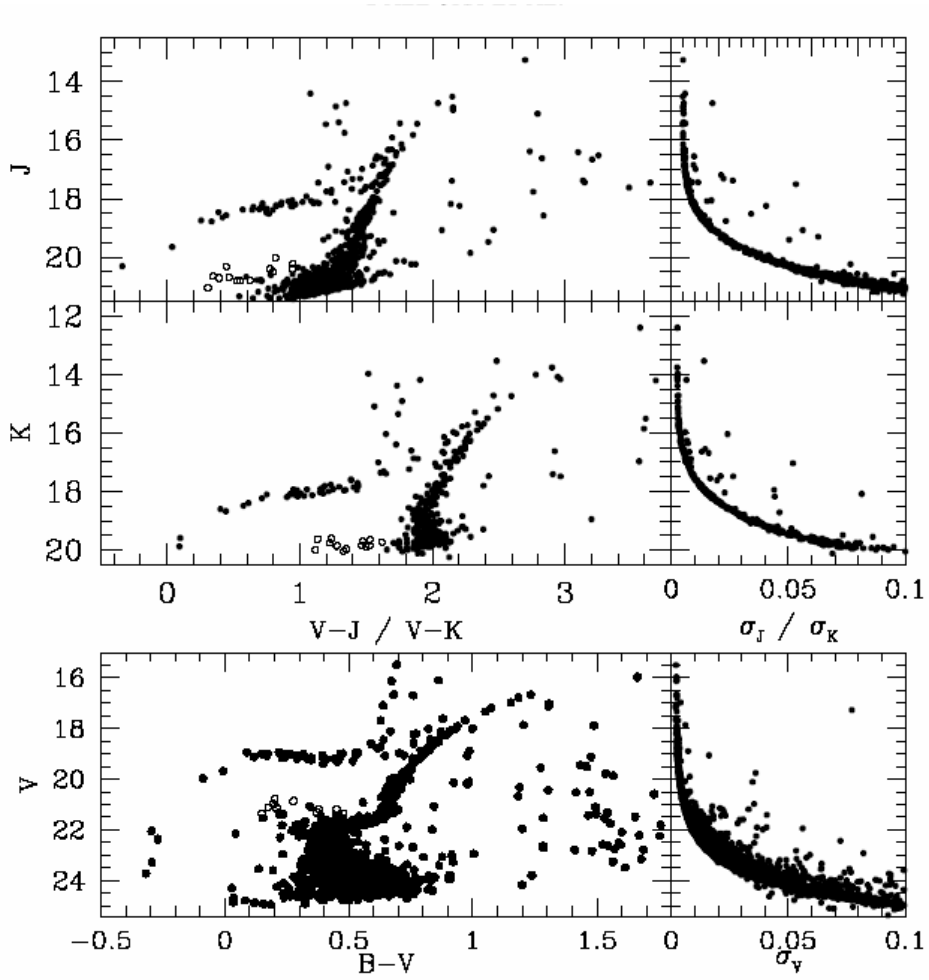

Figure 4.2. In the upper panels,* J-(V-J) *and* K-(V-K) *CMDs are shown, with the associated photometric (internal) errors. Horizontal Branches are clearly visible. Open circles depict candidate Blue Stragglers, confirmed in the* V-(B-V) *CMD (lower panel), showing that the Turn-Off region has been reached. These are the deepest CMDs ever obtained in the Near-Infrared bands. Plot from Dall'Ora et al. (2004b).

Optical *B, V* observations were secured with SUSI2@NTT during three different runs, in 1999, 2000, and 2001. In addiction, *V* frames from the ESO archive, acquired with SUSI1@NTT were added to the sample. Optical data were pre-reduced using standard procedures with IRAF, whereas photometry was performed with the DAOPHOT/ALLFRAME packages. An accurate photometric calibration was obtained by observing several standard stars from the catalogue of Landolt (1992), complemented with *B, V* new catalogue by Stetson (2000). On the whole, 33 *B, V* phase points were available. Optical data have been presented in Ripepi et al. (2004).

4.1.3 Color-Magnitude Diagram

Figure 4.2 shows *J, (V-J); K, (V-K);* and *V, (B-V),* color-magnitude diagrams (left panels) of Reticulum obtained with the present photometry, together with the internal accuracy of the measurements (right panels). The optical *(B-V),V* CMD is typical of an old simple stellar population, very similar to galactic globular clusters. Isochrone fitting, with the adopted metallicity and reddening (fig. 4.3), discloses an ancient population of about 11 Gigayears. This estimate is in good agreement with Walker (1992), who found an age similar, within 2 Gyr, to that of the galactic globular cluster M3 (which has an extimated age of 11 Gyr, Alves, Cook, & Wishnow 2003; Rey et al. 2001), and with the recent results of Mackey & Gilmore (2004) who, on the base of ACS Hubble telescope photometry, give a relative age, with respect to M3, younger of about 1.4 Gyr.

J, (V-J); K, (V-K) CMDs are the deepest ever obtained in the near-infrared bands. Open circles show candidate blue stragglers (that is stars slightly brighter and hotter than typical TO stars), suggesting that in the NIR CMD's the Turn-Offs have been reached. This suggestion is confirmed in the *(B-V), V* CMD, where open circles depict optical positions of the NIR candidates.

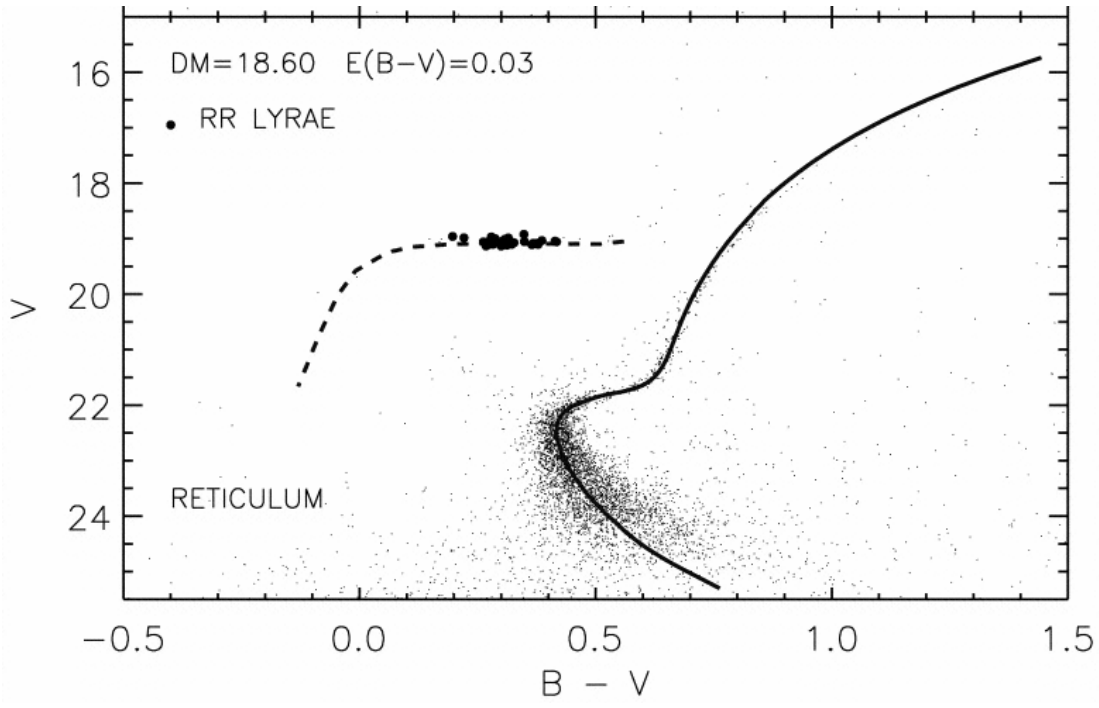

Figure 4.3. Optical photometry of Reticulum with a 11 Gyr isochrone superimposed. The isochrone was built by adopting Y = 0.23, Z = 0.004, and a mixing-length of α = 2. Plot adapted from Monelli et al. (2003).

4.2 The Galactic Globular Cluster M68

4.2.1 Introduction

M68 (NGC 4590) is a Galactic globular cluster located at $\alpha = 12h39m27.5s$ and $\delta = -26°44'30"$(J2000). Its Galactic coordinates are b = 299.63 and l = 36.05, while its Galactocentric distance is $R_{GC} = 10.1$ Kpc (Harris 1996). It is an extended cluster (tidal radius $r_t = 30.34$ arcmin) and moderately concentrated ($c = \log(r_t / r_c) = 1.64$, where r_c is the core radius).

Quoting A. Walker (1994): "*M68 is a metal-poor halo globular cluster that is rich in RR Lyraes and relatively easy to study owing to its proximity, relative openness, and low reddening. In many respects it is the southern analogue of M15*". M15 is the prototype of Oosterhoff II clusters (see chapter 2), and hence it is of paramount importance to compare the observational properties of its RR Lyrae stars with the predictions of both evolutionary and pulsation models. However, as outlined in chapter 2, the HB behavior depends not only on the chemical content, but also on environmental properties that are still not fully understood (second-parameter problem, blue tails etc.). For these reasons, it is very important to collect accurate information on a large set of globular clusters. M68 is an ideal target, since besides the features mentioned by Walker it is also characterized by the fact that the reddening is known with high accuracy ($E(B-V) = 0.07 \pm 0.01$, Walker 1994): this means that uncertainty on *V*-band magnitudes are poorly affected by the uncertainty on the reddening and hence a comparison between distances based on *V* and *K*-magnitude can supply tight constraints on the occurrence of deceptive systematic errors. Moreover, it is worth noticing that Walker' photometry is the most recently published on M68 and there are several deep multi-band unpublished archive data available. From the theoretical point of view, its HB is well-behaving, i.e. it has no peculiar features and hence it is an ideal candidate in comparing theoretical predictions with observations. Therefore, M68 can be a key object in refining evolutionary and pulsation theories.

In the following only near-infrared data will be presented, while optical *U, B, V, I* data have already been pre-reduced, and photometry is being performed.

4.2.2 Observations and data reduction

J, K_s data were collected with SOFI@NTT during two different observing runs between December 2000 and February 2002. Table 4.2 lists the observation logbook. On the whole, 66 *J* and 108 *Ks* for a total exposure time of 396s and 2580s, were respectively collected. We ended up with 12 phase points in both *J* and *Ks* bands. Data were pre-reduced following the procedures described in chapter 2, by means of IRAF routines.

Night	Seeing (arcsec)	Number of *JK* phase points	Notes
2000 December 17	0.8	1	
2001 February 4	0.9	1	
2001February 6	0.6	2	Photometric
2001 February 8	0.8	2	Photometric
2001 March 1	0.6	1	
2002 February 3	0.7	3	Photometric
2002 February 4	0.7	1	
2002 February 25	0.5	1	Photometric

Table 4.2. Journal of observations of M68. Phase points are per pointing.

Since the cluster is moderately extended, two sets of images were collected, one with the center of the cluster located on the left (north) edge of the detector, and the other with the center of the cluster on the right (south) edge of the detector. Hereafter, we will call “left” the former pointing, and “right” the latter. The two pointings overlap on a strip about 100 pixels wide along the *x*-axis. The stars in common allowed us to check the zero-point of the photometric calibration. Photometry was carried with DAOPHOT/ALLFRAME package, following the prescriptions discussed in chapter 3. As outlined in chapter 3, SOFI is affected by a poor image quality on the left side, because of a misalignment of the collimating lens. This implies that images are strongly elongated in a strip approximately 200 pixels wide along the *x*-axis, and the shape of the star images changes going from the upper edge to the bottom edge of such a strip (see figure 3.5). To account for this problem, images belonging to the left pointing were reduced with a cubic PSF, while the right pointing images were modeled with a quadratically or even with a linear PSF, according to the quality of the photometric residuals. On average, for each scientific frame, approximately 30-35 stars have been selected.

The master list to be used with ALLFRAME was built on three large field (7.5 × 15 arcmin) *V*-band frames, obtained with the Wide Field Imager available at the 2.2 meter ESO/MPI telescope. We selected two shallow (30s) *V*-band images and one deep (300s) *V*-band image, and the final catalogue includes both bright RGB stars and faint MS stars. Photometric reduction with ALLFRAME was performed on the whole set of images, regardless pointing and filter. Residual images were satisfactory, since no residual faint star was visible on the subtracted images.

Photometric calibration was performed on the images collected during the night of 25 February 2002, and zero-points were computed on the standard star P9150 (Persson et al. 1998), performing aperture photometry by means of fixed-radius aperture photometry. P9150 was observed just before and after a block of scientific images, allowing differential photometry. Moreover, differences in airmasses between scientific images and standard stars were small, i.e. $\Delta X = 0.07$. Since the mean absorption coefficients are smaller than 0.1 both in *J* and in the *Ks*-bands[2], the systematic error in the differential photometry is smaller than 0.01 mag in both bands.

For each pointing two reference images were chosen, in the *J* and in the *Ks*-band respectively, for the photometric calibration. Aperture corrections were calculated on the four reference images with a fixed radius for each image, equal to 10-15 half width half maximum. The two calibrated CMDs overlapped nicely. To further check the consistency of the calibration between the two pointings, instrumental *J* and *Ks* magnitudes of the stars in the overlapping region were compared, and a parabolic trend with the position along the *y-axis*, both in *J* and *Ks* bands, was found. It was therefore decided to transform instrumental magnitudes of the left pointing into the right pointing system. The correction was evaluated on the stars in the overlap region. No obvious trend was found along the *x*-axis and with the magnitude.

Summarizing, the adopted calibrations are:

a) right pointing

$J = j + 1.193(norm) - 2.050(ZP) - 0.006(AC)$

$K = k + 1.745(norm) - 2.698(ZP) - 0.011(AC)$

$\sigma_J = 0.04$ mag

$\sigma_K = 0.02$ mag

[2] http://www.ls.eso.org/lasilla/sciops/ntt/sofi/setup/Zero_Point.html

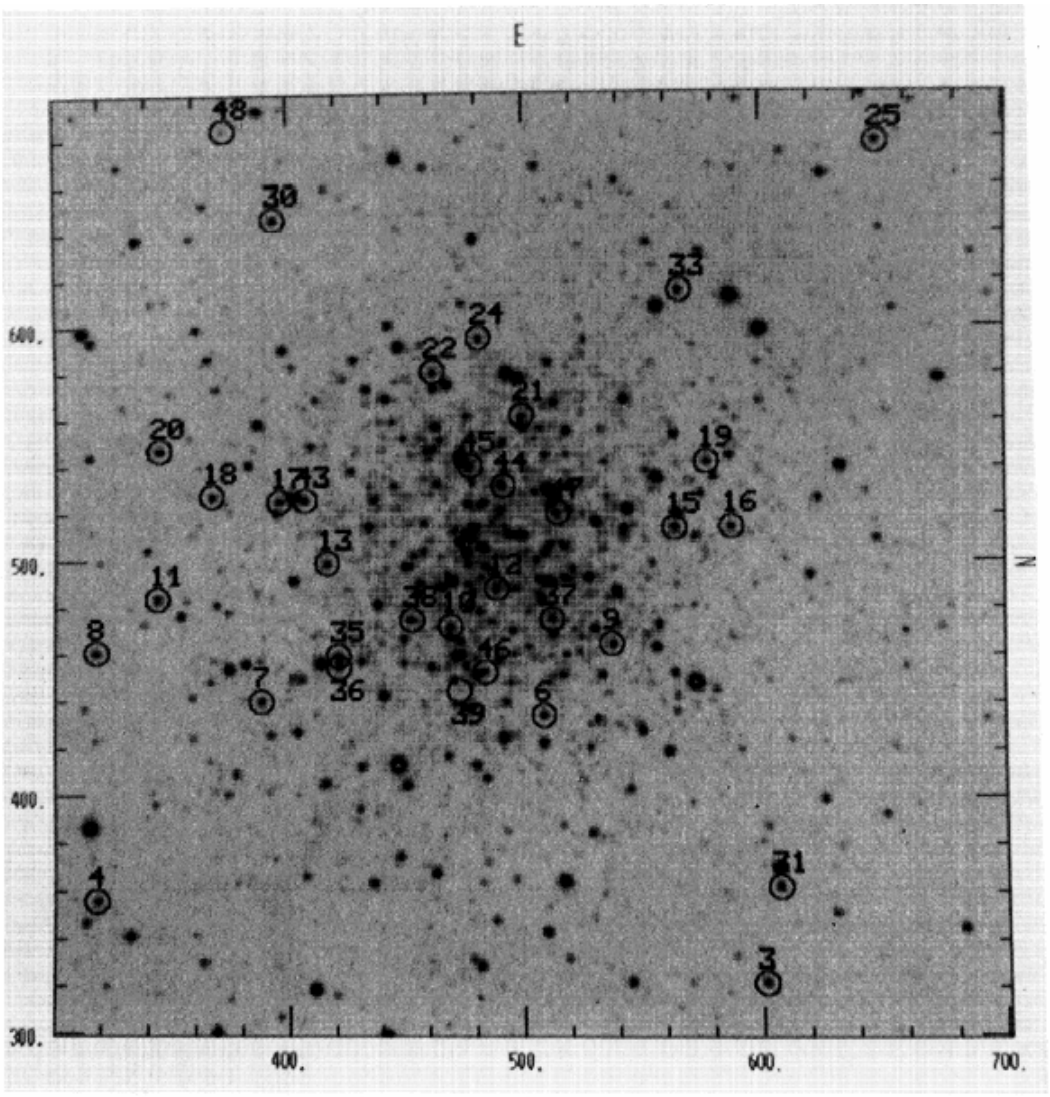

Figure 4.4.* V-*band image of M68. Identifications of RR Lyrae stars are shown. East is up and North is left. Field size is (5.28 ×5.28) arcmin. Image from Walker (1994).

b) left pointing

$$J = j + 1.193 - 2.050 - 0.006 + (-0.149 + 6.3396^{-4} \times (y + 0.6) - 5.4751 \times 10^{-7} \times (y + 0.6)^2)$$

$$K = k + 1.747 - 2.698 - 0.011 + (-0.149 + 5.218 \times 10^{-4} \times (y + 29.6) - 4.3060 \times 10^{-7} \times (y + 29.6)^2)$$

$$\sigma_J = 0.04 \text{ mag}$$

$$\sigma_K = 0.03 \text{ mag}$$

where *norm* is the normalization of the recorded flux to 1 second exposure, *ZP* is the measured zero-point on the standard stars (normalized to 1 sec exposure), and *AC* is the aperture correction.

Errors were computed by simply adding in quadrature the errors associated to each component. The main source of error was the dispersion in the photometry of the standard stars ($\sigma = 0.02 - 0.04$ mag on average).

An independent check on the quality of the calibration, in the *Ks* band, was performed by comparing our calibrated *Ks* magnitudes with the *Ks* photometry of M68 available from the Two Micron All-Sky Survey (2MASS) database (http://www.ipac.caltech.edu/2mass). Following the transformations shown in Carpenter (2001), the expected difference between our LCO *Ks* magnitudes and the 2MASS *Ks* magnitudes is $K_s^{LCO} - K_s^{2MASS} = 0.010 \pm 0.004$ mag. By selecting on the reference image bright, isolated stars (in order to minimize possible blendings due to the large pixel scale of the 2MASS images), we found $K_s^{LCO} - K_s^{2MASS} = 0.008 \pm 0.033$ mag, in excellent agreement with the estimated difference.

In passing, we note that this calibration is improvable, since for the present work fixed-radius aperture corrections were computed only for the four reference images. However, as discussed in chapter 3, better results should be obtainable if growth curves are computed by running DAOGROW on *all* the scientific images.

4.2.3 Color-Magnitude Diagram

Figure 4.5 shows the calibrated *K*-(*J*-*K*) color-magnitude diagram of M68 (left panel, ALLFRAME mean magnitudes) and the ALLFRAME intrinsic photometric error (left panel). The diagram shows the photometry of approximately 9,000 stars, with an excellent dynamic range (more than 9 magnitudes in *Ks*). RR Lyrae stars are approximately at $K \sim 14.5$, and are depicted with empty triangles. The *bump* of Red Giant Branch, at $(J-K) \approx 0.6, K \approx 12.8$, is visible and the limiting magnitude is well below the Turn-Off region. Several candidate Blue-Stragglers are visible at $(J-K) \approx 0.2 - 03, K \approx 16 - 17$. Further conclusions from the CMD will be obtained when the photometric reductions in the optical bands will be complete.

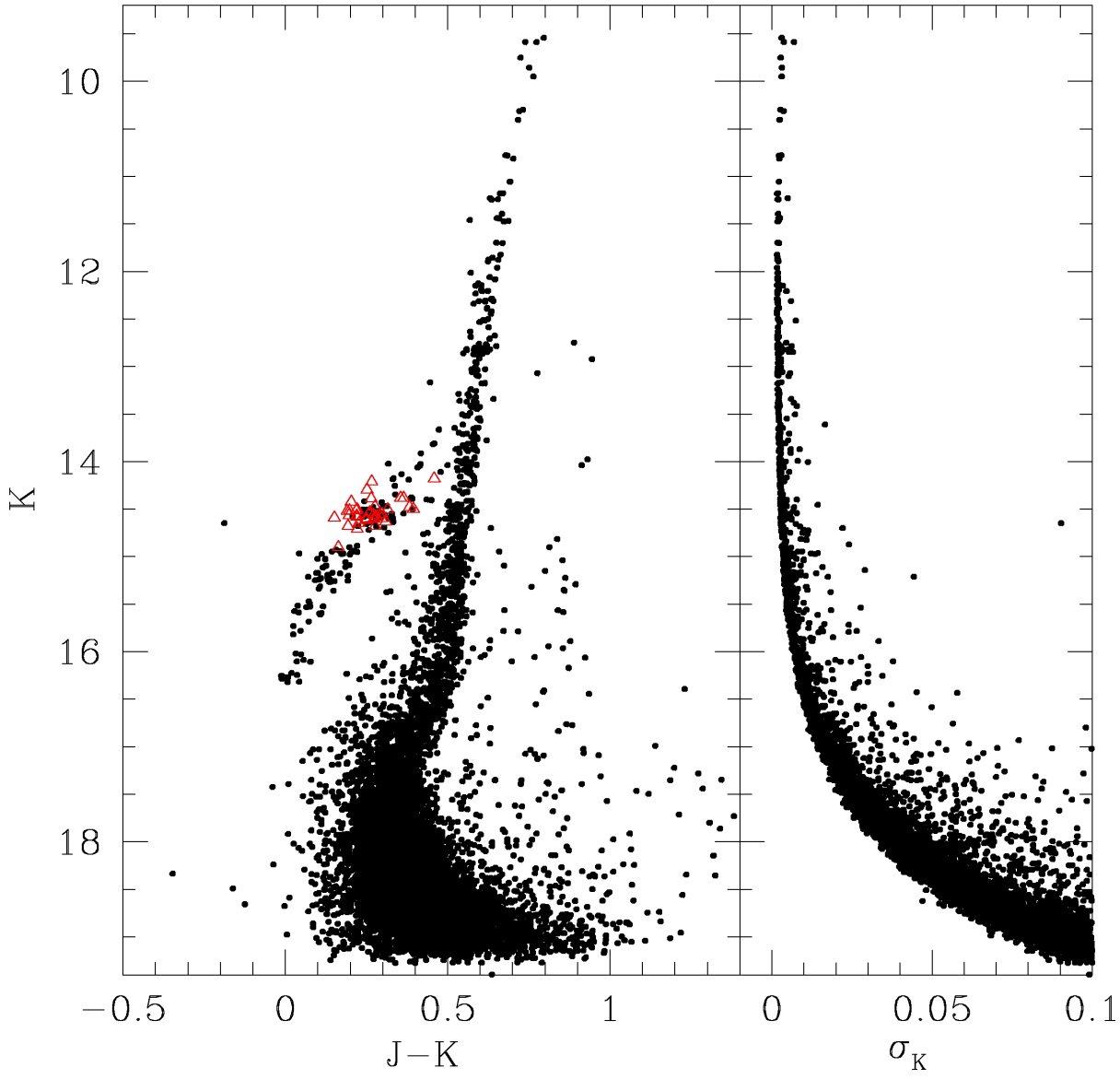

Figure* 4.5. K-(J-K) *color-magnitude diagram for the GGC M68 (right panel). Red empty triangles mark the RR Lyrae stars (see chapter 5) .The right panel shows the internal photometric error, estimated by ALLFRAME.

4.3 The Galactic Globular Cluster NGC 3201

4.3.1 Introduction

NGC3201 is an Oosterhoff I Galactic globular cluster located at $\alpha = 10\text{h}17\text{ m}36.8\text{s}, \delta = -46°24'40''$, with Galactic coordinates $l = 277.228, b = 8.641$. It is therefore an object close to the Galactic plane, characterized by a strong field contamination and by high reddening, with a mean value of $E(B-V) \approx 0.25-030$. Moreover, it is affected by a strong differential reddening, with current estimates that range between $0.24 \le E(B-V) \le 0.35$ (Piersimoni, Bono, & Ripepi 2002), and between $0.18 \le E(B-V) \le 0.37$ (Layden & Sarajedini 2003). NGC 3201 is an interesting object for many aspects, since it hosts a large number of RR Lyrae stars ($N_{RR} = 77$, Clement et al. 2001), and it is relatively close ($DM_0 \approx 13.35$), allowing detailed spectroscopic surveys. It is not particularly crowded, since its central concentration is $\log \rho_0 = 2.69 L_{\odot} pc^{-3}$ (Trager, Djorgovski, & King 1993), thus giving the possibility of an accurate photometry even in the innermost regions. Its mean metallicity is of the order of $[Fe/H] \sim -1.5$ in the Zinn & West scale (Rutledge, Hesser & Stetson 1997; Piersimoni, Bono, & Ripepi 2002; Kraft & Ivans 2003), although in the past a metallicity spread was claimed (Gonzalez & Wallerstein 1998). However, such a spread was not supported by Covey et al. (2003), on the basis of high resolution spectra of six red giants. A further interesting feature of NGC 3201 is that it presents a retrograde orbit (van den Bergh 1993). According to the classification provided by Zinn (1993), GGCs can be divided the halo two groups: a) the "old halo" group obeys a tight HB type versus [Fe/H] relationship, b) while the "younger halo" group deviates from this relationship by a significant amount (second parameter phenomenon). Moreover, Zinn (1993) and Da Costa & Armandroff (1995) argued that the old and the younger halo groups have different kinematic properties in that the old halo group has a prograde mean rotation velocity with smaller velocity dispersion while the younger halo group has a retrograde mean rotation velocity about the Galactic center with larger velocity dispersion. They suggested that the old halo group formed during the collapse that led ultimately to the formation of the Galactic disk and the younger halo group were accreted later in time (see also Lee, Carney, & Habgood 2005). Since NGC 3201 has a retrograde orbit, it is interesting to give an accurate estimate of its age in order to check the Zinn's hypothesis. The ages of the globular clusters are estimated on the basis of the absolute luminosity of the Main Sequence Turn-Off, thus

transforming the apparent luminosity taking into account the reddening and the distance modulus (and knowing the cluster' metallicity). Unfortunately, NGC 3201 is affected by a strong differential reddening, and therefore its age estimate is affected by a large uncertainty. To solve this problem, Piersimoni, Bono, & Ripepi (2002) evaluated individual reddening for the RR Lyrae stars by comparing observed (*B*-*V*) and (*V*-*I*) colors with the intrinsic (un-reddened) colors predicted by period-amplitude-color relations. A surface was then fitted to the individual reddenings, obtaining a map of the reddening to use with the other stars. By adopting a true distance modulus of $(m-M)_0 = 13.32$, they give an estimate of the age of NGC3201 of the order of 13 Gyr. Layden & Sarajedini (2003), by adopting a similar approach and a distance modulus of $(m-M)_0 = 13.44$, estimated an age of 13 ± 2 Gyr, in excellent agreement with the Piersimoni and collaborators' result. Therefore, these results do not seem to support the hypothesis that NGC 3201 is an accreted cluster. Unfortunately, the uncertainty on the distance of NGC 3201, based on the *V*-band magnitude of the RR Lyrae stars, does not allow us to give firm conclusions. However, more striking conclusions on the distance and the age of NGC 3201 can be obtained with the *PLK* relation, since in the *K*-band the absorption is only the 10% than in the *V*-band and since the relation has a small intrinsic scatter.

Finally, it is worth mentioning that NGC 3201 not only hosts RR Lyrae stars, but have also been identified other kind of variable stars, such as RGB variable stars, δ Scuti stars and eclipsing binaries.

4.3.2 Observations and data reduction

J, K_s data were collected with SOFI@NTT during 6 different nights between November 2000 and March 2001. Since NGC 3201 is a very extended cluster (tidal radius $r_t = 28.45$ arcmin, Harris 1996), the observations were split to two pointings, one centered on the north-east corner (hereafter, left pointing or SX) and the other one centered on the south-east corner (right pointing or DX). Therefore, only one portion of the eastern side of the cluster was covered by observations, and only covering the 25% of the tidal radius. The overlap between the two pointings was, on average, only of 40-50 pixels, in order to maximize the covered area. On the whole, 48 *J* and 72 *Ks*-band images were collected. Table 6.1 shows the log of the observations. Images were pre-reduced following the steps discussed in chapter 3, and

photometry was performed by means of the DAOPHOT/ALLFRAME package. For each image, about 30-35 stars were selected to compute the PSF.

Night	Seeing (arcsec)	Number of *JK* phase points	Notes
2000 November 6	0.7-1.2	1	Photometric
2000 December 17	0.5	1	
2001 February 4	0.6	1	
2001 February 6	0.4-0.6	2	Photometric
2001 February 8	0.4	2	Photometric
2001 March 1	0.6	2	Photometric

Table 4.3. Journal of the observations of NGC 3201. Phase points are per pointing.

As discussed in chapter 3, SOFI is affected on the left side by strong image degradation, due to a misalignment of the collimating lens and a cubic PSF was chosen for the left pointing, while a quadratic PSF was preferred for the right pointing. The program was allowed to choose between a Moffat and a Penny function, on the basis of the standard deviation of the fit. As for M68, the input catalogue to use with ALLFRAME was built on three large field (7.5 × 15 arcmin) *V*-band images collected with the Wide Field Imager available at the 2.2 meter ESO/MPI telescope. The input catalogue consists approximately of 16,000 objects, whereas for each image on average 5,500 stars were fitted. Data were calibrated on the night of 6 February, on two reference images (one per filter) for each pointing, in *J* and in the *Ks*-band. Aperture photometry was performed on the standard stars P9144 and P9150 (Persson et al. 1998) with increasing radii from 4 to 18 pixels. Asymptotic magnitudes for the two standard stars were then calculated with DAOGROW. P9144 was observed just before NGC3201, while P9150 soon after, therefore allowing differential photometry. The difference in airmass between the two standards, and between the two standards and the scientific reference images was less than 0.05. Following the extinction coefficients listed in the SOFI web site[3], the systematic effect introduced is less than 0.01 mag. Aperture corrections were calculated with DAOGROW for the four reference images on the PSF stars, having subtracted from the images all the other stars. Unlike the case of M68,

[3] http://www.ls.eso.org/lasilla/sciops/ntt/sofi/setup/Zero_Point.html

no evidence for position-dependent residuals between the two pointings was found. The computed photometric zero points are:

a) right pointing

$J = j + 1.193(norm) - 2.098(ZP) + 0.060(AC)$

$K = k + 1.193(norm) - 2.702(ZP) + 0.079(AC)$

$\sigma_J = 0.02$ mag

$\sigma_K = 0.02$ mag

b) left pointing

$J = j + 1.193(norm) - 2.098(ZP) - 0.064(AC)$

$K = k + 1.193(norm) - 2.702(ZP) - 0.077(AC)$

$\sigma_J = 0.02$ mag

$\sigma_K = 0.02$ mag

where *norm* is the normalization of the recorded flux to 1 second exposure, *ZP* is the measured zero-point on the standard stars, and *AC* is the aperture correction. Errors were computed by simply adding in quadrature the errors associated to each component. The main source of error was the dispersion in the photometry of the standard stars ($\sigma = 0.02$ mag on average). The overlap of the two calibrated CMDs was satisfactory.

As in the case of M68, an independent test on the calibration was performed by comparing our calibrated *Ks* magnitudes with those available in the 2MASS database. The difference found was $K_s^{LCO} - K_s^{2MASS} = 0.010 \pm 0.015$ mag, in excellent agreement with the expected shift (Carpenter 2001).

4.3.3 Color-Magnitude diagram

Figure 4.6 shows the *K*-(*J*-*K*) Color-Magnitude diagram of NGC3201 (left panel), with the associated intrinsic photometric error in the *K*-band (right panel). ALLFRAME mean magnitudes of about 12,000 stars are showed. Red empty triangles mark the positions of the RR Lyrae stars. The broadening of the photometric error (right panel) for stars brighter than $K \sim 9$ is due to non-linearity effects. The limiting magnitude is well below the Turn-Off region. RR Lyrae stars are along the HB, approximately at $K \sim 13$. The overdensity at $(J-K) \approx 0.7$, $K \approx 11.5$ could

be the *bump* of Red Giant Branch. Several candidate Blue-Stragglers are visible at $(J-K) \approx 0.4-05$, $K \approx 14-15$. Faint stars on the red side of the Main Sequence are probably field stars. A cross-check with optical photometry in the *B* and *V*-bands will set these points.

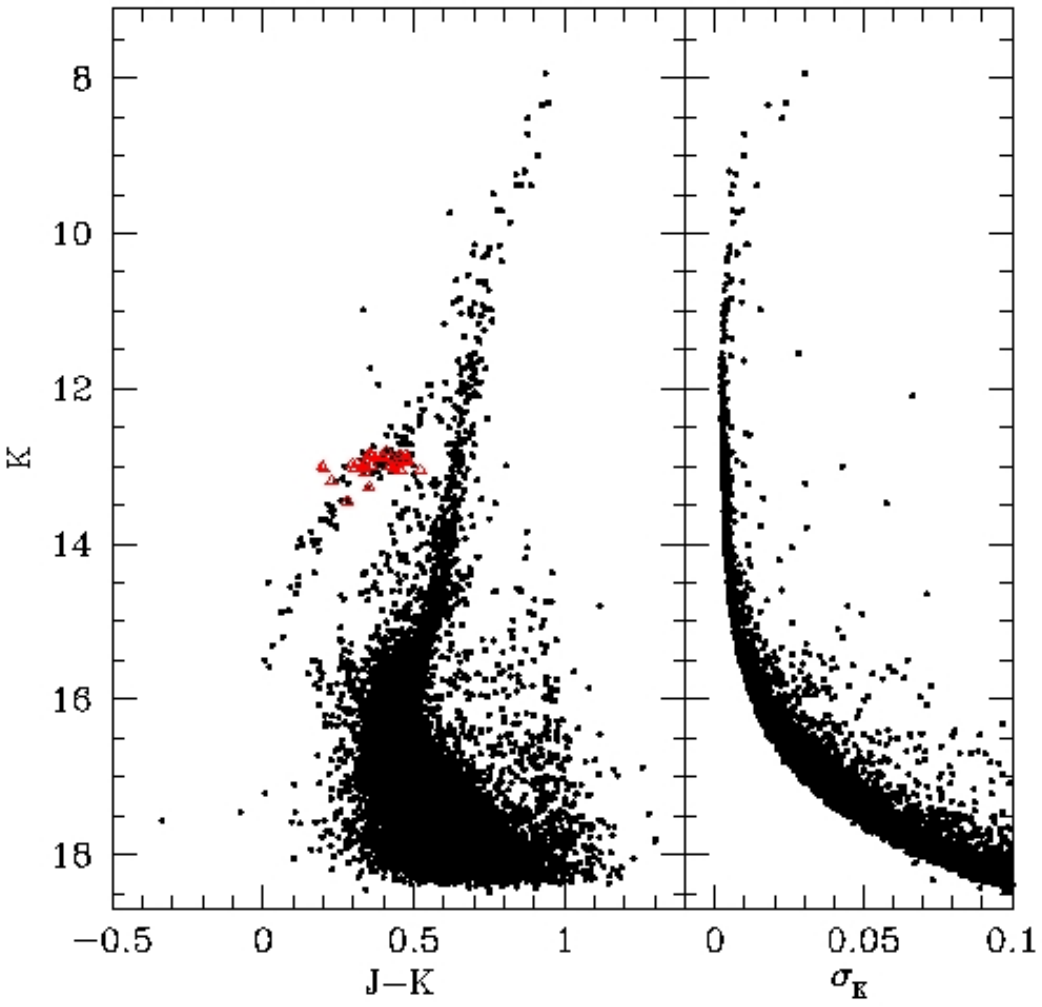

Figure 4.6. **K-(J-K)** ***color magnitude diagram for the GGC NGC 3201(left panel). ALLFRAME mean magnitudes are used for about 12,000 stars. Empty triangles show the position of RR Lyrae stars. In the right panel the ALLFRAME (internal) photometric error is plotted.***

Chapter 5
Discussion of the results: distances estimates

5.1 The distance to Reticulum

The field covered by the observations allowed us to measure 30 out of the 32 RR Lyrae stars catalogued by Walker (1992). Table 5.1 lists the properties of RR Lyrae stars in the sample. Periods and epochs have been estimated on the basis of the optical data, that covers a time interval of about five years, and then they produce very accurate ephemeredes. Optical mean magnitudes have been evaluated by fitting individual measurements with cubic splines.

Estimated periods and epochs have therefore been used to phase *Ks*-band light curves. On the single measurement the error was of the order of the 0.1 mag, therefore light curves are very noisy (fig. 5.1, bottom panel). For this reason, light curves were fitted not with splines, but with well-suited templates, calculated by Jones, Carney, & Fulbright (1996). They have determined five different templates depending on the type of variability (RRab or RRc) and on the *B*-band amplitude of the variable, and they described each of these templates with a Fourier series. For each star the corresponding Fourier template was computed, on the basis of the ephemeredes and of the *B*-band amplitudes (Ripepi et al. 2004; Ripepi, private communication). The candidate RRd stars have been treated as RRc variables because of their small amplitudes and relatively short periods. For each observed phase point it is possible to compute the best estimate of the mean magnitude over the phase φ of the variable by subtracting the template magnitude from the observed magnitude, i.e. $\langle K \rangle = K_{obs}(\varphi) - K_{templ}(\varphi)$. Weighted intensity-averaged magnitude was computed over all the observed phase points for each variable star. The resulting mean magnitudes and their associated intrinsic errors are listed in table 5.1. Figure 5.2 shows the mean <*K*> magnitude as a function of log P.

Periods of first-overtones variables (open circles) have been fundamentalized, i.e. a constant it has added according to $\log P_F = \log P_{FO} + 0.127$ (Di Criscienzo, Marconi, & Caputo 2004). Linear regression gives

$$< K >= -2.16(\pm 0.09)\log P + 17.352(\pm 0.025)$$

with a standard deviation of 0.03 mag, in good agreement with the value predicted by B01 ($\alpha = -2.071$) and by B03 ($\alpha = -2.101$).

To derive an estimate of the distance to Reticulum, observed mean magnitudes have then been compared with absolute magnitudes predicted by the pulsation theory. The adopted relation is the semi-empirical calibrations from B03, where the theoretical relationship has been calibrated on empirical data from field RR Lyrae stars, for which accurate *V* and *K* magnitudes, reddenings and metallicities are available in the literature. The adopted relation is

$$M_K = -0.770(\pm 0.044) - 2.101\log P + 0.231(\pm 0.012)[\mathrm{Fe/H}]$$

It is worth noting that all the theoretical relations concerning the *PLK* have been derived in the *K*-band defined by Bessel & Brett (1988). To properly compare the observations, calibrated in the LCO system, with the theoretical relations, the latter have been transformed into the LCO system. Following the transformations provided by Carpenter (2001), theoretical *K* magnitudes were therefore transformed with the relation

$$K^{LCO} = K^{B\&B} - 0.034$$

ID	*logP* (days)	Epoch (HJD)	<*K*> (mag)	σ_K (mag)	Type
V4	-0.45195	2448206.006	18.058	0.017	c
V7	-0.20853	2448206.070	17.824	0.015	ab
V25	-0.29657	2448206.125	18.020	0.018	ab
V35	-0.27164	2448206.285	17.963	0.015	ab
V36	-0.48161	2448206.220	18.170	0.018	c
V37	-0.29401	2448206.010	18.003	0.016	ab
V38	-0.29043	2448206.968	18.001	0.020	ab
V41	-0.45157	2448206.150	18.055	0.017	d
V49	-0.28158	2448206.708	17.958	0.017	ab
V57	-0.28938	2448206.055	17.933	0.017	ab
V64	-0.28918	2448206.250	17.983	0.018	ab
V67	-0.18245	2448206.515	17.746	0.014	ab
V72	-0.45073	2448206.070	18.060	0.018	d
V77	-0.45276	2448206.258	18.061	0.019	c
V80	-0.24272	2448206.295	17.888	0.015	ab
V97	-0.22529	2448206.245	17.827	0.016	ab
V98	-0.44894	2448206.000	18.077	0.018	d
V99	-0.21497	2448206.535	17.785	0.014	ab
V100	-0.23162	2448206.360	17.835	0.016	ab
V108	-0.32917	2448206.100	18.062	0.016	ab
V110	-0.45906	2448206.100	18.031	0.017	d
V112	-0.25124	2448206.250	17.863	0.019	ab
V117	-0.29205	2448206.245	17.930	0.017	ab
V135	-0.19047	2448206.510	17.783	0.014	ab
V137	-0.26363	2448206.455	17.954	0.016	ab
V142	-0.24504	2448206.200	17.910	0.018	ab
V145	-0.21988	2448206.338	17.786	0.018	ab
V146	-0.31439	2448206.044	18.035	0.019	ab
V151	-0.49493	2448206.134	18.108	0.019	c
V181	-0.52832	2448206.122	18.209	0.018	c

Table 5.1 .Photometric properties of the RR Lyrae stars in Reticulum. Intensity-averaged mean* K *magnitudes are based on the fitting method by Jones et al (1996). Epochs are in Heliocentric Julian Days. In column 5 fundamental and first-overtone RR Lyrae stars are labelled with ab and c, respectively, while candidate mixed-mode RR Lyrae stars are labelled with d. Table from Dall'Ora et al. (2004b).

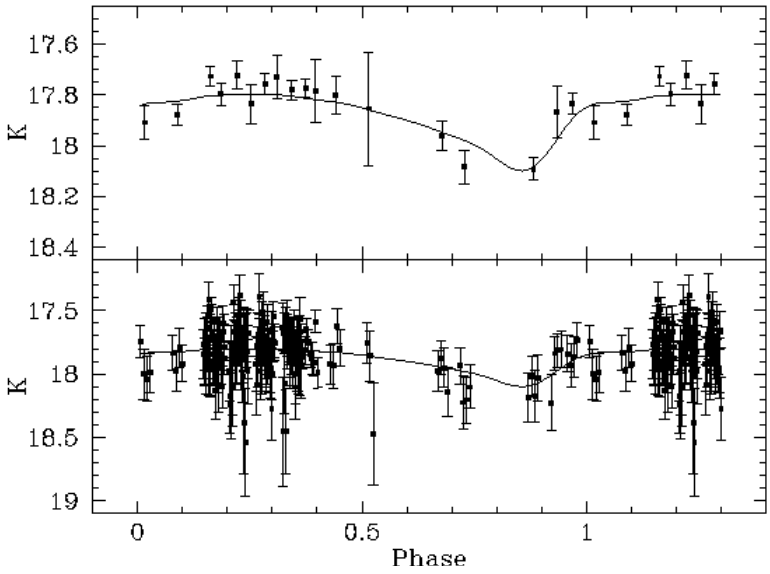

Figure 5.1.* K-*band light curve of the Reticulum variable V80. In the lower panel single measurements are plotted, with superimposed the fit with the Jones et al. (1996) template (solid line). In the upper panel measurements were averaged by phase bin.

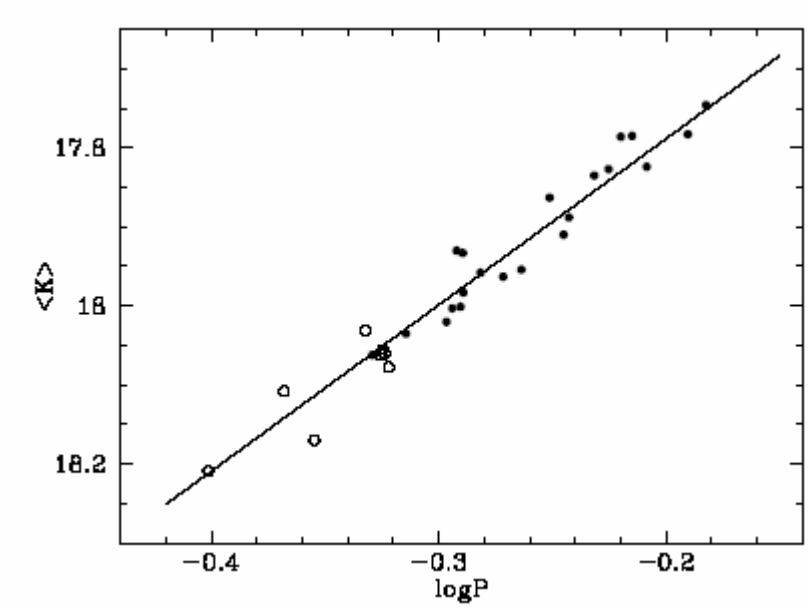

Figure 5.2. Intensity-weighted mean magnitudes <K> vs. logP_F. Filled circles are fundamental pulsators and open circles are (fundamentalized) first-overtones. The straight line represent the theoretical relation from Bono et al. (2003), scaled to the estimated distance modulus. Plot from Dall'Ora et al. (2004b).

By adopting [Fe/H] = -1.71 (Suntzeff et al. 1992) and by using this value in the previous equation, distance modulus for each star is found. The weighted mean of the obtained value is 18.534 ± 0.005. The adopted reddening to Reticulum has been determined by Walker (1992), who found a value of *E(B-V)* = 0.02 mag. Combining this value with the absorption given by Cardelli, Clayton, & Mathis (1989), $A_K = 0.11 \times A_V = 0.11 \times 3.1 \times E(B-V)$, a tiny value is found, i.e. $A_K = 0.011 \text{mag}$. The de-reddened estimated distance modulus to Reticulum is therefore

$$DM_0 = 18.523 \pm 0.005$$

where only the intrinsic random error is listed.

As already discussed (see sec. 2.10.2), when *V* and *K* magnitudes are available it is possible to give an estimate of the luminosity of each pulsator with a Period-Color-Luminosity relation, by using the equation

$$\left(M_V - M_K\right)^F = 4.014 + 1.986 \log P - 0.134 \log Z - 1.662 \log L + 1.656 \log M / M_r$$

The estimated luminosity can be therefore inserted in the *PLK* equation

$$M_K^F = 0.511 - 2.102 \log P + 0.095 \log Z - 0.734 \log L - 1.753 \log M / M_r$$

and, by adopting a reference mass of $M_r = 0.75 M_\odot$, a pulsator mass of $M = 0.80 M_\odot$ and having fundamentalized the first-overtone pulsators, the estimated true distance is $DM_0 = 18.53 \pm 0.03$, where the mean value is the simple mean and the error is the dispersion around the mean. *V*-band magnitudes were supplied by V. Ripepi (private communication). From the above equation, the estimated luminosity level is of the order of $\log L \approx 1.7$, in excellent agreement with the expected value for the estimated metallicity.

It is interesting to compare the obtained value with those available in the literature, found with different methods, in order to highlight possible systematic effects in the adopted procedure. Demers & Kunkel (1976), on the basis of photographic magnitudes calibrated on local standards with photoelectric measurements, found a *V* mean magnitude for Horizontal Branch stars

of $< V_{HB} >= 19.17 \pm 0.06$. By adopting an absolute magnitude of $< M_V >= 0.6$ and an excess of colour of $E(B\text{-V})=0.02$, they found a de-reddened distance modulus of 18.48.

Gratton & Ortolani (1987) estimated on the basis of CCD photometry a de-reddened (reddening as in Demers & Kunkel) mean magnitude for RR Lyrae stars of $< V_0 >= 19.01 \pm 0.06$. With an adopted absolute magnitude of $< M_V >= 0.52$, they estimated a true distance modulus of 18.49 ± 0.1

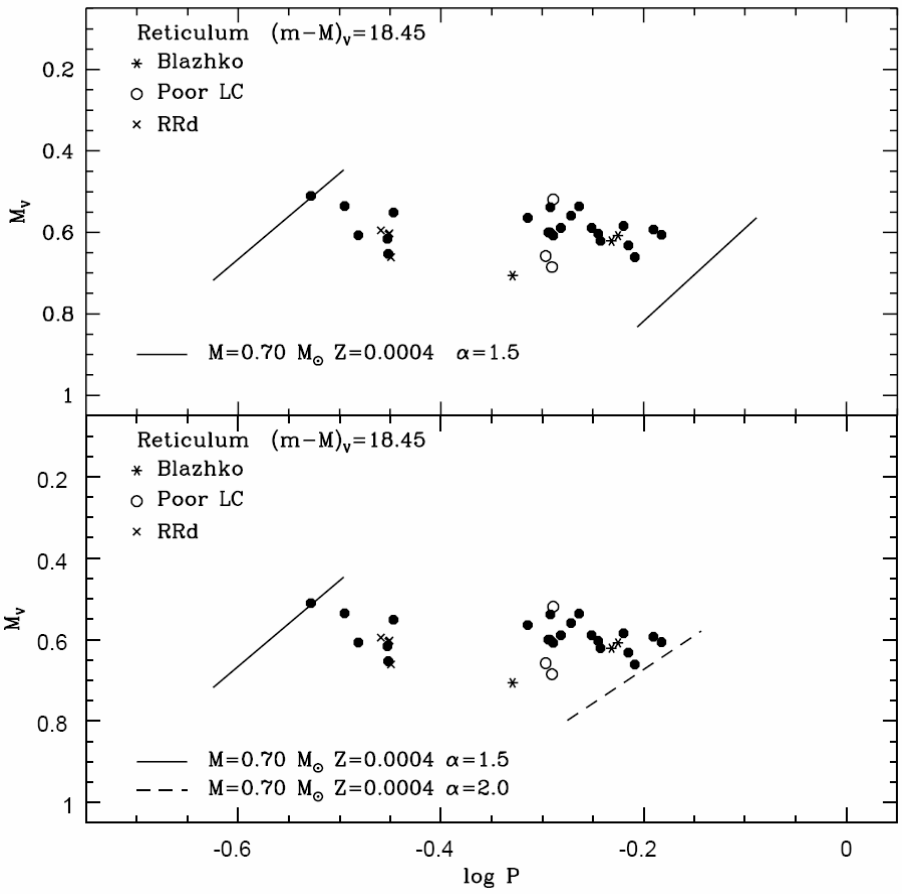

Figure 5.3. Distribution of observed Reticulum RR Lyrae stars in the* logP-M_V *plane. Predicted edges of the Instability Strip for the assumed mass, metal abundance and convection are shown. The match between the theoretical prediction of the First Overtone Blue Edge and the observed distribution gives an estimate of the distance modulus .De-reddened distance modulus is 18.39 mag. Plot from Ripepi et al. (2004).

Walker (1992) obtained a de-reddened ($E(B\text{-V})=0.02$) mean V magnitude for RR Lyrae stars in Reticulum of $< V_0 >= 18.98$. Adopting an absolute magnitude of $< M_V >= 0.6$, he found a de-reddened distance modulus of 18.38. The comparison between photometry in Walker with the

two quoted investigations shows a large scatter with *V* magnitudes of Demers & Kunkel, and a slight discrepancy with Gratton & Ortolani, being Walker's *V* magnitudes brighter of ≈ 0.04 mag.

Ripepi et al. (2004), by comparing the observed period distribution of RRc variables with the predicted blue edge of the instability strip (FOBE method, Caputo 1997; Caputo et al. 2000; Marconi et al. 2003; see figure 5.3) and by adopting $E(B\text{-V})=0.02$, supply a true distance modulus

$$(m-M)_0 = 18.39 \pm 0.12 .$$

in good agreement with the value found by Walker (1992).

Table 5.2 summarizes the distance determinations to this cluster. To properly compare results, column 2 shows distance moduli obtained by adopting the same parameters (reddening and metallicity) used for the *PLK* method. It is worth noticing that, if the relation

$$M_K = 0.139 - 2.071(\log P + 0.30) + 0.167 \log Z$$

(Bono et al. 2001) is adopted, then the distance to Reticulum is 18.46 ± 0.03 mag. Therefore, it seems that the discrepancy resides in the coefficient of the metallicity term.

Method	$(m-M)_0$	**Reference**
PLK (B03) semi-empirical	18.52 ± 0.03	Dall'Ora et al. (2004b)
PLK (B03) theoretical	18.53 ± 0.03	this thesis
PLK (B01)	18.46 ± 0.03	this thesis
FOBE	18.36 ± 0.12	Ripepi et al. (2004)
M_V(RR)	18.34 ± 0.10	this thesis

Table 5.2. True distance moduli for the Reticulum cluster. Column 2 gives the distance moduli obtained by using the same reddening and metallicity as in Dall'Ora et al. (2004b). The M_V(RR) value was obtained by adopting apparent magnitudes from Walker (1992) and the calibration $M_V(RR) = 0.20[Fe/H] + 0.98$ ***from Fernley et al. (1998). The photometric error has been estimated summing in quadrature the internal error with the calibration error.***

5.2 The distance to the LMC

The Large Magellanic Cloud can be considered as the cornerstone in the extragalactic distance scale, since it hosts several standard candles and secondary distance indicators that can be all considered at the same distance. Therefore, it is of extreme interest to compare distance moduli estimated with different indicators, to check the internal consistency of different distance scales. It is worth noting that distance estimates based on different indicators, such as Cepheid and RR Lyrae stars, give discrepant results. However, most recent values are converging and an average of 14 different distance indicators yields for the LMC a true distance modulus of 18.50 ± 0.04 (rms) mag (Alves 2004). Moreover, from the weighted mean of 10 different calibrations of the RR Lyrae stars distance scale, Cacciari & Clementini (2003) estimated a true distance to LMC of 18.48 ± 0.05, in close agreement with the Alves' estimate.

Values listed in table 5.2 seem to support the evidence that Reticulum is located between the Galaxy and the LMC, but this finding heavily depends on the adopted distance indicator. Therefore, we decided to estimate the distance between Reticulum and the LMC by using the same indicator. Recently, Borissova et al. (2004) measured metallicities and *K*-band magnitudes for 37 field RR Lyrae stars in the inner regions of the LMC. By adopting the theoretical relationships by B01 and B03, they found for LMC a distance of $(m-M)_0 = 18.48 \pm 0.08$. This value is to compare with the estimate of the Reticulum distance, based on the B01 theoretical relation, i.e. $(m-M)_0 = 18.46 \pm 0.03$. There is therefore the marginal evidence that Reticulum is closer than the LMC, i.e. $\Delta\mu = -0.02$. Unfortunately, the uncertainties in the measurements are too large to firmly establish whether Reticulum is within or beyond the LMC. To properly address this question, our group has already secured *K*-band photometry for five globular clusters belonging to LMC and for approximately 200 field RR Lyrae stars belonging to its main body. Data have been collected during two observing runs in December 2004 with SOFI and with ISPI, a 2k × 2k Rockwell Hawaii II infrared array available at the 4 meter telescope at Cerro Tololo Interamerican Observatory, and are being reduced.

V-band photometry of the RR Lyrae stars in Reticulum gives a de-reddened mean magnitude of $\langle V(RR) \rangle_0 = 18.98 \pm 0.01$ (Walker, 1992). Interestingly enough, from the analysis of 108 LMC field RR Lyrae stars, Clementini et al. (2003) obtained a de-reddened visual magnitude $\langle V(RR) \rangle_0 = 19.064 \pm 0.064$ at [Fe/H]=-1.5: if one compares this value with the mean value

obtained by Walker on the Reticulum RR Lyrae stars, this result seems to suggest that Reticulum is closer than LMC, with $\Delta\mu = -0.08$, that is approximately 2 kpc. It is worth noting that also in this case any conclusion is still hampered by the uncertainties on the measurements.

Finally, on the basis of a geometrical model for the LMC, it is possible to give the relative distances between the center of the LMC and Reticulum. In the last years, very different geometrical models for the LMC have been produced. Schommer et al. (1992), by comparing radial velocities measurements of several LMC clusters with several rotation curves, and choosing the solution that minimizes the differences between observed radial velocities and model rotation curves, found an inclination of the LMC of $i = 27°$ and a line of nodes of $\Theta = -9°$. By comparing these values with the observed angular distance ρ and position angle ϕ of Reticulum ($\rho = 11.4°, \phi = 329$ °; Schommer et al., 1992) with respect to the LMC center by means of the equation $D/D_0 = 1 + \rho \tan i \sin(\phi - \theta)$ (van der Marel & Cioni, 2001), that gives the distance of one point D with respect to a reference point D_0, one finds that LMC is closer with respect to Reticulum of 0.08 mag, that is $\Delta\mu = +0.08$.

On the basis of an analysis of spatial variations in the apparent magnitude of features in the near-IR color-magnitude diagrams extracted from the Deep Near-Infrared Southern Sky Survey (DENIS) and 2MASS, van der Marel and Cioni (2001) obtained a quite different model for the LMC, yielding $i = (34.7 \pm 6.2)°$ and $\Theta = (122.5 \pm 8.3)°$. With these values one finds that the distance modulus of Reticulum is approximately 0.14 mag smaller than the center the LMC, that is $\Delta\mu = -0.14$.

Data listed in table 5.3 disclose that more work is required to assess the question.

Method	$\Delta\mu$ (mag)	Reference
PLK	-0.03	Borissova et al. (2004)
V_0(RR)	-0.08	Clementini et al. (2003)
Radial velocities	+0.08	Schommer et al. (1992)
NIR photometry	-0.14	van der Marel & Cioni (2001)

Table 5.3. Estimated differences between the distance modulus of Reticulum and LMC with different indicators. Differences are in the sense Reticulum-LMC.

5.3 The distance to M68

The field covered by the observations allowed us to obtain data for 34 out of the 42 RR Lyrae stars known in M68. Table 5.4 lists the photometric properties of the observed RR Lyrae stars.

Light curves were well-sampled, and a cubic spline was chosen to fit individual phase points (figure 5.4). Intensity-averaged mean magnitudes were therefore computed from the fitted spline. Figure 5.5 shows the empirical *PLK* relation of RR Lyrae stars in M68.First Overtones (empty triangles) have been fundamentalized. Red straight line is the best fit to observed data, i.e.

$$\langle K \rangle = -2.36(\pm 0.11)\log P + 13.80(\pm 0.03)$$

with a rms error of $\sigma = 0.04$ mag. The slope α seems slightly steeper than the predicted slope by B01 ($\alpha = -2.071$) and by B03 ($\alpha = -2.101$), while it is in good agreement with the slope of the average relation given by Catelan, Pritzl, & Smith (2004), who found $\alpha = -2.353$. However, when RRab and RRc stars are considered separately, the obtained slopes are $\alpha = -2.19(\pm 0.23)$ for the RRab stars and $\alpha = -2.56(\pm 0.26)$ for the RRc stars, to compare with the B03 predictions, -2.101 and -2.265, respectively.

It is worth noticing that these values do not depend on deceptive errors on the calibration, since photometric calibration simply adds a constant term to the instrumental magnitudes. However, mean magnitudes were obtained by interpolating observed data with spline curves: this means that some light curves, especially with RRab stars, could not have been properly fitted. Better results will be achieved with the templates by Jones, Carney, & Fulbright (1996), as adopted in the case of Reticulum.

By using the value [Fe/H] = −2.1 (Walker 1994), the comparison between observed magnitudes and absolute magnitudes predicted with the B03 semi-empirical calibration yields a distance modulus of

$$DM_0 = 15.24 \pm 0.04$$

where the error is the dispersion around the mean value.

Id	Period (days)	Epoch (HJD)	<*K*> (mag)	σ_K (mag)	Type	Notes
V3	0.39078	2451895.3068	14.569	0.006	d	
V4	0.39602	2451895.3472	14.504	0.007	d	
V5	0.28211	2451895.4159	14.901	0.013		
V6	0.36859	2451895.5256	14.613	0.005	c	
V7	0.38803	2451895.3337	14.603	0.008	c	
V8	0.39044	2451895.5787	14.617	0.006	d	
V9	0.57904	2451895.4406	14.425	0.009	ab	Blazhko
V10	0.55142	2451895.3778	14.497	0.007	ab	
V11	0.36494	2451895.5329	14.709	0.009	c	
V12	0.61580	2451895.4905	14.378	0.005	ab	Blazhko?
V13	0.36176	2451895.3566	14.676	0.008	c	
V14	0.55680	2451895.4181	14.477	0.008	ab	Blazhko?
V15	0.37227	2451895.4429	14.600	0.009	c	
V16	0.38201	2451895.4862	14.594	0.007	c	
V17	0.66755	2451895.7124	14.384	0.005	ab	Blazhko
V18	0.36735	2451895.4298	14.676	0.011	c	
V19	0.39170	2451895.5028	14.562	0.011	d	
V20	0.38577	2451895.3124	14.632	0.009	c	
V21	0.40707	2451895.5950	14.475	0.006	d	
V22	0.56344	2451895.7492	14.502	0.006	ab	
V24	0.37647	2451895.3311	14.580	0.008	c	
V25	0.64149	2451895.6444	14.383	0.005	ab	
V30	0.73364	2451895.5313	14.180	0.005	ab	
V31	0.39965	2451895.5814	14.513	0.008	d?	
V33	0.39059	2451895.6582	14.536	0.007	c	
V35	0.70250	2451895.4674	14.295	0.005	ab	
V36	0.41099	*N/A*	14.515	0.006	d	
V37	0.38463	2451895.4196	14.567	0.008	c	
V38	0.38294	2451895.4663	14.588	0.006	d?	
V43	0.37071	2451895.4921	14.645	0.009	c	
V44	0.38514	2451895.4157	14.547	0.007	c	
V45	0.39087	2451895.3124	14.550	0.007	d?	
V46	0.73816	2451895.3086	14.209	0.004	ab	Blazhko?
V47	0.37295	2451895.4026	14.518	0.007	c	

Table 5.4 Photometric properties of the RR Lyrae stars in M68. Intensity-averaged mean K magnitudes are computed by fitting the observations with cubic splines. Periods are given by Walker (1994), except for V10, evaluated on the basis of the fit. For V36 the ALLFRAME mean magnitude was used. Intrinsic photometric errors calculated by ALLFRAME are listed. In column 4 fundamental and first-overtone RR Lyrae stars are labelled with ab and c, respectively, while candidate mixed-mode RR Lyrae stars are labelled with d.

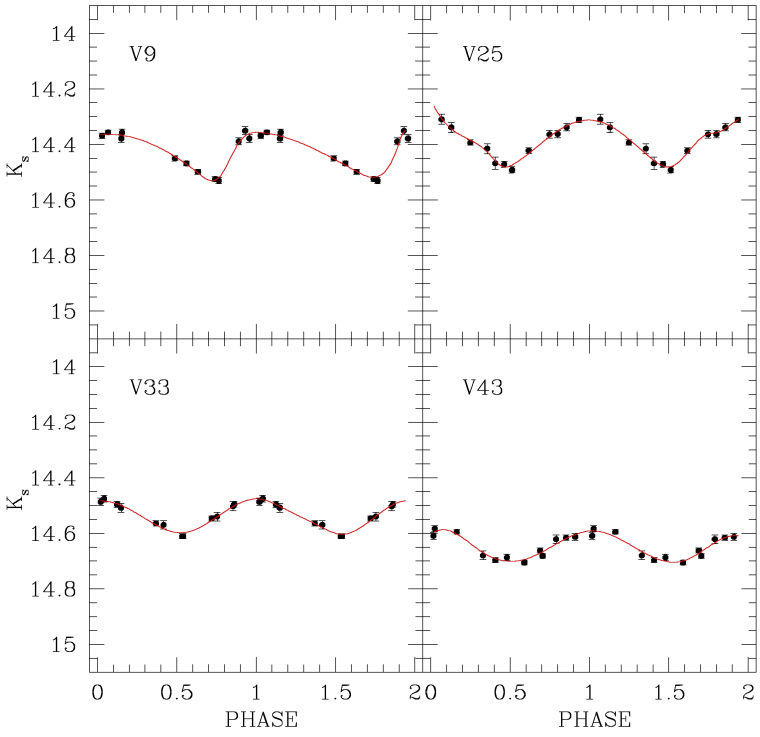

Figure 5.4 Light curves for some of the RR Lyrae stars in M68. Points depict observations, and the straight line is the interpolating spline. V9 and V25 are RRab stars, while V33 and V43 are RRc stars.

De-reddened magnitudes were obtained by considering an extinction of $E(B-V)=0.07$ (Walker 1994) and by using the relations $A_K = 0.11 A_V$ and $A_V = 3.1E(B-V)$ (Cardelli, Clayton, & Mathis 1989). Therefore, the *K*-band absorption is $A_K = 0.022$.

M68 hosts a sizable sample of RRc stars, and hence it is interesting to use the theoretical relations from B03 separately for fundamental and first-overtone pulsators, i.e. the relations

$$M_K^F = 0.511 - 2.102 \log P + 0.095 \log Z - 0.734 \log L - 1.753 \log M / M_r$$
$$M_K^{FO} = -0.029 - 2.265 \log P + 0.087 \log Z - 0.635 \log L - 1.633 \log M / M_r$$

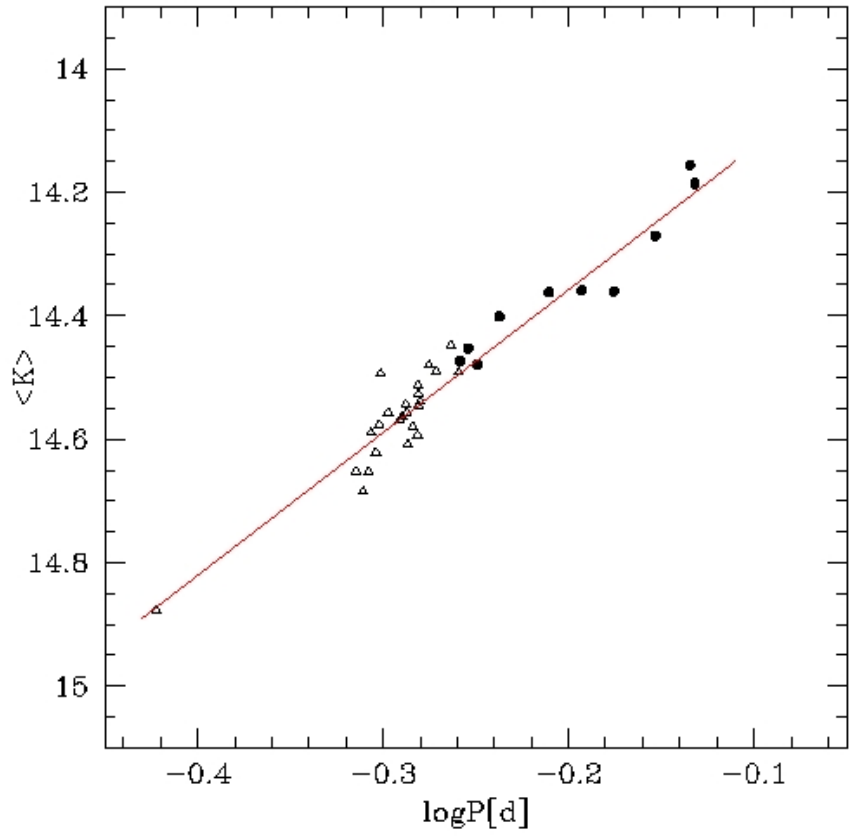

Figure 5.5 Intensity-weighted mean magnitudes <K> vs. logP. Filled circles are fundamental pulsators and open triangles are (fundamentalized) first-overtones. Double-mode pulsators have been considered as first-overtones. The straight line represents the empirical fit to the data.

By using typical values: $\log L = 1.71, M_r = 0.75 M_\odot$, and $M = 0.8 M_\odot$, the estimated distance moduli are $DM_0 = 15.12 \pm 0.03$ for fundamental pulsators and $DM_0 = 15.15 \pm 0.04$ for first-overtones. *V*-band mean magnitudes for the RR Lyrae stars in M68 are available from Walker (1994). Therefore, it is possible to use the (*V-K*) colors to derive a direct estimate for the luminosity of these stars, and to use the estimated luminosities in the previous equations. The obtained estimates are $DM_0 = 15.24 \pm 0.05$ and $DM_0 = 15.22 \pm 0.04$ for the RRab and for the RRc stars, respectively. It is interesting to note that the estimated luminosities are of the order of $\log L \approx 1.85$, suggesting that the RR Lyrae stars in M68 could be evolved objects. Finally, using the B01 theoretical relation the estimated distance is $DM_0 = 15.11 \pm 0.04$.

It is interesting to compare the obtained distance moduli with others available in the literature. RR Lyrae stars average magnitude obtained by Walker (1994) is $\langle V \rangle (RR) = 15.43 \pm 0.01$. By accounting for $A_V = 3.1E(B-V) = 0.22$ mag (Walker 1994), and using the $M_V - [Fe/H]$ calibration by Fernley et al. (1998), the de-reddened distance modulus to M68 is $DM_0 = 14.90 \pm 0.10$, where the uncertainty is due to the Fernley's calibration. Di Criscienzo, Marconi, & Caputo (2004) used the FOBE method to estimate the distance to M68. By adopting a mixing-length of $l/H_p = 1.5$ they obtain a distance modulus of $DM = 15.30 \pm 0.07$. Taking into account the absorption previously mentioned, the true distance modulus is $DM_0 = 15.08 \pm 0.07$.

As discussed in chapter 2, semi-empirical calibration gives distance moduli slightly larger than other methods (i.e. it gives slightly brighter absolute magnitudes), especially when compared to the Baade-Wesselink calibration, while the discrepancy is reduced with the FOBE method. Fully theoretical *PLK* distances seem instead to be in good agreement with the others estimate. However, theoretical *PLK* relations and FOBE relations are obtained from the same pulsation code. Therefore, a comparison between the results given by the two methods can only check the internal consistency of the theoretical scenario, and cannot reveal possible systematic effects. In the table 5.5 are summarized the results.

Method	$(m-M)_0$	**Reference**
PLK (B03) semi-empirical	15.24 ± 0.04	this thesis
PLK (B03) theoretical	15.23 ± 0.05	this thesis
PLK (B01)	15.11 ± 0.04	
FOBE	15.08 ± 0.07	Di Criscienzo et al. (2004)
M_V(RR)	14.90 ± 0.10	this thesis

Table 5.5. True distance moduli for M68. Column 2 shows the distance moduli obtained by using the same reddening and metallicity as in Walker (1994). In the PLK theoretical has been used the average of the estimates on the RRab and RRc star. The M_V(RR) value was obtained by adopting apparent magnitudes from Walker (1994) and the calibration $M_V(RR) = 0.20[Fe/H] + 0.98$ ***from Fernley et al. (1998). In this latter case, photometric error has been estimated summing in quadrature the internal error with the calibration error.***

5.4 The distance to NGC 3201

The field covered by observations allowed us to obtain data for 30 of the 77 RR Lyrae stars catalogued in NGC 3201. Table 5.6 lists the photometric properties of the RR Lyrae stars. For the *PLK* relation, mean magnitudes were computed by interpolating observed light curves with cubic splines (figure 5.6). Figure 5.7 shows the empirical *PLK* relation of RR Lyrae stars in NGC3201. First Overtones (empty triangles) have been fundamentalized, while red straight line is the best fit to observed data, i.e.

$$\langle K \rangle = -2.35(\pm 0.08)\log P + 12.25(\pm 0.02)$$

with a rms error of $\sigma = 0.02$ mag .

As in the case of M68, the slope α seems slightly steeper than the predicted slope by B01 (α =-2.071) and by B03 (α =-2.101). If only the RRab stars are considered, the slope is $\alpha = -2.13$ ($\pm$ 0.12), in excellent agreement with the B03 value.

The distance to NGC 3201 was estimated with the B03 semi-empirical calibration, having de-reddened the *K* magnitudes with the average value *E(B-V)*=0.30 (Piersimoni, Bono, & Ripepi 2002). The de-reddened distance modulus obtained is $DM_0 = 13.47 \pm 0.03$. Distance modulus was also estimated with the B03 theoretical calibration. Adopting $\log L = 1.61$, $M_r = 0.7 M_\odot$, $M = 0.7 M_\odot$, as indicated in B03 for the estimated metallicity, the de-reddened distance moduli are $DM_0 = 13.32 \pm 0.03$ and $DM_0 = 13.38 \pm 0.03$ for RRab and RRc stars (only three objects), respectively. As in the cases of Reticulum and M68, the availability of accurate *V*-band magnitudes (Piersimoni. Bono, & Ripepi 2002; Layden & Sarajedini 2003) allowed us to estimate the luminosity of the RR Lyrae stars from the (*V-K*) colors. The estimated luminosity level for the RR Lyrae stars is of the order of $\log L \approx 1.75 - 1.8$, and the true distance moduli are $DM_0 = 13.45 \pm 0.04$ and $DM_0 = 13.49 \pm 0.06$ for RRab and RRc stars, respectively, in excellent agreement with the semi-empirical calibration. If the theoretical relation by B01 is used, the obtained value is $DM_0 = 13.38 \pm 0.03$.

Id	Period (days)	Epoch (HJD)	<K> (mag)	σ_K (mag)	A_K (mag)	Type	Notes
V6	0.5250936	51854.8627	13.026	0.008	0.15	ab	
V7	0.6303322	51855.2694	12.942	0.007	0.06	ab	
V8	0.6286573	51855.0346	12.881	0.007	0.05	ab	
V9	0.5257087	51854.8384	13.166	0.009	0.12	ab	
V10*	0.5351644	51855.1172	13.091	0.008	0.10	ab	
V11	0.2990490	51854.9999	13.410	0.006	0.06	c	
V12	0.4955547	51855.2109	13.161	0.006	0.13	ab	
V13	0.5752145	51855.0613	13.059	0.006	0.10	ab	
V14*	0.5092945	51854.9905	13.103	0.007	0.12	ab	
V15*	0.5346644	51854.7849	12.954	0.008	0.12	c	
V16*	0.263438	51854.2894	13.528	0.008	0.07	c	
V22	0.6059882	51854.9437	12.925	0.009	0.09	ab	
V23*	0.586775	51854.8345	12.930	0.007	0.08	ab	
V29*	0.529120	51854.9792	13.136	0.007	0.07	ab	Blazhko?
V35	0.6155244	51854.9976	12.945	0.011	0.07	ab	
V36	0.482143	51944.9874	13.192	0.006	0.09	ab	Blazhko?
V37	0.5772897	51854.8765	13.100	0.009	0.02	ab	Blazhko?
V38	0.5091250	51855.1351	13.249	0.006	0.11	ab	
V40	0.6421096	51854.9268	12.921	0.006	0.05	ab	
V48	0.3412136	51854.9699	13.248	0.008	0.06	c	Blazhko?
V49	0.5815089	51854.8653	13.045	0.005	0.11	ab	
V50*	0.542178	51854.7882	13.074	0.005	0.13	ab	
V51	0.5206220	51854.8378	13.172	0.008	0.13	ab	Blazhko?
V71	0.6011859	51855.2198	12.963	0.007	0.07	ab	
V73	0.5199500	51854.7882	13.010	0.005	0.14	ab	
V76	0.526680	51855.0677	12.983	0.006	0.12	ab	Blazhko?
V77	0.5676648	51855.2073	13.026	0.006	0.13	ab	
V78	0.513900	51854.7849	13.080	0.008	0.09	ab	
V90	0.606105	51855.2579	12.884	0.006	0.10	ab	
V92	0.539585	51855.2172	13.015	0.009	0.12	ab	

Table 5.6 Photometric properties of the RR Lyrae stars in NGC3201. ALLFRAME mean* K *magnitudes and photometric intrinsic errors are used. Periods from Piersimoni et al (2002) were adopted, except for variables labelled with (*), from Layden & Sarajedini (2003). Individual reddenings from Piersimoni et al., except for V10, V14, V15, V16 and V29, adopted from Layden & Sarajedini. Fundamental and first-overtone RR Lyrae stars are labelled with ab and c, respectively.

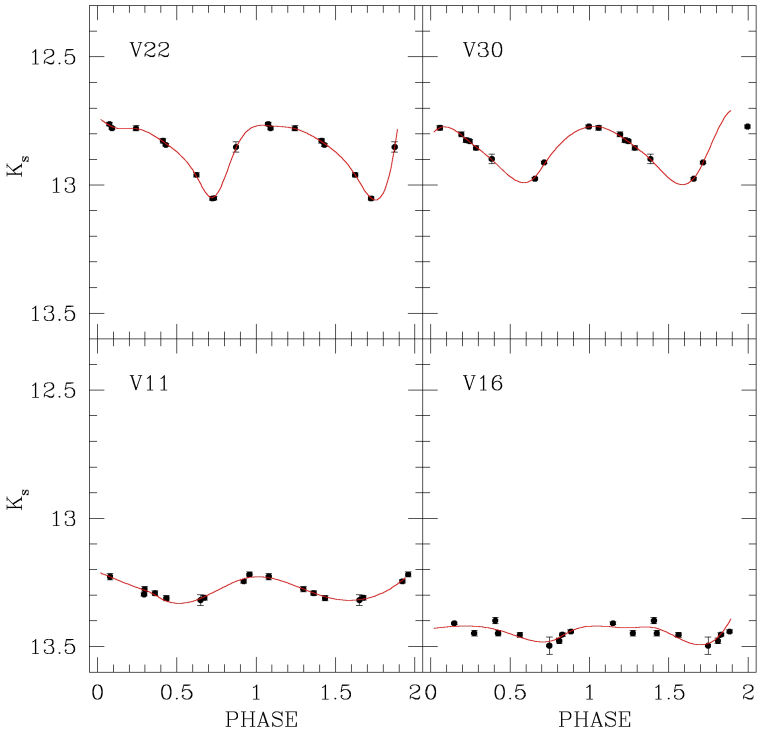

Figure 5.6 Light curves for some of the RR Lyrae stars in NGC 3201. Points depict observations, and the straight line is the interpolating spline. V22 and V30 are RRab stars, while V11 and V16 are RRc stars.

These results can be compared with the findings of Layden & Sarajedini (2003), who estimated a true distance modulus of $DM_0 = 13.40 \pm 0.05$ from RR Lyrae stars, and $DM_0 = 13.35 \pm 0.05$, by adopting the Period-Luminosity relation of Petersen & Hog (1998) on the δ Scuti stars; and with the results of Covino & Ortolani (1997), who estimated $DM_0 = 13.35 \pm 0.05$ and $DM_0 = 13.5 \pm 0.2$ from the *V*-band luminosity of RR Lyrae stars and the Main Sequence fitting, respectively.

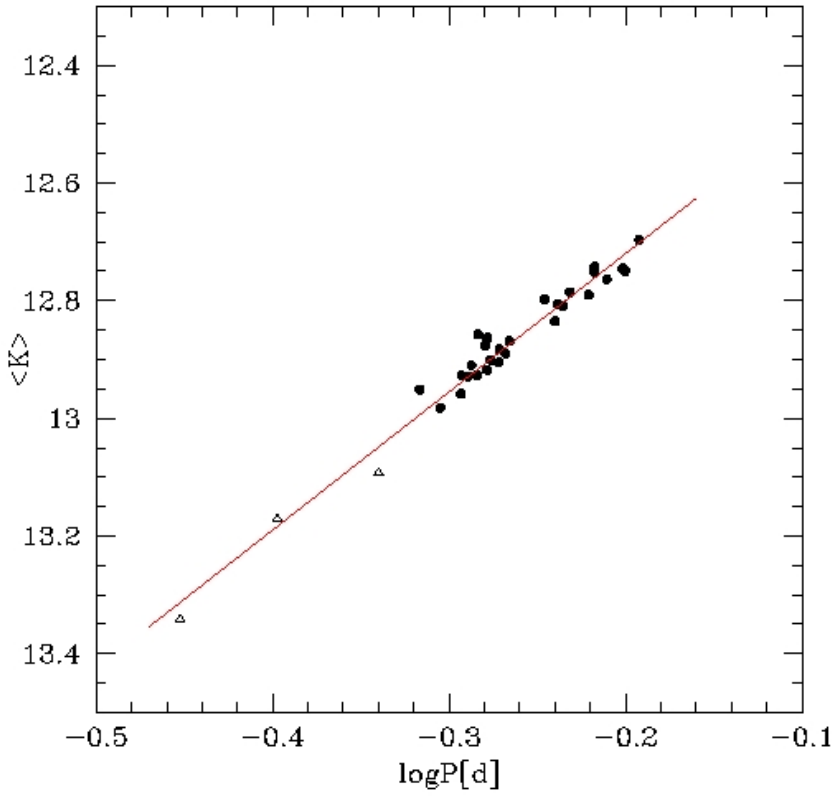

Figure 5.5. Intensity-weighted mean magnitudes <K> vs. logP. Filled circles are fundamental pulsators and open triangles are (fundamentalized) first-overtones. Red straight line marks the observed slope.

Method	$(m-M)_0$	Reference
PLK (B03) semi-empirical	13.47 ± 0.03	this thesis
PLK (B03) theoretical	13.47 ± 0.06	this thesis
PLK (B01)	13.38 ± 0.03	this thesis
M_V(RR)	13.40 ± 0.05	Layden & Sarajedini (2003)
δ Scuti stars	13.35 ± 0.05	Layden & Sarajedini (2003)
M_V(RR)	13.3 ± 0.15	Covino & Ortolani (1997)
Main Sequence fitting	13.5 ± 0.2	Covino & Ortolani (1997)

Table 5.7. True distance moduli for NGC 3201.The PLK theoretical value is the simple mean of the RRab and RRc results.

5.5 The RGB *Bump*

The RGB luminosity function is a very robust observable in order to check the accuracy of the inner structure of RGB evolutionary models. In particular, the RGB luminosity function can supply tight constraints on the chemical stratification inside these stars (Renzini & Fusi Pecci 1988).

The hydrogen jump in the H encountered by the thin H-burning shell affects the evolutionary rate, and in turn, the star counts along the RGB. In particular, the RGB bump marks the evolutionary phase during which the H-burning shell crosses the chemical discontinuity left over by the convective envelope soon after the first dredge up. Dating back to its first detection in 47 Tuc (Lee 1977), the RGB bump has been the crossroad of several theoretical and observational investigations (Ferraro et al. 1999; Zoccali et al. 1999, and references therein).

Owing to the anti-correlation of the RGB bump luminosity with the stellar metallicity, the detection of this feature is much easier in metal-intermediate and in metal-rich GGCs. This is the reason why the RGB bump has only been detected in a few metal poor GGCs. By roughly estimating the RGB bump from the CMD, we detected the RGB bump at $K_{bump} = 12.7 \pm 0.1$ for M68 and $K_{bump} = 11.5 \pm 0.1$ for NGC3201.

To further constraint the plausibility of these detections, we performed a detailed comparison with updated evolutionary predictions (see fig. 5.6) provided by Pietrinferni et al. (2004). In order to estimate the absolute K magnitude of the RGB bump in M68 and in NGC3201, we adopted the true distance moduli based on the B03 *PLK* relations, i.e. $DM_0 = 15.24$ for M68 and $DM_0 = 13.47$ for NGC3201. Here we adopted the fully theoretical calibrations of the *PLK*, since the distances obtained with these relations agree quite well with those obtained with other independent methods. To perform an exhaustive comparison between theory and observations, we also included the RGB bump estimates by Ferraro et al. (2000) and by Valenti et al. (2004).

Data plotted in figure 5.6 indicate that a fairly good agreement does exist between updated theoretical models (solid lines) and observations. However, more interesting conclusions concerning the quadratic behavior suggested by Valenti et al. (2004) can be reached as soon as the luminosity function analysis will be complete.

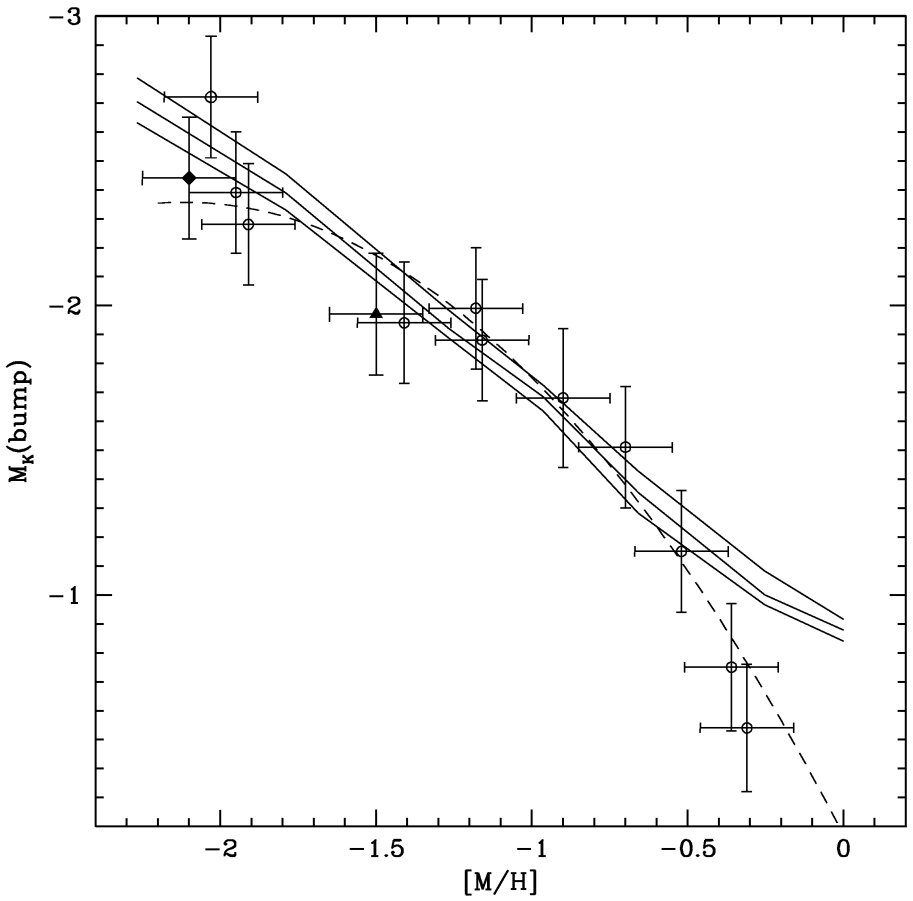

Figure 5.6. Comparison between predicted absolute* K *magnitude of the RGB bump as a function of the global metallicity and observational measurements. The filled diamond marks the location of the RGB bump of M68, while the filled triangle marks the location of the bump of NGC3201. The different solid lines display predictions for different assumptions on the cluster age: 12 Gyr (top line), 14 Gyr (middle line), and 16 Gyr (bottom line). The dashed line is the fit to the empirical measurements provided by Valenti et al. (2004).

Conclusions

The main aim of this thesis project is to explore the RR Lyrae distance scale through the K-band Period-Luminosity relation (*PLK*). The best way to accomplish this goal is to get *K*-band photometry for RR Lyrae stars in globular clusters, since for each cluster they are a homogeneous sample of objects, sharing the same chemical composition, the same evolutionary properties and the same distance.

In this thesis we have produced, for the first time, deep *J, Ks* photometry of the Galactic Globular Clusters M68 and NGC 3201, and of the Large Magellanic Cloud cluster Reticulum. The observed slopes of the *PLK* relations are in good agreement with the slopes predicted by theoretical models (Bono et al. 2001; Bono et al. 2003). This evidence encouraged us to use the theoretical relations to estimate the distance of the selected clusters.

Comparisons between predicted (B03) and observed slopes of the *PLK* relation for RRab and RRc stars are shown in Figure 1 and Figure 2, respectively.

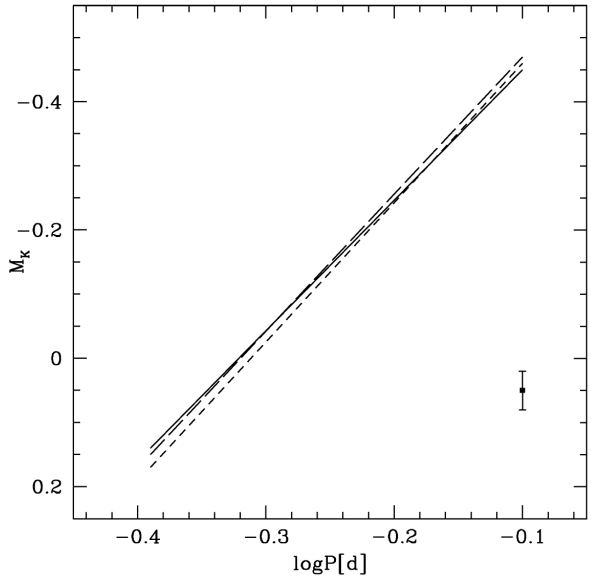

Figure 1. Comparison between predicted and observed slopes of the PLK relation for RRab stars. Solid line depicts the theoretical relation from B03, while long-dashed lines shows the observed relations for Reticulum and M68. Short dashed line represents the observed relation for NGC3201. On the right corner is shown the typical dispersion in the observed relations.

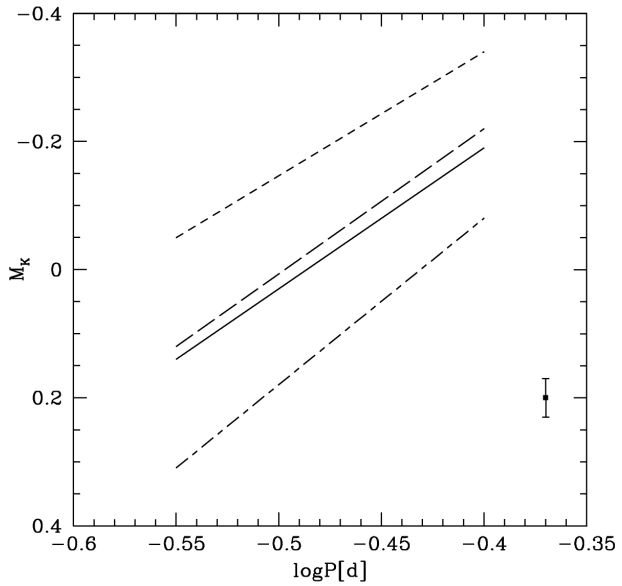

Figure 2. Comparison between predicted and observed slopes of the PLK relation for RRc stars. Solid line depicts the theoretical relation from B03, while long-dashed lines shows the observed relations for Reticulum, long-short dashed line is the relation for M68, and short dashed line represents the observed relation for NGC3201. On the right corner is shown the typical dispersion in the observed relations.

The agreement is excellent for RRab stars, and current findings do not support the large scatter in the slopes found by Longmore et al. (1990), who found slopes in the range between -1.8 and -2.5.

Relations for RRc stars are dominated by the large uncertainties in the slope estimates (ranging from $\alpha = -1.9$ to $\alpha = -2.6$).

It is interesting to note that, if RRc stars are fundamentalized, slopes found for M68 and NGC 3201 match very well the average slopes predicted by Catelan, Pritzl, & Smith (2004), who found an average slope of $\alpha = -2.353$, and the slopes predicted by Cassisi et al. (2004), which range from $\alpha = -2.30$ to $\alpha = -2.41$, depending on the cluster metallicity and on the HB morphology.

Table 1 summarizes the results on the distance estimates and shows a comparison between optical and *PLK*-based distance moduli. Column 3 lists the weighted mean of different *V*-band based RR Lyrae distance estimates (M_V*-[Fe/H], FOBE*), while columns 4 and 5 show the distances estimated with the B03 semi-empirical (SE) calibration and the B01 theoretical relation. For each *PLK* distance estimate, it is shown the difference with the *V*-band based estimate. Data listed in the table show that B03 *PLK* distances are greater than optical ones.

It is difficult to draw firm conclusions from only three points, but the general trend seems to suggest that the difference is larger with decreasing metallicity.

B01 calibration seems to agree, within the errors, with optical estimates. It is interesting to note that the differences between the SE and the B01 estimates can be accounted for with the difference in the metallicity term.

Object	[Fe/H]	μ_0 (V)	μ_0 (B03) SE	μ_0 (B01)	$\Delta\mu_0$ SE	$\Delta\mu_0$ B01
M 68	-2.1	15.02±0.06	15.24±0.04	15.11±0.04	+0.22	+0.09
Reticulum	-1.71	18.35±0.10	18.52±0.03	18.46±0.03	+0.17	0.11
NGC 3201	-1.53	13.40±0.05	13.47±0.03	13.38±0.03	+0.07	-0.02

Table 1. Comparison between PLK and optical-based RR Lyrae distances. The third column lists the (weighted) mean of the most recent distance estimates for the selected clusters. Columns, 4 and 5 show the distance moduli estimated with the B03 semi-empirical calibration (SE) and the B01 theoretical relation, respectively. Columns 6 and 7 list the difference in the distances between* PLK *and* V*-band based estimates.

In order to perform an independent check of our results, we estimated the distance moduli of the selected targets by using the *PLK* relations computed by Cassisi et al. (2004). By adopting an approach very similar to Catelan, Pritzl, & Smith (2004), they put the *PLK* relation in the form

$$M_K = M_K^{-0.3} + b_K(\log P_F + 0.3)$$

(where $M_K^{-0.3}$ is the M_K value when $\log P_F = -0.3$), and they computed $M_K^{-0.3}$ and b_K for various metallicities and HB morphologies. The intrinsic uncertainties on the coefficients are of the order of 0.02 mag.

By adopting the HB morphologies from Harris (1996; M68 and NGC 3201), and from Walker (1992; Reticulum), we estimated the following distances

Object	μ_0 (mag)
M 68	15.15 ± 0.04
Reticulum	18.47 ± 0.03
NGC 3201	13.38 ± 0.02

where the listed uncertainties are the dispersion around the mean values. These estimates are in excellent agreement with the B01 calibration (column 5 of table 1), and hence seem to support this calibration.

It is worth noting that the *PLK* relations estimated by Cassisi et al. (2004) and by Catelan, Pritzl, & Smith (2004) require the knowledge of both the metallicity and of the evolving mass of the RR Lyrae stars. The knowledge of this latter parameter for cluster RR Lyrae stars can be inferred from the HB morphological type, while it is completely unknown for field RR Lyrae stars. On the other hand, pulsationally based *PLK* relations only need the knowledge of the metallicity and, once calibrated, can be adopted for individual RR Lyrae stars.

It is therefore of paramount importance to reach a solid empirical calibration of the *PLK* relation. Note that we have already collected accurate near-infrared data for a large sample of globular clusters (17) that cover a wide range of metal contents and HB morphologies. Firmer conclusions will therefore be drawn about the calibration of the *PLK* relation when the photometry of this dataset will be complete.

Bibliography

Alves, D.R. 2000, ApJ, 539, 732

Alves, D.R. 2004, NewAR, 48, 659

Alves, D.R., Cook, K.H., & Wishnow, E. 2003, AAS, 203, 5216

Asplund M., Grevesse N., and Sauval J. 2004, invited review presented at Cosmic abundances as records of stellar evolution and nucleosynthesis, ASP *in press*, astro-ph/0410214

Bailey, S.I., & Pickering, E.C. 1902, AnHar, 38, 1

Baker, N., & Kippenhahn, R. 1962, ZA, 54, 114

Bessell, M.S., & Brett, J.M., 1988, PASP, 100, 1134

Benedict, G.F., et al. 2002, AJ, 123, 473

Blazhko, S. 1907, Astron. Nachr., 175, 325

Bono, G. 2003, in Stellar Candles for the Extragalactic Distance Scale, ed. D. Alloin and W. Gieren (Berlin: Springer Verlag), 85

Bono, G., Caputo, F., Castellani, V., & Marconi, M. 1997, A&AS, 121, 327

Bono, G., Caputo, F., Castellani, V., Marconi, M., & Storm, J. 2001, MNRAS, 326, 1183 (B01)

Bono, G., Caputo, F., Castellani, V., Marconi, M., & Storm, J. 2002, MNRAS, 332, L78

Bono, G., Caputo, F., Castellani, V., Marconi, M., Storm, J., & Degl'Innocenti, S. 2003, MNRAS, 344, 1097 (B03)

Bono, G., Castellani, V., & Marconi, M. 2000, ApJL, 532, L129

Bono, G., Stellingwerf, R. F. 1994, ApJS, 93, 233

Borissova, J., Minniti, D., Rejkuba, M., Alves, D., Cook, K. H., & Freeman, K. C. 2004, A&A, 423, 97

Buckley, D. R. V., Longmore, A. J., & Dixon, R. I. 1992, MmSAI, 63, 433

Butler, D. J. 2003, A&A, 405, 981

Buonanno, R., Corsi, C. E., Buzzoni, A., Cacciari, C., Ferraro, F. R., & Fusi Pecci, F. 1994, A&A, 290, 69

Cacciari, C., & Clementini, G., 2003, in Stellar Candles for the Extragalactic Distance Scale, ed. D. Alloin and W. Gieren (Berlin: Springer Verlag), 105

Caputo, F. 1997, MNRAS, 284, 994

Caputo, F., Castellani, V., Marconi, M., & Ripepi, V. 1999, MNRAS, 306, 815

Caputo, F., Castellani, V., Marconi, M., & Ripepi, V. 2000, MNRAS, 316, 819

Cardelli, J. A., Clayton, G. C., & Mathis, J. S. 1989, ApJ, 345, 245

Carpenter, J. M., 2001, AJ, 121, 2851

Carretta, E., & Gratton, R. G. 1997, A&AS, 121, 95

Cassisi, S., Castellani, M., Caputo, F., & Castellani, V. 2004, A&A, 426, 641

Cassisi, S., Castellani, V., degl'Innocenti, S., & Weiss, A. 1998, A&AS, 129, 267

Cassisi, S., Castellani, V., degl'Innocenti, S., Salaris, M., & Weiss, A. 1999, A&AS, 134, 103

Castellani, V. 2005, Astrofisica Stellare, *in preparation*

Castellani, M., Caputo, F., & Castellani, V. 2003, A&A, 410, 871

Castellani, V., Chieffi, A., & Pulone, L. 1991, ApJS, 76, 911

Catelan, M., Pritzl, B. J., & Smith, H. A. 2004, ApJS, 154, 633

Clement, C. M., et al. 2001, AJ, 122, 2587

Clementini, G., Gratton, R., Bragaglia, A., Carretta, E., Di Fabrizio, L., & Maio, M. 2003, AJ, 125, 1309

Corwin, T. M., & Carney, B. W. 2001, AJ, 122, 3183

Covey, K. R., Wallerstein, G., Gonzalez, G., Vanture, A. D., & Suntzeff, N. B. 2003, PASP, 115, 819

Covino, S., & Ortolani, S. 1997, A&A, 318, 40

Cox, J. P. 1955, ApJ, 122, 286

Cox, J. P. 1963, ApJ, 138, 487

Da Costa, G. S., & Armandroff, T. E. 1995, AJ, 109, 2533

Dall'Ora, M., et al. 2003, AJ, 126, 197

Dall'Ora, M., et al. 2004, MMSai, 75, 138 (2004a)

Dall'Ora, M., et al. 2004, ApJ, 610, 269 (2004b)

Demers, S., & Kunkel, W. E. 1976, ApJ, 208, 932

Demers, S., & Wehlau, A. 1977, AJ, 82, 620

Di Criscienzo, M., Marconi, M., & Caputo, F. 2004, ApJ, 612, 1092

Dirsch, B., Richtler, T., Gieren, W. P., & Hilker, M. 2000, A&A, 360, 133

Eddington, A. S. 1926, The Internal Constitution of the Stars, Cambridge: Cambridge University Press

Fernley, J. 1994, A&A, 284, L16

Fernley, J., Skillen, I., Carney, B. W., Cacciari, C., & Janes, K. 1998, MNRAS, 293, L61

Ferraro, F. R., Montegriffo, P., Origlia, L., & Fusi Pecci, F. 2000, AJ, 119, 1282

Ferraro, F. R., Paltrinieri, B., Rood, R. T., & Dorman, B. 1999, ApJ, 522, 983

Gonzalez, G., & Wallerstein, G. 1998, AJ, 116, 765

Gratton, R. G., Bragaglia, A., Clementini, G., Carretta, E., Di Fabrizio, L., Maio, M., & Taribello, E. 2004, A&A, 421, 937

Gratton, R., Carretta, E., Bragaglia, A., Clementini, G., & Grundahl, F. 2003, in ASP Conf. Ser. 296, New Horizons in Globular Cluster Astronomy, ed. G. Piotto, G. Meylan, S. G. Djorgovski and M. Riello (San Francisco: ASP), 381

Gratton, R. G., & Ortolani, S. 1987, A&AS, 71, 131

Gratton, R. G., Tornambè, A., & Ortolani, S. 1986, A&A, 169, 111

Harris, W. E. 1996, AJ, 112, 1487

Helmi, A., & White, S. D. M. 1999, MNRAS, 307, 495

Helmi, A., & White, S. D. M. 2001, MNRAS, 323, 529

Jones, R. V., Carney, B. W., & Fulbright, J. P. 1996, PASP, 108, 877

Jones, R. V., Carney, B. W., Storm, J., & Latham, D. W. 1992, ApJ, 386, 646

Joyce, R. R. 1992, in ASP Conf. Ser. 23, Astronomical CCD observing and reduction techniques, ed. S. B. Howell (San Francisco: ASP), 258

King, D. S., & Cox, J. P. 1968, PASP, 80, 365

Kinman, T. D. 1959, MNRAS, 119, 538

Kraft, R. P., & Ivans, I. I. 2003, PASP, 115, 143

Landolt, A. U. 1992, AJ, 104, 340

Layden, A. 2002, ASP, 259, 118

Layden, A. C., & Sarajedini, A. 2003, AJ, 125, 208

Lee, J., Carney, B. W., & Habgood, M. J. 2005, AJ, 129, 251

Lee, S. W. 1977, A&AS, 27, 381

Lee, Y., & Demarque, P. 1990, ApJS, 73, 709

Liu, T., & Janes, K. A. 1990, ApJ, 354, 273

Lidman, C., Cuby, J. G., Vanzi, L., Billeres, M., Hainaut, O., & Pompei, E. 2003, SOFI User's manual, http://www.ls.eso.org/lasilla/sciops/ntt/sofi/archive/manual/sofiman.pdf

Longmore, A. J., Dixon, R., Skillen, I., Jameson, R. F., & Fernley, J. A. 1990, MNRAS, 247, 684

Longmore, A. J., Fernley, J. A., & Jameson, R. F. 1986, MNRAS, 220, 279

Mackey, A. D., & Gilmore, G.F. 2004, MNRAS, 352, 153

Marconi, M., Caputo, F., Di Criscienzo, M., & Castellani, M. 2003, ApJ, 596, 299

Mateo, M. L. 1998, ARA&A, 36, 435

Monelli, M., et al. 2003, AJ, 126, 218

Nemec, J. M. 1985, AJ, 90, 204

Olech, A., Kaluzny, J., Thompson, I. B., & Schwarzenberg-Czerny, A. 2003, MNRAS, 345, 86

Oosterhoff, P.T. 1939, Obs, 62, 104

Persson, S. E., Murphy, D. C., Krzeminski, W., Roth, M., & Rieke, M. J. 1998, AJ, 116, 2475

Petersen, J. O., & Hog, E. 1998, A&A, 331, 989

Peterson, C. J., & Kunkel, W. E. 1977, PASP, 89, 634

Pickering, E. C., & Bailey, S. I. 1895, ApJ, 2, 321

Piersimoni, A. M., Bono, G., & Ripepi, V. 2002, AJ, 124, 1528

Pietrinferni, A., Cassisi, S., Salaris, M., & Castelli, F. 2004, ApJ, 612, 168

Preston, G. W. 1959, ApJ, 130, 507

Renzini, A., & Fusi Pecci, F. 1988, ARA&A, 26, 199

Rey, S., Lee, Y., Joo, J., Walker, A. R., & Baird, S. 2000, AJ, 119, 1824

Rey, S., Yoon, S., Lee, Y., Chaboyer, B., & Sarajedini, A. 2001, AJ, 122, 3219

Rich, R. M., Da Costa, G. S., & Mould, J. R. 1984, ApJ, 286, 517

Ripepi, V., et al. 2004, CoAst, 145, 24

Rousselot, P., Lidman, C., Cuby, J. G., Moreels, G., & Monnet, G. 2000, A&A, 354, 1134

Reid, M. J. 1993, ARA&A, 31, 345

Ritter, A. 1879, Ann. Phys. Chem. Neue Folge, 8, 157

Romaniello, M., Primas, F., Mottini, M., Groenewegen, M., Bono, G., & Francois, P. 2005, A&A, 429, L37

Rose, W.K. 1973 Astrophysics, New York: Holt, Rinehart and Winston

Rutledge, G. A., Hesser, J. E., & Stetson, P. B. 1997, PASP, 109, 907

Salaris, M., Chieffi, A., & Straniero, O. 1993, ApJ, 414, 580

Sandage, A. 1990, ApJ, 350, 631

Schommer, R. A., Suntzeff, N. B., Olszewski, E. W., & Harris, H. C. 1992, ApJ, 103, 447

Schwarzschild, M. 1940, HarCi, 437, 1

Sersic, J. L. 1974, Ap&SS, 28, 365

Silbermann, N. A., & Smith, H. A. 1995, AJ, 110, 704

Smith, H. A. 1995, RR Lyrae Stars, New York, NY: Cambridge University Press, 65

Soszynski, I., et al. 2003, AcA, 53, 93

Stetson, P. B. 1987, PASP, 99, 191

Stetson, P. B. 1990, PASP, 102, 932

Stetson, P. B. 1992, ASP, 25, 297

Stetson, P. B. 1993, IAU Colloq. 136: Stellar Photometry - Current Techniques and Future Developments (Cambridge: Cambridge University Press), 291

Stetson, P. B. 1994, PASP, 106, 250

Stetson, P. B. 2000, PASP, 112, 925

Storm, J. 2004, A&A, 415, 987

Suntzeff, N. B., Schommer, R. A., Olszewski, E. W., & Walker, A. R. 1992, AJ, 104, 1743

Sersic, J. L. 1974, Ap&SS, 28, 365

Tammann, G. A., Sandage, A., & Reindl, B. 2003, A&A, 404, 423

Trager, S. C., Djorgovski, S., & King, I.R. 1993, in ASP Conf. Ser. 50, Structure and Dynamics of Globular Clusters, ed. S. G. Djorgovski and G. Meylan (San Francisco: ASP), 347

Valenti, E., Ferraro, F. R., Perina, S., & Origlia, L. 2004, A&A, 419, 139

van Albada, T. S., & Baker, N. 1973, ApJ, 185, 477

van den Bergh, S. 1993, ASP, 50, 1

van der Marel, R. P., & Cioni, M. L. 2001, AJ, 122, 1807

Vivas, A. K., et al. 2001, ApJL, 554, L33

Walker, A. R. 1992, AJ, 103, 1166

Walker, A. R. 1993, AJ, 105, 527

Walker, A. R. 1994, AJ, 108, 555

Zhevakin, S. A. 1953, Russ. Astron. J., 30, 161

Zhevakin, S. A. 1959, SvA, 3, 389

Zinn, R. 1993, in ASP Conf. Ser. 48, The globular clusters-galaxy connection, ed. G. H. Smith, and J. P. Brodie (San Francisco: ASP) 38

Zinn, R., & West, M. J. 1984, ApJS, 55, 45

Zoccali, M., Cassisi, S., Piotto, G., Bono, G., & Salaris, M. 1999, ApJL, 518, L49

Acknowledgements

The period devoted to the attainment of the PhD is a very important stage in the professional maturation.

In Rome I've had the invaluable opportunity to work in a very dynamical (and smart!) community, and I also had the unique chance to gain a satisfactory international experience, attending meetings, observing in some of the most magic places in the world, and having the possibility to learn from several of the most skilled researchers. Many thanks to my "collaborators", Alistair, Horace, Jesper, and Peter.

I am hopelessly indebted with Giuseppe Bono, Roberto Buonanno and Filippina Caputo for having offered me this opportunity.

I should also thank so many people that I could write another PhD thesis to finish....so, everybody, thank you!

In the coming years, I will remember this period with a picture, portraying Carlo, Giuseppe, me and Matteo (Cicci..), taken by Horace Smith. The Horace's comment was:

"*A though gang of astrophysicists, planning misfits in the streets of Monte Porzio*".

And this is ***exactly*** what we did!

Finally, this thesis is dedicated to the sacrifices of who loves me.